UNIVERSITÀ
DEGLI STUDI
DI PADOVA

Head Office: Università degli studi di Padova

Department of Surgery, Oncology and Gastroenterology

PhD course in Clinical and Experimental Oncology and Immunology

Series XXXV

Combinatory therapeutic approaches for haematological and solid tumors with Cytokine-Induced Killer (CIK) cells

Coordinator: Prof. Stefano Indraccolo

Supervisor: Prof. Antonio Rosato

Co-supervisor: Roberta Sommaggio, PhD

PhD student: Annavera Ventura

Abstract

In the last decade adoptive cell therapy (ACT) achieved extraordinary results in antitumor treatments, especially against haematological malignancies, even if with some limitations - such as - safety, high costs of manufacturing, and restricted cell sources. In this regard, Cytokine-Induced Killer cells are achieving considerable clinical relevance, due to the low risk of acute graft versus host disease (GvHD) in both autologous and allogeneic settings, their feasibility, and the limited costs of production. CIK cells are a heterogeneous population of T lymphocytes, expanded and activated *ex vivo* from peripheral blood mononuclear cells (PBMCs) or cord blood, with the addition of recombinant human interferon-γ (rhIFN- γ), anti-CD3 monoclonal antibody (mAb), and recombinant human interleukin-2 (rhIL-2). During the expansion, CIK cells acquire the expression of CD56 and present several functional and phenotypical properties of both T and Natural Killer (NK) cells. Importantly, CIK cells do not require any genetic engineering or antigen-specific stimuli to recognize tumor cells and exert a potent major histocompatibility complex (MHC)-unrestricted antitumor activity. In 2016, our group showed that CIK cells increase their ability to kill tumor cells by antibody-dependent cellular cytotoxicity (ADCC) due to the expression of the Fragment chain (Fc)-γ Receptor IIIa (CD16a).

In this study, we assessed CIK cell cytotoxicity against $CD20^+$ lymphoma patient-derived samples, both *in vitro* and *in vivo*, by the combination with two clinical grade anti-CD20 monoclonal antibodies (mAbs), Rituximab (RTX) or Obinutuzumab (Gazyva/Gazyvaro, OBI). Furthermore, to fulfil the huge amount of cell numbers required to achieve successful clinical responses, we optimized an efficient serum-free protocol for optimal expansion of CIK cells in gas-permeable rapid expansion (G-Rex®) devices from both healthy donors and B-cell malignant patients. G-Rex® devices allow the expansion of a high number of CIK cells, fully functional in terms of viability, phenotype, and lytic activity. Moreover, the addition of the bispecific T cell-engager (BiTE) Blinatumomab (CD3xCD19) to the cultures from B-cell lymphoma patients eliminated the residual tumor cells ($CD19^+$), favouring the expansion of CIK cells, even if starting from blood samples containing very low percentages of $CD3^+$ precursor cells.

Next, we extended this efficient combinatorial strategy to solid cancers, focusing on Human epidermal growth factor receptor 2 (Her-2) - expressing breast cancers. We combined CIK cells with both the mAb Trastuzumab (TRS) or with the bispecific single chain Fragment variable (bsscFv) Her2xCD3 in a BiTE-like format. The synergistic effect exerted by CIK cells with the antibodies,

especially with the Her2xCD3, resulted in a remarkable *in vitro* lytic activity against several Her-2^{+} cancer cell lines, even at very low effector/target ratio and a reduced dosage of the bsscFv, encouraging clinical perspectives of this approach for the ACT.

To further gain insight into the trafficking and the infiltration of transferred CIK cells in solid tumors, we explored an agarose-embedded thick-tumor tissue slice assay combined with a high-resolution spinning disk confocal microscopy. This technique not only allows the tracking of labelled effector cells in the tumor tissue slice, but it can be useful also to explore the multicellular interactions taking place in the tumor microenvironment. Moreover, to study and characterize the tumor three-dimensional structure in terms of the stiffness of the extracellular matrix (ECM), we exploited the Second Harmonic Generation (SHG) microscopy which provides important information about collagen density and fibres organization.

Index

1. Introduction

1.1 Adoptive cell therapy (ACT)

According to the World Health Organization (WHO), cancer is a leading cause of death worldwide, accounting for nearly 10 million deaths in 2020 [1,2]. Depending on the cancer type and time of diagnosis, available treatments usually include surgery, radiotherapy, and/or systemic therapy (chemotherapy, hormonal treatments, targeted biological therapies). Over the last 20 years, new attempts to develop more efficient approaches to treat cancer have been investigated, such as cancer immunotherapy, which has become a clinically validated treatment for many cancers. Different from chemotherapy or radiotherapy, immunotherapy aims to boost and restore the activity of the immune system to eliminate malignant cells overriding their resistance mechanisms, including local immune evasion, tolerance, and systemic disruption of T cell signaling[3]. Cancer immunotherapy can be either active or passive. On one hand, the active approach aims at eliciting a specific host immune response by employing cancer vaccines, immunomodulators, oncolytic viruses, or cytokines[4].On the other hand, the passive approach involves the administration of therapeutic agents, such as monoclonal antibodies (mAbs), bispecific molecules, and cellular therapies[5]. In adoptive cell therapy (ACT), tumor-reactive immune cells are stimulated and expanded *ex vivo*, and subsequently infused back into the patient, after a lymphoid-depleting preparative regimen. Such immune effector cells can derive from the patient itself (autologous setting) or another healthy donor (allogeneic setting)[6]. The pilot experiment of ACT came from the Rosenberg team in the 1980s, by re-infusion of *in vitro* expanded tumor-infiltrating lymphocytes (TILs) derived from a metastatic melanoma patient with interleukin (IL)-2[7]. However, the administration of IL-2 and the toxic effects observed in treated patients following the lymphodepletion regimen limited the use of TILs for adoptive immunotherapy. In the following years, ACT emerged with Lymphokine-Activated Killer (LAK) cells, which represent the first *ex vivo*-generated Natural Killer (NK) cell-enriched products for adoptive immunotherapy[8]. Over the past decades, many effector cells have been developed, including NK cells[9], γδ T cells[10], NK -T [11] cells, Cytokine-Induced-Killer[12] (CIK) cells, or T-cell receptor (TCR)[13] or chimeric-antigen receptor (CAR)-engineered T cells[14]. ACT with autologous NK cells co-administrated with IL-2 started soon after the development of LAK cells but showed limited therapeutic effects [15,16]. Moreover, due to the low availability of NK cells in peripheral blood (~10%), NK cells were obtained from alternative sources, such as cord blood [17–19], clonal NK-92 cell line [20], and stem cell-derived NK cells [21–23]. Clinical trials with allogeneic NK cells showed enhanced persistence and proliferation but still limited therapeutic effects [24–26]. The γδ T cells are a particular subtype of T cells expressing a TCR composed of γ and δ chains, with structural and functional heterogeneity. γδ cells express the

typical NK cell receptor Natural-Killer group 2 member D (NKG2D), and display cytotoxic activity against stressed and abnormal cells, such as viral infected and tumor cells[27]. Immunotherapy with γδ T cells demonstrated safety and feasibility in many solid cancer types, such as renal, head and neck, mammary, hepatocellular and pancreatic cancer, and neuroblastoma [28]. However, median response rates are still limited [29–31]and the expansion of cells to achieve clinically relevant numbers remains a huge issue[32]. NK-T cells are specialized T cells that recognize glycolipid antigens presented by CD1d molecule[33]. Following stimulation, NK-T cells lead to downstream activation of both innate and adaptive immune cells in the tumor microenvironment (TME), a feature that has impelled the development of NK-T cell-based immunotherapies for treating cancer. Recent preclinical data from numerous studies on a variety of murine tumor models have shown the significant role of NK-T cells in protecting tumor growth and metastasis [34].

The advent of genetic engineering opened the possibility to modify immune cells to redirect them in an antigen-specific manner and boost their antitumor efficacy. In this regard, antigen-specific TCR-modified T cells are employed against several tumor types, such as metastatic renal and melanoma cancer [35], epithelial cancers [36,37], breast cancer, and endometrial cancer [38]. However, several challenges limit their efficacy, such as neurologic toxicity due to cross-reactivity with antigen isoforms expressed on healthy neurons [35], traffic to tumor sites, and antigen escape. In the last decade, among ACT strategies, CAR-T cell therapy gained great attention for the remarkably effective and durable clinical responses achieved in the hematological setting[39]. CARs are modular synthetic receptors guiding lymphocytes, such as NK or T cells, in an antigen-specific manner, in order to precisely recognize and eliminate cancer cells [40]. In particular, CD19-CAR-T cell therapy revealed an excellent success, with astonishing complete remission rates in patients with relapsed/refractory aggressive B-cell lymphomas [41–43]. Although encouraging CAR-T cell therapy progress achieved in the hematologic setting, the maximal anti-tumoral success of CAR-T cells for solid tumors is long overdue because of the shortage of solid tumor-specific antigens[44] and the impact of the TME. Indeed, the tumor niche represents the first physical barrier limiting the trafficking and the infiltration of CAR-T cells in solid cancers, but the anti-tumor potential of adoptively transferred cells is mainly hampered by hypoxia, specific TME metabolism, and immunosuppressive cells[45]. Hence, despite the clinical success of CAR-engineered cell therapy, several general hurdles such as the development of severe toxicities [46,47], very high production costs, technically complex manipulation processes, huge cell numbers required to achieve clinical response, and regulatory or financial issues[39], limit CAR-T therapy wide application [46,47]. However, many of those hurdles might be overcome whether the effector population can be easily generated in clinically relevant numbers and redirected against the

tumor cells without genetic modifications. Most recently, an increasing number of clinical trials on both hematological and solid tumors support the efficacy and the easy manufacturing of CIK cells (http://www.clinicaltrials.gov).

1.2 Cytokine-Induced Killer (CIK) cells

CIK cells were first discovered in 1991 [48] as LAK cell successors [49]. CIK cells are a heterogeneous population of activated $CD3^+CD8^+$ lymphocytes that during the *ex vivo* expansion acquire NK phenotypic markers, such as the CD56, NKG2D, and CD16a cell-surface receptors [50,51]. By the isolation from PBMCs or cord blood [51–53], CIK cells are easily obtained *in vitro* by sequential exposure to rhIFN- γ, anti-CD3 mAb, and timed addition of rhIL-2. IFN-γ priming is important to stimulate monocytes to produce the contact-dependent factor CD58/lymphocyte function-associated antigen (LFA)-3 and the soluble factor IL-12, which are critical for CIK cell expansion *in vitro* [54,55]. On the other hand, the anti-CD3 antibody interacts with the CD3ε chain of TCR and provides a mitogenic signal subsequently sustained by IL-2, which is crucial for CIK cell proliferation and expansion *in vitro* [56,57]. Although CIK cells have been studied since the 1990s in both pre-clinical studies and clinical trials, there is not yet a standardized protocol to produce them. CIK could be stimulated with different concentrations of anti-CD3 monoclonal antibody and IL-2, ranging from 50 to 100 ng/mL and from 300 to 500 IU/mL, respectively [51,58,59]. Moreover, several groups have expanded CIK cells together with dendritic cells (DCs)[60,61], or by adding in the culture different cytokines, such as IL-1, IL-6, IL-7, IL-12, and IL-15 [59,62–64]. Terminally expanded $CD3^+CD56^+$ CIK cells are large granular lymphocytes (LGL)[52] that originate from $CD3^+CD8^+$ precursor cells representing the predominant subgroup (20±70%) of the bulk population, for the remainder consisting of $CD3^+CD56^-$ precursor cells, and a small amount of $CD3^-CD56^+$ NK cells[52]. Like T lymphocytes, CIK cells express TCR in a polyclonal fashion with a similar proportion of α and β chains compared to ɤ and δ chains of peripheral blood T cells[52], arguing that CIK cells are more related to T cells than NK cells. Nonetheless, CIK cells share additional phenotypical features with NK cells, as they express NKG2D and relatively low levels of other natural killer activating receptors, such as NKp30 and NKp44[65]. The anti-tumor activity of CIK cells is primarily mediated by the NKG2D receptor that plays a pivotal role in CIK cell-tumor recognition. Indeed, CIK cells do not require antigen-specific stimuli or any genetic engineering to recognize tumor cells [49] and exert a TCR - and major histocompatibility complex (MHC) - unrestricted lytic activity against both solid and hematologic malignancies, but not healthy tissues[58,66]. Several experiments using blocking antibodies against CD3, CD8, CD56, TCR α/β, and MHC class I and II molecules failed to inhibit CIK cytotoxic activity[65,67].

Otherwise, functional assays blocking the NKG2D receptor, using small interfering RNA, or redirected cytolysis showed that CIK cell killing activity is mostly mediated by the NKG2D, rather than by the TCR-engagement[68,69]. NKG2D expression by CIK cells is upregulated by IFN- γ, IL-2, and the TCR cross-link with the mAb OKT-3. NKG2D receptor binds to its stress-inducible ligands, the MHC-class I-like molecules, MICA and MICB, and members of the UL-16 protein binding family (ULBP1-4) expressed by malignant cells. While the NKG2D mediates the interactions between CIK and tumor cells, the final cytotoxic mechanism is triggered by the release of granzyme B and perforin [50,66,70,71]. Moreover, significant inhibition was obtained by blocking LFA-1 and intracellular cell adhesion molecule (ICAM)-1 demonstrating that CIK cell cytolytic activity requires cell-to-cell contact with tumor target cells [65,67]. Furthermore, recent data published from our group have shown that CIK cells can mediate a potent ADCC due to the CD16a expression if combined with clinical-grade monoclonal antibodies (mAbs) [51,72]. Moreover, evidence highlight that *in vivo* CIK cells present a low risk of acute GVHD [73,74], and do not rely on exogenous rhIL-2 to survive, limiting the risk of multi-organ toxicity[49,75]. Indeed, the abundant IFN- γ production occurring in expanded CIK cells results in a protective effect against GVHD [76,77], as demonstrated by the fact that CIK cells generated from IFN- γ knock-out mice induced lethal GVHD when infused across MHC barriers [73,77]. Overall, clinical trials confirmed the safety and the very low toxicity of CIK cell infusions in patients with a broad spectrum of cancer types, in both the autologous [78–82] and the allogeneic [83–86] setting. The advantages of CIK cells in terms of feasibility, safety, and easy manufacturing introduce them as a pharmacological tool for cancer immunotherapy over other cellular therapies. In the last decade, several combinatory strategies are being investigated to improve CIK cell anti-tumor efficacy, including the combination of CIK cells with oncolytic virus[87] (OV), DCs [88,89], clinical-grade antibodies[72], chemotherapeutic drugs[90], and checkpoint inhibitors[91], as well as the engineering of CIK cells to express a tumor-specific CAR[92] (Fig.1).

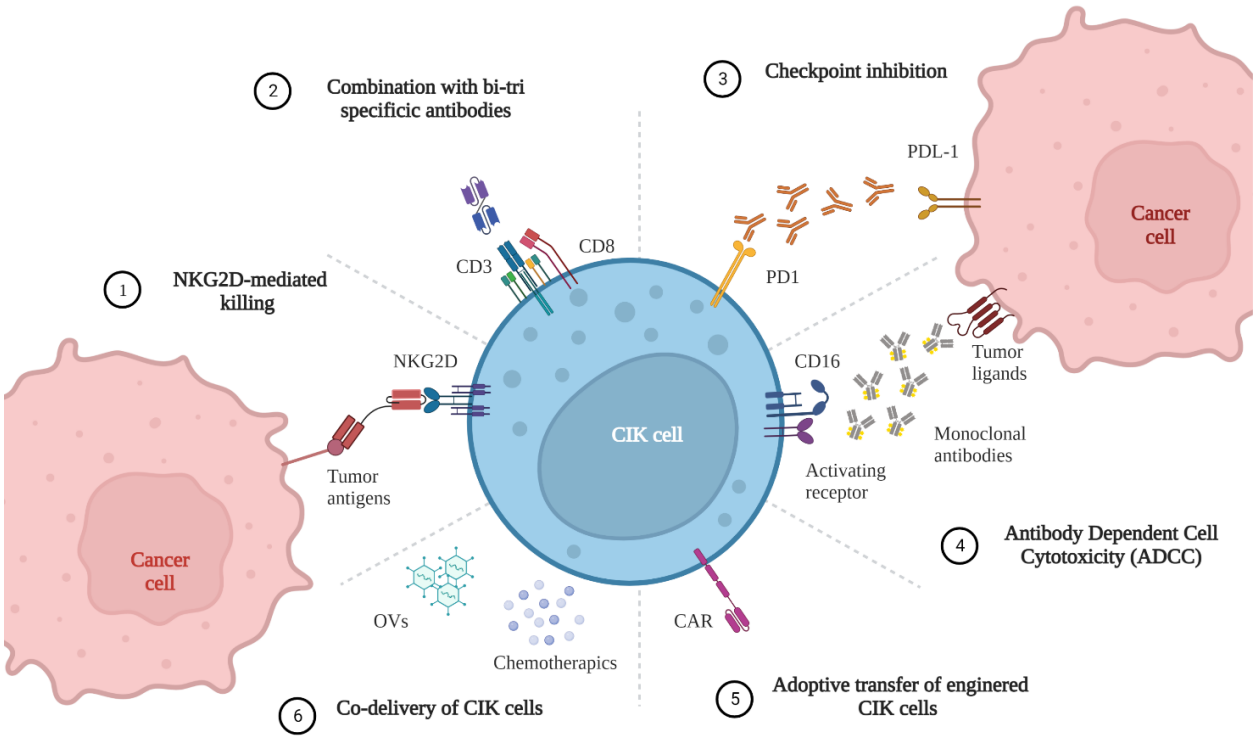

Figure 1. CIK cells as a versatile "pharmacological tool" for cancer immunotherapy. Created with Biorender.com

Although CIK cells are widely used in several clinical trials for both solid and liquid tumors, they are not well known worldwide in terms of treatment efficiency or phenotypic and functional characterization. In this regard, we seek to clarify some of the issues related to the definition of CIK cells in the literature, highlighting differences existing between CIK cells, as properly defined, circulating CIK cells[93] and NK-T cells[94].

1.2.1 Circulating $CD3^+CD56^+$ cells

In 2009, Franceschetti and colleagues reported that the presence of circulating $CD3^+CD56^+$ cells account for a mean of 4,7 % (1±11%) of mononuclear cells and they are defined as immune-experienced T cells because they are present only in adult peripheral blood, but not in cord blood [52]. Circulating $CD3^+CD56^+$ cells are mainly $CD3^+CD8^+$ cells, but they present functional and phenotypic differences from their *ex vivo* expanded CIK cells. Circulating $CD3^+CD56^+$ cells express CD56 with less intensity - mean fluorescent intensity (MFI) 135 - compared to *in vitro*-generated CIK cells - MFI 710 – and, they present an oligoclonal TCR with a skewed ɤδ repertoire[52]. Moreover, they express only 8% of NKG2D mediated-killing receptor compared to 80±90% expressed by *in vitro*-expanded CIK cells. Additionally, circulating $CD3^+CD56^+$ cells do not exert cytotoxic activity against

the NK cells -target, such as the K562 lymphoma cell line[52]. Evidence suggests that experienced circulating $CD3^{+}CD56^{+}$ cells may arise *in vivo* following the activation of T cells by antigenic stimuli.

1.2.2 Natural Killer (NK)-T cells

NK-T cells are a subpopulation of T cells, defined by the expression of NK markers, and well renowned for being potent cytokine producers. Even though NK-T cells express the CD3 and CD56 molecules similar to CIK cells, NK-T are different from CIK cells in terms of origins, cluster of differentiation, TCR fashion, mechanism of cell-recognition and, cytokines production. Here we report some crucial differences existing between NK-T and CIK cells, because the distinction is often misleading.

Nowadays NK-T cells are classified into 1) "Classical NK-T cells Type I and II", based on the CD1d-dependent activation and on the α/β TCR, and 2) "NK-T-like CD1d-independent cells" [94,95]. NK-T CD1d-restricted cells are lipid antigen–reactive T lymphocytes originating in the thymus that act as crucial regulators of the innate and adaptive immune response, in humans and mice, playing an important role in infection, including from bacteria, viruses, parasites, and fungal pathogens[96]. Conversely, different works have demonstrated that the properly defined CIK cells are derived *ex vivo* after cytokine stimulation from CD3 precursor T cells[93]. The invariant TCR of NK-T cells Type I is composed of the Vα24-JαQ α-chain, and one of several β-chains, but mainly Vβ11. This TCR does not recognize peptide antigens like the α/β TCR of classical cytotoxic T lymphocyte (CTL), but the glycolipid antigens presented by CD1 molecule on APCs[94,97]. Instead, Type II do not express the invariant Vα24 TCR, but they can be activated by other lipids presented by CD1d on APCs[94]. The term NK-T cell was first used in 1995 to define a subset of mouse T lymphocytes expressing the NK cell marker NK1.1[94], the equivalent human NK marker CD56. Indeed, while classical NK-T cells express constitutively the NK1.1 marker, CIK cells acquire the expression of CD56 during their *in vitro* expansion. Importantly, Classical NK-T Type I/II and NK-T-like CD1d-independent cells are $CD4^{+}$, double negative CD4/CD8 or $CD8^{+}$[94], whereas CIK cells are mainly CD8-expressing lymphocytes[66,93]. Classical NK-T cells exibit a single invariant TCR α chain paired with a restricted number of Vβ chains and recognize glycolipid antigens presented by the non-classical MHC molecule CD1, contrary to CIK cells that present a heterogeneous Vβ-TCR repertoire and they are not able to recognize CD1- presented antigens[98]. Other important differences existing between classical NK-T and CIK cells are that, different from CIK cells, upon stimulation classical NK-T cells produce a large amount IL-4 and they have no higher antitumor cytotoxicity than CIK cells[94].

1.3 "Bench to bedside": Gas-permeable static culture devices for CIK cells clinical translation

The therapeutic dose of CIK cells used in clinical trials ranges between 10^8 to 10^{10} cells/infusion, both against solid and haematological malignancies [84–86,79,99,100]. The expansion of such a high number of cells could represent a crucial issue in ACT whether T-flasks are used, especially because frequent and time-consuming culture manipulations increase the chances of contamination. To overcome these issues gas-permeable culture bags [80,82,85,101], or bioreactors [102] have been recently employed for the large-scale production of CIK cells. However, CIK cell production for clinical immunotherapy often employs culture supplements that increase the expansion of cells, such as AB serum, frozen plasma, or platelet lysate[59]. Such supplements raise the risk of infection, increasing the variability of the expanded final product since the composition of serum and plasma is highly batch-dependent. Hence, the expansion of a massive cell number remains complex and expensive, even though the employment of such innovative protocols and culture systems.

In this regard, G-Rex® culture devices are emerging as a valid alternative for the *ex vivo* expansion of many cell types, such as CIK cells[103], Cytotoxic T Lymphocytes [104], TILs [105,106], T_{reg} cells [107], and NK cells [108]. G-Rex devices are designed to allow an increased depth of the medium above cells, which delivers virtually unlimited oxygen and nutrients, and diluted waste. A silicone permeable membrane placed in the bottom of the device optimizes the cell proliferation rate by the O_2 and CO_2 gas exchange. Indeed, this system allows cell expansion without any media exchange leading to a reduced risk of contamination. G-Rex device ensures effector cell survival and cytotoxic activity against tumor targets[104,107–109], thereby encouraging the cell therapy-based approach in cancer treatment.

In this study, we investigated the advantages of using the G-Rex system to expand clinically relevant numbers of CIK cells under serum-free conditions.

1.4 Hematological malignancies

Hematological malignancies are the types of cancer affecting blood, bone marrow, and lymph nodes[110]. The 2016 updated WHO system indicates morphology as the central distinguishing feature for the classification of hematopoietic and lymphoid tissue malignancies. Although, also mutation screening is increasingly being utilized for confirmation of morphologic diagnosis and, at times, for directing the diagnostic process[110]. Haematological cancers are referred to as leukaemia, lymphoma, and myeloma depending on the cell type affected. Specifically, myeloid malignancies derive from bone marrow progenitor cells that normally develop into erythrocytes, granulocytes (neutrophils, basophils, and eosinophils), monocytes, or megakaryocytes. On the other hand, lymphoid neoplasms

originate from T or B cell progenitors, mature T (cytotoxic T cells, helper T cells, or T regulatory cells), or mature B (B cells or plasma cells) lymphocytes. Lymphoid neoplasms, defined as leukaemia, show bone marrow and blood involvement and are distinguished from those that are present as a mass, otherwise called lymphoma. Since the FDA approbation of the chimeric mAb anti-CD20 Rituximab (RTX) in 1997[111,112], lymphocytic leukaemia and lymphoma patients frequently experienced relapse and increased resistance to radiotherapy [113–115] or chemotherapy [116] treatments. CD20 is a non-glycosylated surface phosphoprotein that is found on most healthy and malignant B cells[117]. It undergoes little post-translational structural modifications, thereby maintaining predictable binding epitopes. No natural CD20-ligands are known, thus reducing endogenous binding competitors for mAbs. Therefore, the CD20 expression in virtually all mature B cell lymphoid malignancies and its distinct absence from pre-B hematopoietic stem cells and terminally differentiated plasma cells, limits the mAbs off-target toxicity, retaining the stem cell pool, which is important for B cell regeneration following therapy[118]. The first mAb anti-CD20 RTX was constituted by the murine 2B8 a variable heavy (VH) and variable light (VL) chain region combined with the human kappa and IgG1 constant region directed against the B-cell-specific antigen CD20 expressed on non-Hodgkin's lymphomas (NHL). The therapeutic efficacy of RTX was due to the non-proliferative effect exerted on CD20-expressing lymphoma cells and to the recruitment of immune cells playing strong complement-dependent cytotoxicity (CDC) against CD20-expressing cells[112]. However, several forms of resistant tumors, such as RTX-refractory or advanced-stage lymphoma patients, have limited the therapeutic potential of RTX-based treatments. To overcome such hurdles, the anti-CD20 mAb OBI was developed. OBI is a glycoengineered antibody endowed with an enhanced binding affinity to the FcγRIII receptor on immune effector cells, which results in a superior or more rapid ADCC *in vitro* [119–121] and patients [122–125], compared to RTX. Clinical trials with OBI showed a promising response in R/R patients, both in monotherapy [126–128] and in combination with chemotherapy [124,129,130].

In this thesis work, we explored the potential anti-tumor effect of CIK cells in combination with OBI against CD20-expressing lymphoma.

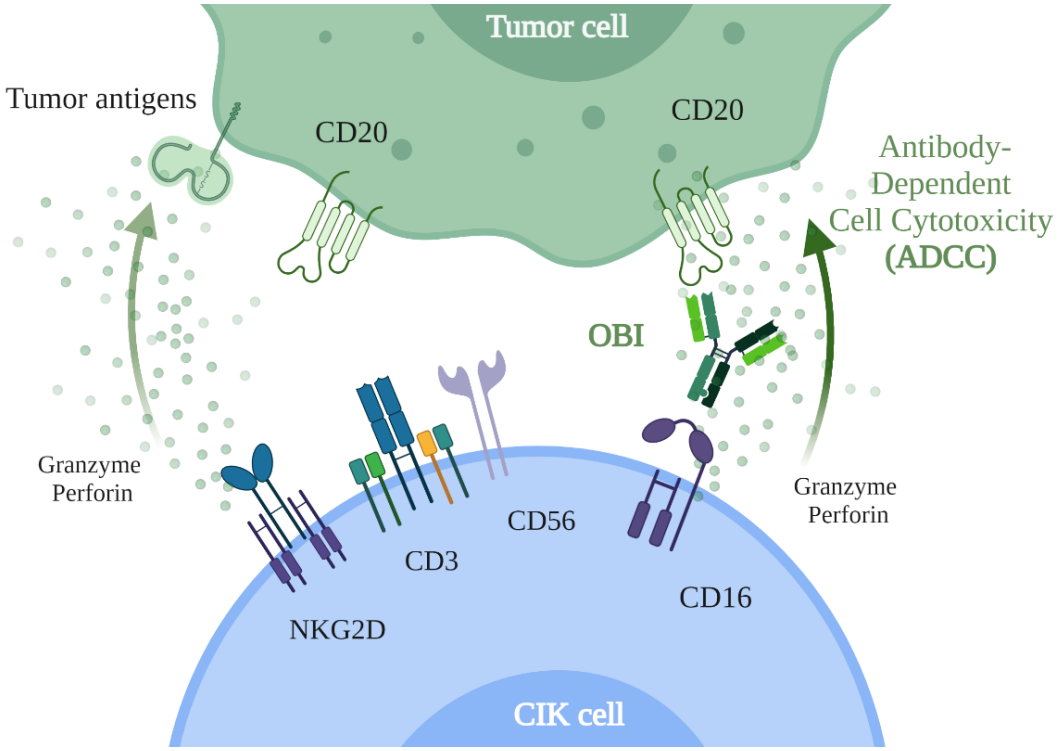

Figure 2. ADCC mediating CIK cells killing activity against CD20-expressing lymphoma. Created with Biorender.com

1.5 Her-2/neu^{+} breast cancer

Breast cancer (BC) is the second leading cause of cancer death worldwide and it still represents the most frequently occurring women cancer [131]. Even though several treatment options are improving the outcome of BC patients, metastatic disease progression and cancer relapse remain hard to overcome. However, drug resistance in various molecular BC subtypes [132] represents the main existing barriers to disease control. To date, among all the well-identified BC molecular targets, the most notable are the members of the epidermal growth factor receptor (EGFR). EGFR, also called ErbB-1 or Her-1, is the prototype of the type I subfamily, which includes three additional members: Her-2, Her-3, and Her-4. Whereas the Her-1 receptor binds to multiple distinct ligands that share the EGFR-like motif, Her-3, and Her-4 ligands are isoforms of the neuregulin (neu) differentiation factor, while no known ligands for the Her-2/neu receptor have been identified [133]. However, Her-2/neu can dimerize with various members of the family (EGFR, Her -3, or Her -4). Depending on the wide variety of ligands and dimerization partners, the specific tyrosine residues on the intracellular portion of the Her-2 /neu receptor are phosphorylated, activating the signalling pathways. Her-2 heterodimers are more stable[133], and their signalling is more potent [134] than other receptor combinations excluding Her-2[135]. The Her-2/neu gene is overexpressed or amplified in almost 15% of BC patients and it is

considered a poor prognosis marker. The Her-2 -enriched BC subtype is characterized by the high expression of Her-2-related genes and proteins [132], and it is associated with high tumor grade, DNA aneuploidy, high cell proliferation rate, negative assays for nuclear protein receptors for estrogen (ER) and progesterone (PR), p53 mutation, and topoisomerase IIα amplification[135–138].

With the advent of immunotherapy for BC in 1998, patient overall survival was significantly improved thanks to the FDA- approved humanized mAb anti-Her-2 Trastuzumab (TRS), or other Her-2 targeting antibodies[139]. However, not all patients benefit from TRS, or most of them unavoidably experience disease progression due to tumor resistance intrinsic mechanisms[140]. Recently, second-generation adjuvant trials testing single and dual Her-2-targeted agents, such as antibody-drug conjugates[141] (ADCs) or bsAbs, administered concomitantly or sequentially with chemotherapy, are emerging[142]. The bsAbs consist of two different single-chain Fragment variable (scFv) molecules, each containing a VH and VL chain region from a different parent Ig and can crosslink different target antigens, either on the same cell or on two different cells. Bispecific T-cell engagers (BiTEs) are engineered bsAbs expressing, within a single entity, the binding sites to the invariant TCR CD3ε chain and the binding site to a tumor-associated or a tumor-specific antigen [143–148]. This approach results in more efficient recruitment of T cells to target cancer cells, thus achieving a stronger lytic effect compared to IgG1 conventional mAbs engaging Fcγ RIII-expressing cells[148]. Blinatumomab was the first FDA-approved CD19xCD3 BiTE antibody construct for the treatment of Philadelphia chromosome-negative acute B-lymphoblastic leukemia[149].

In this thesis work, we explored the efficacy of a combinatory therapy for Her-2-expressing BC with CIK cells and the mAb TRS and the bAb Her2xCD3 in a BiTE-like format[150] (Fig. 3).

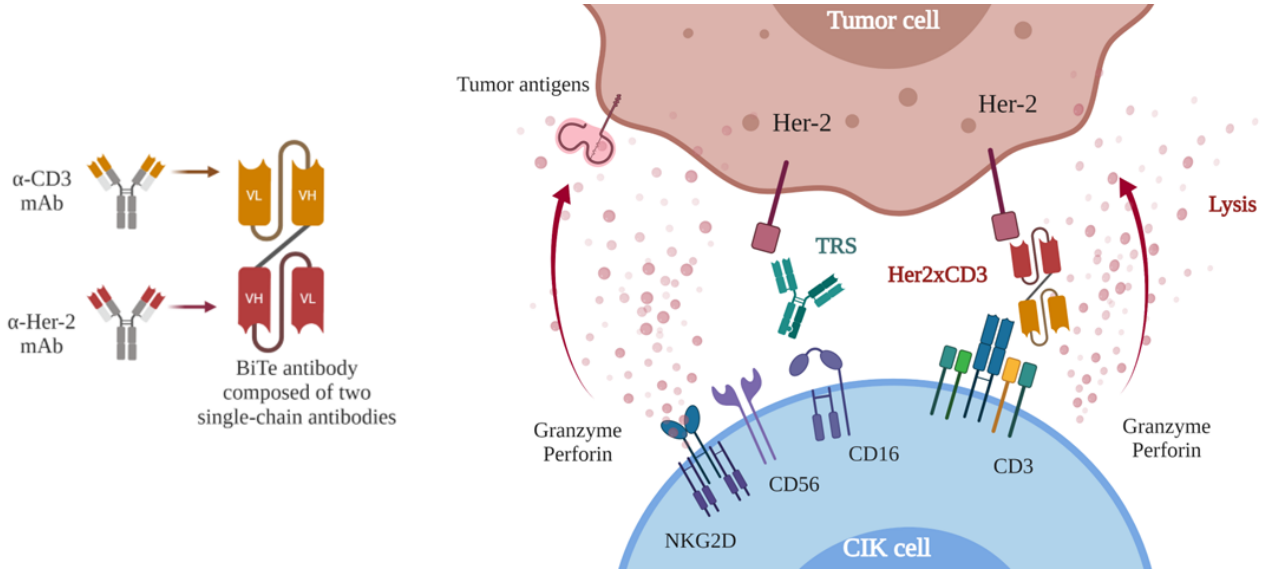

Figure 3. Her2xCD3 bsscFv antibody in a BiTE-like format (on the left) and the proposed combinatory therapy against Her-2^{+} breast cancer with CIK cells and TRS or Her2xCD3 (on the right). Created with Biorender.com

1.6 Breast cancer tumor micro-environment

Nowadays, the high heterogeneity of the tumor niche represents one of the major challenges in the field of ACT for solid malignancies. Cancer cells can functionally sculpt their microenvironment through the secretion of various cytokines, chemokines, and other factors. This results in the reprogramming of the surrounding cell, which subsequently enables them to play a putative role in tumor survival and progression. TME is mainly composed of immune cells, cytokines, metabolites, tumor-associated extracellular vesicles, immune inhibitory checkpoints, homeostatic alterations (i.e. hypoxia, angiogenesis, and cellular metabolic reprogramming), and tumor-associated stroma, as referred to ECM [151,152]. In this regard, it is also noteworthy to mention the impact of non-cellular components in determining tumor fate. More than an intercellular cement, ECM acts an active physiological role in cell communication, adhesion, and proliferation, and it may have both a supportive and an inhibitory impact on the adaptive immune response[153]. Indeed, ECM provides both signallings supporting T cell invasion, and signallings to inhibit T cell proliferation[154]. Equally, lymphatic vessels support tumor growth through angiogenesis, and serve as migratory highways for immune cells[155], while lymphatic endothelial cells trigger and regulate DC activation[156]. Furthermore, in the tumor niche, a crucial role in tumor proliferation, invasion, and metastasis is played by stromal cells, including cancer-associated fibroblasts (CAFs). CAFs not only are involved in the M2

macrophage polarization by secreting immunosuppressive cytokines, but they also contribute to $CD8^+$ T-cell exhaustion and deletion, as well [157].

In BC, the immunoediting process taking place in the tumor niche is orchestrated by both immunosuppressive and immunostimulating cells. Indeed, the presence of immunostimulating immune cells such as some macrophages, lymphocytes, NK cells, innate lymphoid cells (ILCs), DCs, and eosinophils is crucial for tumor control, but the anti-tumor response generated by such cells is inhibited and reverted by the action of immunosuppressive cells, such as myeloid-derived suppressor cells (MDSCs), mast cells (MCs), regulatory T cells (Tregs), and type 2- polarized tumor-associated macrophages (M2-like TAMs), which intrinsically collaborate remodelling a hostile TME [158](Fig.4). Especially regarding Her-2-expressing tumors, the composition of the TME plays a crucial role in determining the sensitivity to Her-2-targeted therapies [158]. For example, the presence of collateral immunosuppressive cells in the TME may significantly impact NK cell-triggered ADCC in the TRS-mediated anti-tumor activity[159]. Nonetheless, in BC the tumor ECM is characterized by increased stromal protein levels, stiffness, and changes in the overall organization relative to the healthy breast. These changes generate a dense physical barrier and an increased interstitial pressure (Fig.4), resulting in aberrant signalling and directly impacting drug delivery and therapy efficacy[154,160]. Increased collagen deposition is the most well-recognized ECM alteration occurring inside the tumor tissue[161–166], and collagen is considered the most regulator of the biophysical and biochemical properties of TME, impacting cancer cell polarity, migration, and signalling [167–170]. In BC, three tumor-associated collagen signatures (TACS)[171] have been described. TACS-1 is a hallmark of small tumor regions in which dense collagen is concentrated mostly in the area around the tumor. In TACS-2, straightened collagen fibres are stretched around the tumor, and thicken as the tumor volume increase. Finally, TACS-3 is characterized by radially aligned collagen fibres, favouring cell motility, and triggering tumor invasiveness and metastatic process[172]. Literature data on BC highlights the association between higher deposition of collagen and worse prognosis. It has been reported that the collagen fibre linearity enhances the motility of neoplastic cells by increasing directional persistence and restricting protrusions along such aligned fibres, thus promoting a greater distance travelled by cancer cells[173].

In-depth knowledge of the complex interplay elapsing between cancer and immune cells, as well as the tumor niche three-dimensional structure, could help to achieve promising results to overcome tumor evasion and optimize clinical outcomes of BC immunotherapies.

In this regard, we took advantage of a collaboration with the group of Doctor Emmanuel Donnadieu at the Cochin Institute in Paris to learn about new imaging techniques to explore the trafficking of adoptively transferred cells, the spatial multicellular interplay taking place in the TME of a BC mouse model, as well as the tumor three-dimensional structure, especially in terms of collagen stiffness.

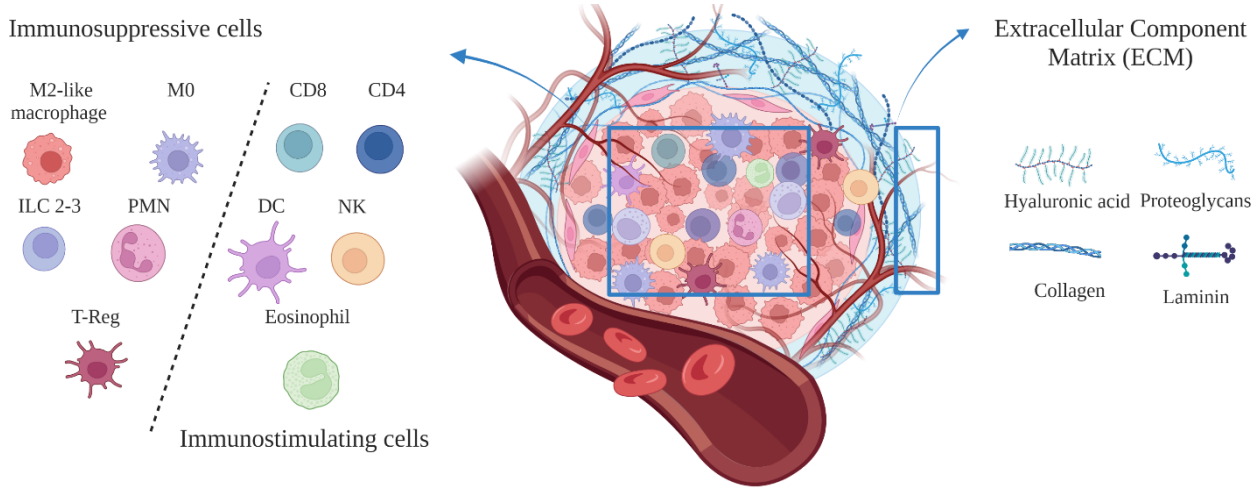

Figure 4. Major cellular and non-cellular factors characterizing the breast cancer tumor micro-environment (TME). Created with Biorender.com

Aim of the study

The present thesis work addresses four issues, as detailed below.

Objective I. Overcoming the issues related to the huge number of cells required in the clinical setting to treat cancer patients. We aimed to optimize a serum-free protocol using the G-Rex® devices to expand CIK cells in large numbers, minimizing the complexity of downstream processing and being easily reproducible under Good Manufacturing Practice (GMP) conditions.

Objective II. Enhancement of the CIK cell therapeutic efficacy against B-cell malignancies. We combined CIK cells derived from B- cell lymphoma patients with anti-CD20 clinical-grade mAb to trigger a potent ADCC activity.

Objective III. Address the combinatorial therapeutic strategy to Her-2/neu^{+} breast cancer. We investigated the improvement of CIK cell cytotoxicity both with the mAb TRS and the bsscFv Her2xCD3.

Objective IV. Investigation of the tumor microenvironment in a breast cancer model. We focused on the interactions elapsing between cancer and immune cells in the tumor niche and on its three-dimensional structure, in terms of ECM stiffness.

2. Material and methods

2.1 Study approval

Patient samples were obtained after informed consent from the Hematology Department, San Bortolo Hospital, Vicenza, Italy (Ethical Committee act n. 104/18 of 11/12/2018) and from Padua Hospital, Italy (Ethical Committee act n. 3529/AO/14). All the procedures involving animals and their care conformed with institutional guidelines that comply with national and international laws and policies (D.L. 26/2014 and subsequent implementing circulars), and the experimental protocol (Authorization n. 118/2019-PR) was approved by the Italian Ministry of Health.

2.2 Generation and expansion of CIK cells

2.2.1 Healthy donors

CIK cells were obtained from anonymized human buffy coats provided by the Blood Bank of Padua Hospital in Italy. PBMCs were isolated by density gradient centrifugation (300 g for 20 min) with Lymphoprep™ (STEMCELL Technologies Inc., BC, Canada). Cells from each donor were cultured in parallel in G-Rex® devices (Wilson Wolf, St Paul, MN, USA) or in conventional T-flasks at 37°C in a 5% CO_2 incubator. With regards to G-Rex® devices, G-Rex6, G-Rex6M, and G-Rex 100M were evaluated. G-Rex6 and G-Rex6M are characterized by the same surface area of the well (10 cm^2), but a media capacity of 40 mL and 100 mL, respectively. On day 0, PBMCs were seeded in both G-Rex6 and G-Rex6M at a density of $2.5x10^5$ cells/cm^2 ($2.5x10^6$ cells/well) in 40 mL and 100 mL, respectively, of X-VIVO™ 10 medium (Lonza, Basel, CH) supplemented with 1% Penicillin/Streptomycin (Lonza, Basel, CH). On day 7, cells cultured in G-Rex6 were transferred into a new G-Rex6M ($2.5x10^6$ cells/well) adding 60 mL of fresh media supplemented with 500 IU/mL of rhIL-2; this culture condition was named G-Rex6-6M. Conversely, cells plated in G-Rex6M did not undergo any cell density adjustment or replenishment of media. For the expansion in conventional T-flasks, PBMCs were seeded at day 0 in T25 non-treated flasks for suspension cell cultures (Nunc™ EasYFlask™, Thermo Fisher, MA, USA) at a density of $5x10^6$ cells/mL ($50x10^6$ cells in 10 mL medium) in either X-VIVO 10 medium supplemented with 1% Penicillin/Streptomycin, or in Roswell Park Memorial Institute (RPMI)-1640 medium (Euroclone, Pero, MI, IT) containing 10% heat-inactivated fetal bovine serum (FBS, Gibco, Thermo Fisher, Waltham, MA USA), 1% Penicillin/Streptomycin, 1% U-glutamine, 1% Hepes buffer (all from Lonza, Basel, CH). On day 4, and every 3-4 days, the cell density was adjusted to $1.5x10^6$ cells/mL and cells were transferred to T75 flasks when needed. In all of the culture conditions, the culture medium was supplemented at

day 0 with 1,000 IU/mL of rhIFN-γ (R&D, Minneapolis, MN, USA) and 24 hours later with 50 ng/mL of CD3 pure human-functional grade (Miltenyi Biotec, CA, USA). rhIL-2 (Proleukin, Novartis, Basel, CH) was added to the culture on days 1,7, and 14. Growth, viability, phenotypic profile, and cytotoxic activity of cells cultured under different conditions were evaluated on days 7, 14, 21, and 28. Viability was assessed by Trypan blue exclusion test. Fold expansion was calculated by dividing the number of cells yielded at each time point by the number of cells seeded at day 0.

2.2.2 Patients

PBMCs from B-cell malignant patients were obtained after informed consent and seeded in G-Rex6M at a density of $5x10^5$ cells/cm^2 ($5x10^6$ cells/well) in 40 mL of X-VIVO 10 medium supplemented with 1% Penicillin/Streptomycin and rhIFN-γ (R&D, Minneapolis, MN, USA). After 24 hours cells were stimulated with 50 ng/mL of CD3 pure human-functional grade (OKT-3, Miltenyi Biotec, CA, USA). Starting from day 1 and every 3-4 days, 500 IU/mL of rhIL-2 (Proleukin, Novartis, Basel, CH) was added to the culture. Where indicated, in CIK cells generated from patients the CD3xCD19 bispecific antibody (BsAb) blinatumomab (Blina) was added to the culture at 1 μg/mL in addition to the CD3 antibody (BL-CIK protocol). Growth, viability, phenotypic profile, and cytotoxic activity of cells cultured under different conditions were evaluated on days 7 and 14. Viability was assessed by Trypan blue exclusion test.

2.3 Tumor cell lines

K562 (chronic myelogenous leukemia) from American Type Culture Collection (ATCC) and Raji (Burkitt lymphoma) cell lines were cultured in RPMI 1640 (Euroclone, Milan, IT) completed with 10% heat-inactivated FBS (Gibco, Thermo Fisher, MA, USA), 1% ultra- glutamine, 1% N-2-hydroxyethyl piperazine-N'-2-ethane sulfonic acid (HEPES) buffer, 1% penicillin/streptomycin (all from Lonza, Basel, CH). The human breast adenocarcinoma cell lines HCC1569, HCC1419, and SK-BR-3 were obtained from ATCC and cultured in complete RPMI. MCF-7 human breast cell line was cultured in Eagle's Minimum Essential Medium (EMEM) supplemented with 0.01 mg/ml human recombinant insulin (Sigma-Aldrich, Merck, Missouri, USA), 10% heat-inactivated FBS (Gibco, Thermo Fisher, Massachusetts, USA), 1% ultra-glutamine, 1% HEPES buffer, and 1% penicillin/streptomycin (Lonza, Switzerland). T-47D human breast cancer cell line was cultured with complete RPMI with 0.007 mg/mL human recombinant insulin (Sigma-Aldrich, Merck, Missouri, USA). All tumor cell lines were maintained at 37°C, 5% CO2, and sub-cultured every 3-4 days.

2.4 Flow cytometry for phenotypic characterization

CIK cell phenotype was analyzed using multi-color flow cytometry. In brief, cells were harvested and stained using the following antibodies: CD3-BV510 (clone UCHT1), CD4-BV650 (clone SK3), CD8-BV421 (clone RPA-T8), NKp30-BV650 (clone P30-15), CD244-BV421 (clone 25235), CD62L-FITC (clone DREG-56), CD45RA-PerCP (clone HI100), CD45RO-BV650 (clone UCHL1) and CCR7-Alexa647 (clone 150503) from BD Bioscience; CD56-PE (clone HCD56), NKG2D-APC (clone 1D11), NKp44-APC (clone P44-8) and CD27-FITC (clone O323) from BioLegend. Dead cells were excluded using Fixable Viability Stain 780 (FVS780; BD Bioscience), and the positivity to the evaluated markers was determined by gating on $CD3^{+}CD56^{+}$ or $CD3^{+}CD56^{-}$ cells. Naive/memory subsets were identified according to their expression of CD45RA and CD62L: naïve, N, $CD62L^{+}CD45RA^{+}$; central memory, $CD62L^{+}CD45RA^{-}$; effector memory (EM), $CD62L^{-}CD45RA^{-}$; effector memory RA^{+} (EMRA), $CD62L^{-}CD45RA^{+}$. Flow cytometry was performed using Celesta flow cytometer and DIVA software (BD Bioscience). Data analyses were carried out with FlowJo software (Treestar).

2.5 Her2xCD3 binding property

The binding property of the bsscFv Her2xCD3 was evaluated by flow cytometry. Her2xCD3-Cy5.5 fluorescent antibody was obtained after the conjugation with VivoTag® 680XL (PerkinElmer, Massachusetts, USA), according to the manual instructions. The binding property of Her2xCD3-Cy5.5 was assessed by incubating 500000 of both target and CIK cells with different doses of the bsscFv-Cy5.5 for 1 hour. FACS quantification was carried out on the APC-positive cell population. To evaluate the simultaneously bispecific binding of Her2xCD3, effector CIK, and tumor cells were labeled with 5 µM CellTrace CFSE and 5 µM CellTrace Violet Cell Proliferation Kit (Thermo Fisher, Massachusetts, USA), respectively, for 20 minutes at 37°C. Hence, labeled cells were co-cultured with different concentrations of Her2xCD3 for 30 minutes at 4°C. FACS analyses were carried out by gating the double-positive CellTrace $Violet^{+}$ and CellTrace $CFSE^{+}$ cell populations.

2.6 Calcein-AM-release and Cell Trace viability assay to assess CIK cells cytotoxicity

CIK cells harvested between days 14 and 21 were challenged against tumor cell lines or a single cell suspension, respectively using a standard calcein-acetoxymethyl (calcein-AM) release assay or a Viability FACS-based assay. 10^{6} above-described cancer cell lines were labeled with 3.5 µM calcein-

AM (Merck, Germany) in cRPMI medium and plated at the indicated E/T ratios in presence of 1 µg/mL of the anti-CD20 antibodies rituximab (RTX), or 1 µg/mL of OBI or 1 µg/mL IgG1 isotype control antibody (Iso), or 1 µg/mL of the bsscFv Her2xCD3, the mAb Transtuzumab (TRS) or the bsAb Blina. After a 4-hour incubation at 37°C, the plates were centrifuged and 100 µL of supernatant collected from each well was transferred into an OptiPlate-96 Black plate (PerkinElmer, Waltham, MA, USA) to measure the released fluorescence using VICTOR Multilabel Plate Reader (PerkinElmer, Waltham, MA, USA). The results are expressed as % Specific Lysis = (experimental release – spontaneous release)/(maximal release–spontaneous release) x 100. Maximum and spontaneous releases were obtained by incubating target cells with 3% Triton X-100 (Merck, Germany) or complete RPMI medium and relative mAbs, respectively.

For cytotoxicity assessment on primary samples, target cells were labeled with 5 µM of CellTrace Violet Cell Proliferation Kit (Thermo Fisher, Massachusetts, USA) for 20 minutes at 37°C, and incubated with CIK cells at a 25:1 Effector/Target (E/T) ratio for 6 hours at 37°C. Cells were then stained with BD Horizon Fixable Viability Stain 780 (FVS780, BD Bioscience) and with Annexin V (APC, Thermo Fisher, Massachusetts, USA) according to the manufacturer instructions. The percentage of $FVS780^+$ necrotic cells and Annexin V^+ apoptotic cells was measured in flow cytometry within the $CellTrace^+$ target cells. The Her2xCD3 dose-dependent lytic activity of CIK cells was evaluated at a fixed 10:1 E/T ratio and indicated bsscFv dilutions.

2.7 Real-Time Cell Analysis (RTCA) measuring the tumor cell loss of impedance induced by CIK cells cytotoxicity

To test the cytotoxicity in real time we took advantage of the Agilent xCELLigence Real-Time Cell Analysis-Single Plate (RTCA-SP) instrument, which uses label-free cellular impedance to continuously monitor cell health, behaviour, and function with high accuracy, sensitivity, and reproducibility. A total of 50000 adherent tumor $Her2^+$ cells/well were added to 16 -well micro-E-plate at 37°C in a 5% CO_2 incubator to monitor the impedance of the cells every 20 minutes for up to 60 hours. $Her2^+$ cells were resuspended in 100 µl of complete RPMI medium and seeded for 20 h until the linear growth time phase, thereafter effector CIK cells together with 1µg/ml of Her2xCD3, TRS, and a corresponding control construct (CD19xCD3) were resuspended in 100 µl of complete RPMI medium and added at the previously titrated optimal E/T ratios. The loss of impedance of tumor cells was measured as the killing capability of effector CIK cells. As a control, tumor cells were incubated with a 3% TRITON-X solution and with the mentioned above antibodies.

2.8 Quantification of cytokine release by MACSPlex Cytokine Kit® after a CIK and target cells co-culture

The assay was designed to determine soluble cytokines on the cell culture supernatant. The analysis was based on the MACSPlex Cytokine 12 Capture Beads consisting of 12 bead populations that have been coated with capture antibodies specific for the following cytokines: GM-CSF, IFN-α, IFN-γ, IL-2, IL-4, IL-5, IL-6, IL-9, IL-10, IL-12p70, IL-17A, and TNF-α. After a 20-hour co-culture of CIK and MCF-7 cells at 10:1 effector/target ratio, the supernatant was incubated with the antibody-coated MACSPlex Capture Beads and analyzed by flow cytometry. Standards of known quantities of given analytes were provided in the kit and were used for the quantification of the analytes. The FACS analysis of these complexes was based on the fluorescence characteristics of both the MACSPlex Capture Bead and the detection reagent.

2.9 Fluorescent multiplex immunohistochemistry (fmIHC)

fmIHC staining was performed using the Opal seven-colour manual kit (Akoya Biosciences) following the manufacturer's instructions. 4 µm-thick formalin-fixed and paraffin-embedded (FFPE) tissue sections were deparaffinized in Clearene (Leica Biosystems) and rehydrated by serial passages in graded ethanol. Before the multiplex staining, a monoplex staining on a positive control tissue (human tonsil) was mandatory to determine the optimal labelling conditions for each marker. To ensure the fixation of the sample on the glass slide during the several serial steps of staining, we performed a 20-minute step in 10% neutral buffered formalin (Sigma). The heat-induced epitope retrieval (HIER) with Target Retrieval Solution pH9 (Dako) or pH6 (Akoya Biosciences), depending on the primary antibody, was carried out at the beginning of each serial staining, and non-specific sites were blocked with Protein Block Serum-free (Dako) for 10 minutes before applying primary antibodies. To characterize adoptively transferred immune cells and tumor cells, MCL3-PDX samples were stained for anti-CD56 (123C3, 1:30, DAKO/Agilent), anti-CD3 (F.7.2.38, 1:400, DAKO/Agilent) and anti-CD20 (L26, 1:400, DAKO/Agilent). The anti-mouse+rabbit Horseradish Peroxidase (HRP)-conjugated secondary antibody (Akoya Biosciences) was added for 10 minutes at room temperature, followed by 10 minutes with specific Tyramide Signal Amplification (TSA)-conjugated Opal fluorophore (Akoya Biosciences) (Fig.5). In the end, the slides were counterstained with spectral DAPI (Akoya Biosciences) and mounted using Vectashield Hardset mounting medium (Vector Labs).

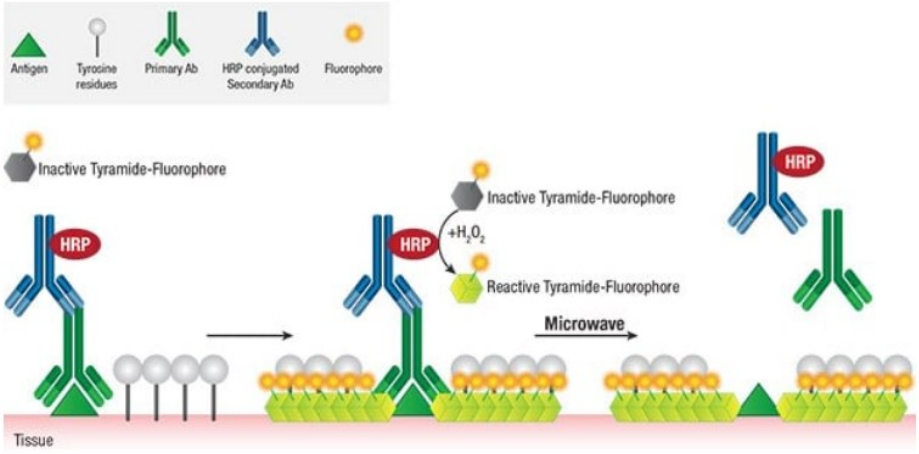

Figure 5. **Overview of Tyramide signal amplification (TSA).** Adapted from Cell Signaling technologies.

2.10 Multispectral imaging analysis

Multiplex stained slides were imaged using the Mantra Quantitative Pathology Workstation (Akoya Biosciences) at 20X magnification. The inForm Image Analysis software (version 2.4.2, PerkinElmer) was used to unmix multispectral images using a spectral library built from the acquisition of single fluorophore-stained control tissues and containing fluorophores-emitting spectral peaks. A selection of representative multispectral images was used to train the inForm software to create the analysis algorithm. Tumor tissue was segmented based on the expression of anti-CD20 marker, to differentiate the tumor area from the surrounding stroma. Single cells were segmented by nuclear counterstaining and the cell phenotyping was based on the cluster differentiation (CD) expression. The cellular density (cell counts/mm^2) was reported as the mean of all acquired fields for each slide, and an average of 80 snaps was collected for each experimental group.

Here above, we explain in detail the *ex vivo* tumor slice assay and the microscopy techniques I learned during my stage at the Institut Cochin in Paris.

2.11 Tumor slice imaging assay for the *in situ* study of multicellular interactions

Tumor samples were fixed ON at 4 °C with periodate–lysine–paraformaldehyde (PLP) to fix glycoprotein antigens and allow immunohistochemical detection of membrane antigens of the immune system cells[174]. Next, the samples were washed and embedded in PBS 5% low-gelling temperature agarose (type VII-A; Sigma-Aldrich) and 350 µm-thick slices were obtained with a vibratome (VT 1000 S; Leica) in a bath of ice-cold PBS[175]. Non-specific sites on the tissue slices

were blocked with a PBS 0,5% BSA,0,05% TRITON-X solution for 10 minutes, then the slides were stained with conjugated antibodies for 15 minutes at 37°C or ON at 4 °C (Fig.6). The following anti-mouse antibodies were used: CD8a-AF647 (clone 53-6.7), CD4-FITC (clone RM2-5), and CD326-BV421 (EpCam, clone G8.8), CCR2-APC from BD Bioscience; CD11b-FITC (clone M1/70), gp38-AF488 (Podoplanin, clone 8.1.2001), and CD279-BV421 (PD-1, clone 29F.1A12) from BioLegend; Fibronectin- AF488 (clone FN-3), F4/80-AF488 and F4/80-PE (clone CI:A3-1) from BIORAD; and CX3CR1-PE (CD181) from Acris. In the end, the slides were mounted with Antifade Vectashield (Vector Labs) and imaged with an inverted confocal with an advanced spinning disk unit contributing to a large field of view and the highest resolution (Fig.6).

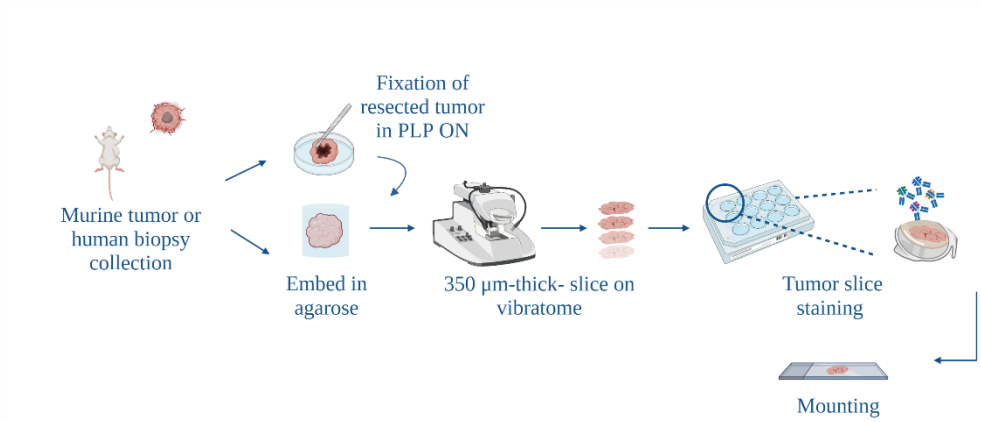

Figure 6. Tumor slice staining protocol. Created with Biorender.com

2.12 Spinning disk confocal laser (SDCLM) imaging and Z-stack analysis

In the spinning disk confocal laser microscopy (SDCLM) an expanded beam illuminates an array of microlenses arranged on a collector disk. Each microlens presents an associated pinhole laterally co-aligned on a second pinhole disk and axially positioned at the focal plane of the microlenses. The disks are fixed to a common shaft that is driven at high speed by an electric motor. When the disks spin and the scanner is coupled to a microscope with the pinhole disk located in its primary image plane, an array of focused laser beams scan across the specimen (Fig.7). Furthermore, the use of a very high quantum efficiency camera (CDD camera) as a detector allows for overcoming the considerable photobleaching and photodamage caused by the poor efficiency of the photomultiplier tubes (PTMs) used to detect light in conventional confocal laser scanning microscopy (CSLM). 350 µm-thick tumor slices were imaged using an inverted spinning disk confocal microscope (Olympus IXplore, CSU-W1 T1; Yokogawa), equipped with a CDD camera (ORCA-Flash, Hamamatsu), (IMAG'IC core facility – Institut Cochin). Images were acquired with a 20x objective and a 60x oil

immersion objective. The cellSens acquiring software (IX3-DSU, IX83F) was used to set the following parameters: laser power, time of exposure, pixel binning, and z-stack values were adapted to reconstruct the entire thickness of the tissue. Z-stacked images were then analyzed in two-dimensional visualization, by compressing the z information into a single plane with the maximum intensity Z projection performed with ImageJ software.

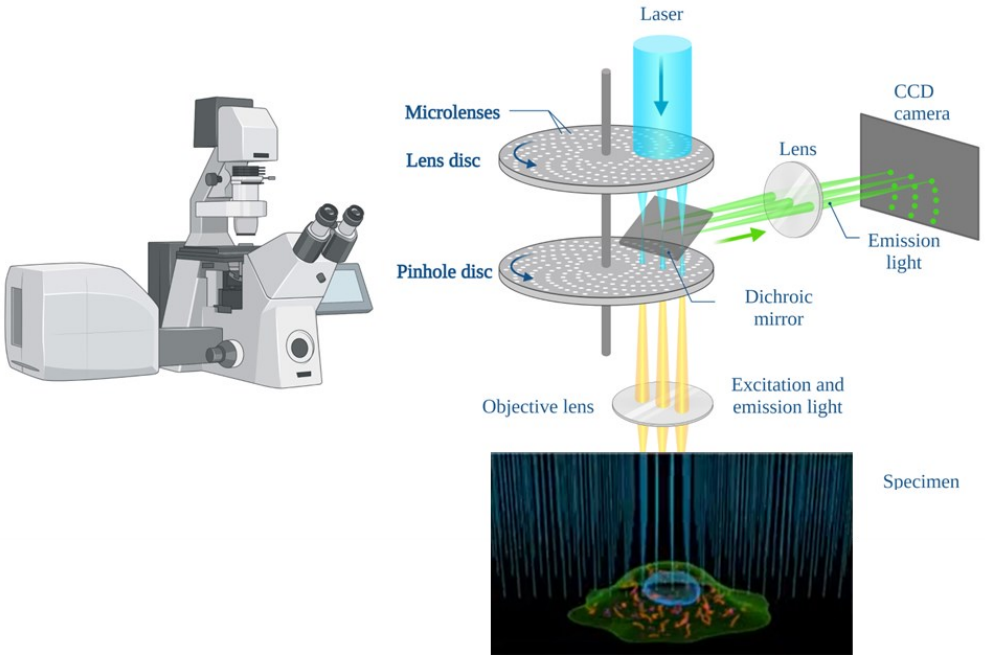

Figure 7. Spinning disk laser confocal microscope (SDLCM). Adapted and created with Biorender.com

2.13 Second Harmonic Generation (SHG) microscopy

The label-free second harmonic generation (SHG) microscopy within the nonlinear optical material requires that two photons are upconverted into one emerging visible photon at exactly twice the energy of the excitation laser. Thus, this phenomenon is based on the noncentrosymmetric assembly of these two photons, therefore called "harmonophores", in a permanent dipole moment [176,177] (Fig.8). For the collagen quantification in tumor samples, 15 µm-tick FFPE tissue slides representative of three different 4T1 breast tumor sections were analyzed for each mouse to reconstruct tissue heterogeneity. Samples were imaged with 2-photon Leica SP8 DIVE FLIM microscope (IMAG'IC core facility – Institut Cochin) with the following Leica parameters. SHG (collagen structure) signal was detected in epi-collection through 440/60 nm bandpass filters, respectively, by NDD PMT detectors (Leica Microsystems) with a constant voltage supply, at constant laser excitation power, allowing direct comparison of SHG intensity values. To assess the natural fluorescence, samples were illuminated at a wavelength of 900 nm and two-photon excited fluorescence (TPEF) emission was measured at a wavelength of 500 nm. Immersion objective 25x/0.95 W. Analyses were carried out

by applying a published collagen scoring method [178]. Treatment of images was performed with ImageJ software and included: the split of SHG and TPEF channels, the threshold setting (Threshold TPEF 28-225, Threshold SHG 25-225, algorithm run on 5 random images) with a black background, and the convert to mask option visualization, thus the SHG score measurement. The collagen score was calculated as the collagen density represented by the number of SHG pixels divided by the total number of pixels in the imaged area. Likewise, 15 µm-tick FFPE tissue slides were analyzed as described above for the collagen evaluation in the metastatic lung of 4T1 breast tumor-bearing mice.

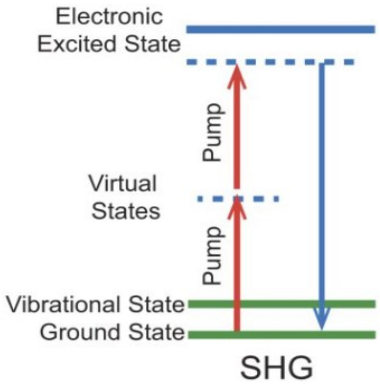

Figure 8. Energy level diagram for the SGH imaging mechanism.

2.14 *In vivo* studies

$CD20^+$ leukaemia mouse model

Six-to-eight-week-old female NOD/SCID common γ chain knockout (NSG, The Jackson Laboratory, ME, USA) mice maintained at the Oncologic Institute of Veneto SPF animal facility were used for all the experiments. The lymphoma model was generated in NSG mice by subcutaneous (s.c.) injection with $1x10^6$ MCL3-PDX cells. Seven days later, when the tumors became palpable and reached a similar size in all animals, mice were randomly assigned to experimental groups. Mice were treated daily, for 7 consecutive days, by i.v. co-administration of $10x10^6$ CIK cells resuspended with 10 mg/kg of the anti-CD20 mAb OBI (CIK+OBI group); $10x10^6$ CIK cells resuspended with 10 mg/kg of the isotype control mAb (CIK+Iso group); 10 mg/kg of OBI (OBI group), or left untreated. Mice were sacrificed when subcutaneous masses exceeded an 800 mm^3 volume or appeared ulcerated. Tumor growth was monitored by caliper measurement and the volume was calculated using the formula: Tumor volume (mm^3) = D×d2/2, where D and d represent the longest and the shortest diameters, respectively.

$Her\text{-}2^+$ breast mouse model

For the biodistribution study of Her2xCD3, $5x10^6$ MCF-7 cells were injected s.c in 8-week-old NGS female mice. When tumors were palpable ($150mm^3$), the Cy5.5fluorophore-conjugated Her2xCD3 was administrated i.v. and the fluorescent signal was registered at two-hour intervals for two days with the eXplore Optix MX2. For the metastatic breast MCF-7 mouse model, $3x10^6$ MCF-7/Luc cells transduced with a lentiviral vector coding for the Firefly Luciferase reporter gene[72] were injected subcutaneously with 17β-estradiol in 8 weeks-old female NGS mice. 1 µg/mouse 17β-estradiol (Sigma) was resuspended in a peanut oil solution and administrated intraperitoneally every 2- or 3-days supporting cell proliferation as MCF-7 is known to be an estrogen receptor (ER)- sensitive cell line. Mice were imaged every week for tumor progression using bioluminescence imaging (Xenogen IVIS ® spectrum).

3. Results

3.1 Objective I

Optimization of CIK cells production under Good Laboratory Practice-grade conditions in G-Rex ® culture devices

CIK cells efficiently expand in gas-permeable culture G-Rex6M well plate devices using serum-free medium

To set up a serum-free expansion protocol for CIK cells in G-Rex devices, PBMCs were seeded at day 0 in either G-Rex6 plates and transferred 7 days later into a G-Rex6M device (G-Rex6–6M protocol) or G-Rex6M without any further cell density adjustment. To compare the results to the standard culture in conventional T-flasks, PBMCs were plated in either X-VIVO or complete RPMI according to our published protocol [12]. After 28 days of culture, the cell yield obtained was significantly different among culture conditions, as indicated by the cell growth curve in Figure 9-A. The culture of CIK cells in X-VIVO serum-free medium using G-Rex6-6M led to a more efficient cell expansion compared to all of the other culture protocols, yielding a mean of $1.88\pm1.77x10^9$ total cells in 28 days starting from only $2.5x10^6$ cells, which corresponds to a 752-fold increase (Fig.9-B). However, the expansion of CIK cells in X-VIVO serum-free medium was significantly reduced when G-Rex6M or T-flasks were employed. Indeed, in both the latter cases, the cell growth curve quickly reached a plateau starting from day 14 (Fig.9-A), leading to a reduced overall fold increase of 124

and 2.3, respectively (Fig.9-B). The use of a complete RPMI medium led to a higher cell yield in the first 14 days, reaching a peak on day 21, but on day 28 the number of cells dramatically decreased with a mean of $0.42\pm0.28x10^9$ total cells obtained from $50x10^6$ cells, corresponding to 8.4-fold increase. Additionally, cells cultured according to the G-Rex6-6M protocol showed improved long-term viability over the entire culture period, whereas increased cell death was observed in G-Rex6M and in X-VIVO T-flasks, especially at the last time point tested (P=0.008 and P=0.031, respectively; (Fig.9-C)).

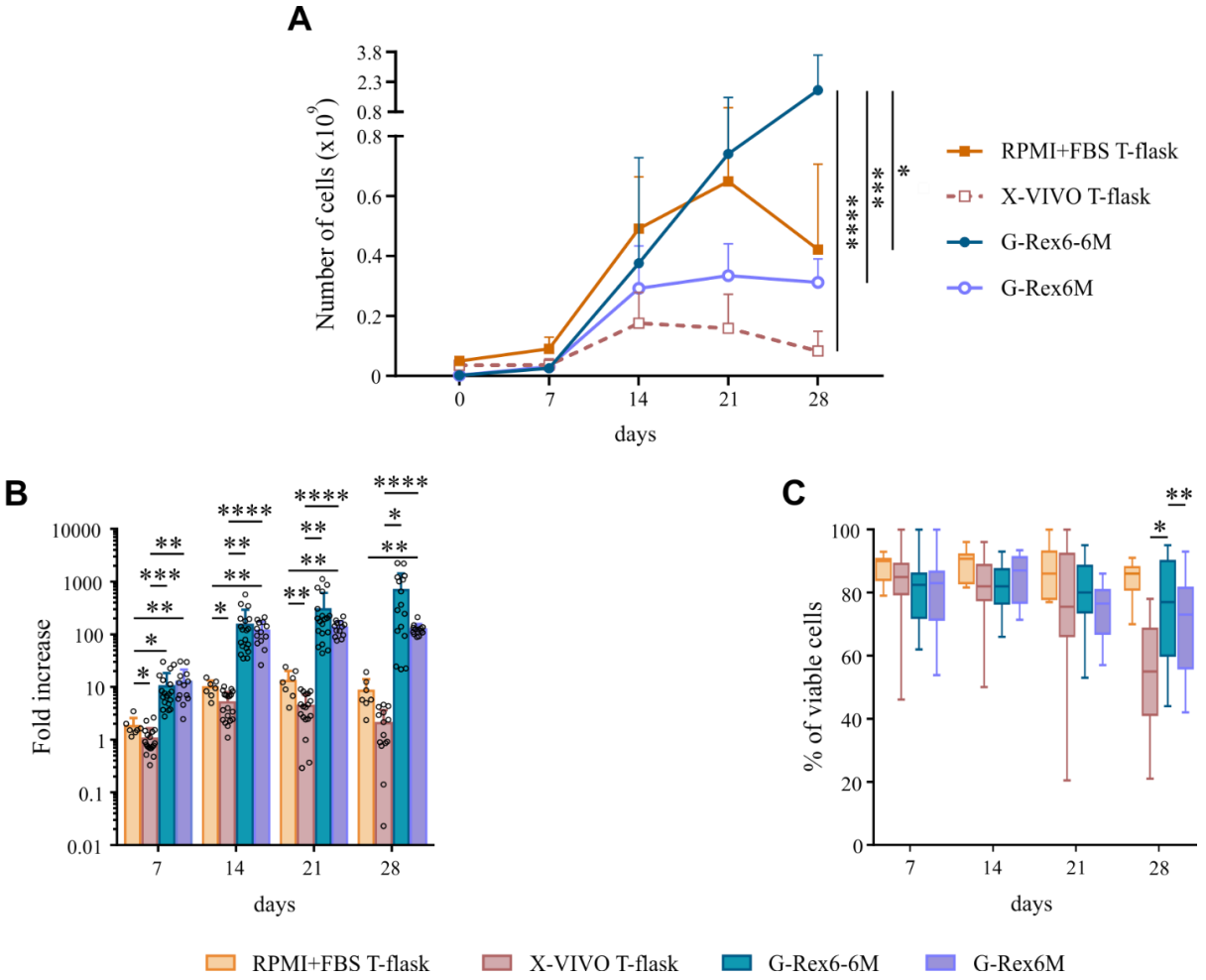

Figure 9. Assessment of CIK cells expansion and viability. On days 7, 14, 21, and 28, CIK cells cultured in T-flasks (n=7 in RPMI+FBS; n=19 in X-VIVO), G-Rex6-6M (n=19), and G-Rex6M (n=13) were sampled and counted to evaluate (**A**) cell expansion (the statistics reported refers to day 28) and to calculate (**B**) the fold-increase. (**C**) Cell viability was calculated as a percentage of viable cells at different time points. Data were analyzed by one-way (**A**) or two-way (**B** and **C**) ANOVA with Bonferroni's correction (****, P<0.0001; ***, P<0.001; **, P<0.01; *, p<0.05).

CIK cells cultured in G-Rex showed a naïve-like phenotype compared to standard culture protocols, but a similar lytic activity *in vitro*

Multi-color flow cytometry analysis was performed to characterize in detail the phenotype of CIK cells cultured under different conditions. After 14 days of culture, the bulk CIK cell culture was fully characterized for the expression of several T and NK classical markers, as is customary in our experiment routine [12,51](Fig.10). The percentage of $CD3^{+}CD56^{+}$CIK cells was comparable among the four different culture systems, but they expanded more efficiently in G-Rex6–6M, resulting in the highest percentage on day 21 (mean: 45.19 ± 14.53%) and day 28 (mean: 40.01 ± 17.38%) (Fig.10-A).

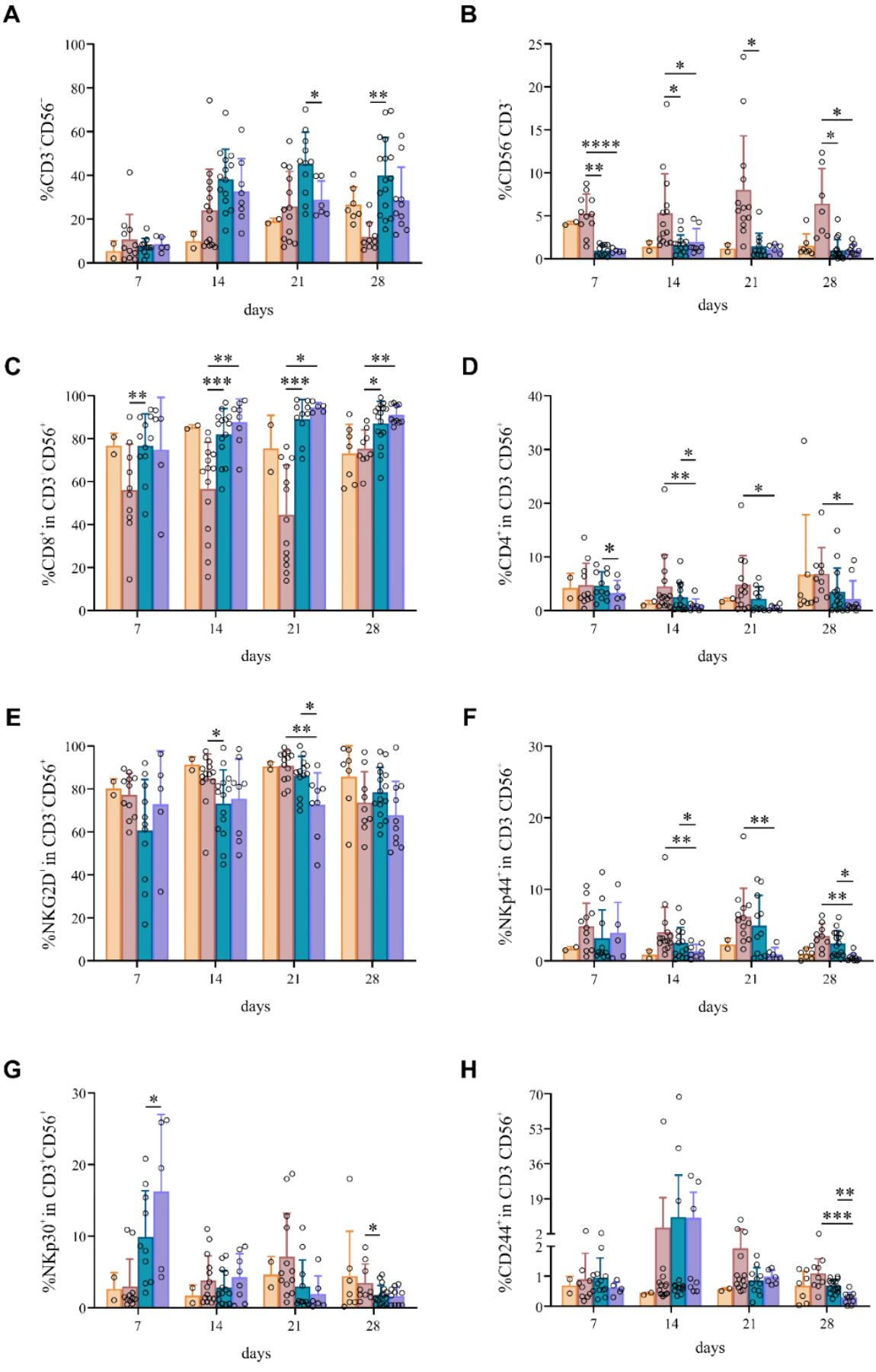
A
%CD3+CD56-
days
B
%CD56+CD3-
days
C
%CD8+ in CD3-CD56+
days
D
%CD4+ in CD3-CD56+
days
E
%NKG2D+ in CD3-CD56+
days
F
%NKp44+ in CD3-CD56+
days
G
%NKp30+ in CD3+CD56+
days
H
%CD244+ in CD3-CD56+
days
RPMI+FBS T-flask
X-VIVO T-flask
G-Rex6-6M
G-Rex6M

Figure 10. Phenotypic characterization of CIK cell cultures. CIK cells expanded according to the different culture protocols and were analyzed by flow cytometry on days 7, 14, 21, and 28 for their phenotypic profile. (**A**) Percentages of $CD3^+CD56^+$ CIK cells and (B) $CD3^+CD56^+$ NK cells were assessed within the bulk cultures. The expression of (**C**) CD8, (**D**) CD4, (**E**) NKG2D, (**F**) NKp30, (**G**) NKp44 and (**H**) CD244 markers was evaluated within the $CD3^+CD56^+$ subset. Results show the mean expression ± standard deviation. Data were analyzed by two-way analysis of variance with Bonferroni correction. *P < 0.05; **P < 0.01; ***P < 0.001; ****P < 0.0001.

At the end of the expansion period (day 28), CIK cells were stained for CD62L and CD45RA to identify the four main subpopulations related to memory and effector functions—namely, naïve (N, $CD62L^+CD45RA^+$), central memory (CM, $CD62L^+CD45RA^-$), EM ($CD62L^-CD45RA^-$) and effector memory RA^+ (EMRA, $CD62L^-CD45RA^+$)—within both $CD3^+CD56^+$ and $CD3^+CD56^-$ cell subsets. CIK cell culture from G-Rex6–6M and G-Rex6M presents a significantly higher proportion of $CD3^+CD56^+$ naïve cells (34.6 ± 12.4% and 42.1 ± 19.2%, respectively) compared with X-VIVO T-flasks, which comprised a mean of 14.7 ± 7.1% naïve $CD3^+CD56^+$ cells (P = 0.0286 and P = 0.0016, respectively) (Fig.11 A-B). Likewise, the phenotype of the precursor $CD3^+CD56^-$ T cell counterpart appeared to be less differentiated; in particular, in G-Rex6–6M and G-Rex6M cultures, the $CD62L^+$ $CD45RA^+$ naïve cell subset accounted for 59.9 ± 19.4% and 50.5 ± 16.4% of total T cells, respectively (Fig.11 A-B). Conversely, $CD3^+CD56^+$ CIK cells cultured in T-flasks with complete RPMI appeared mostly as fully differentiated EM (82.3 ± 8.4%), whereas the percentage of this subset was significantly reduced in X-VIVO T-flasks (42.7 ± 15.8%; P < 0.0001) (Fig.11 A-B). This tendency to an immature-like phenotype observed under G-Rex culture condition was confirmed by the expression of the lymphoid homing marker CCR7, which is associated with a naïve or early memory phenotype. Indeed, CCR7 was significantly more expressed on $CD3^+CD56^+$ CIK cells cultured in G-Rex6–6M and G-Rex6M as compared with both protocols employing T-flasks (Fig.11-C). Accordingly, the antigen-experienced cell marker CD45RO was more expressed in cells expanded in conventional T-flasks with either complete RPMI or X-VIVO (Fig.11-D), whereas the co-stimulatory marker CD27 was significantly higher in G-Rex6–6M and G-Rex6M (Fig.11-E).

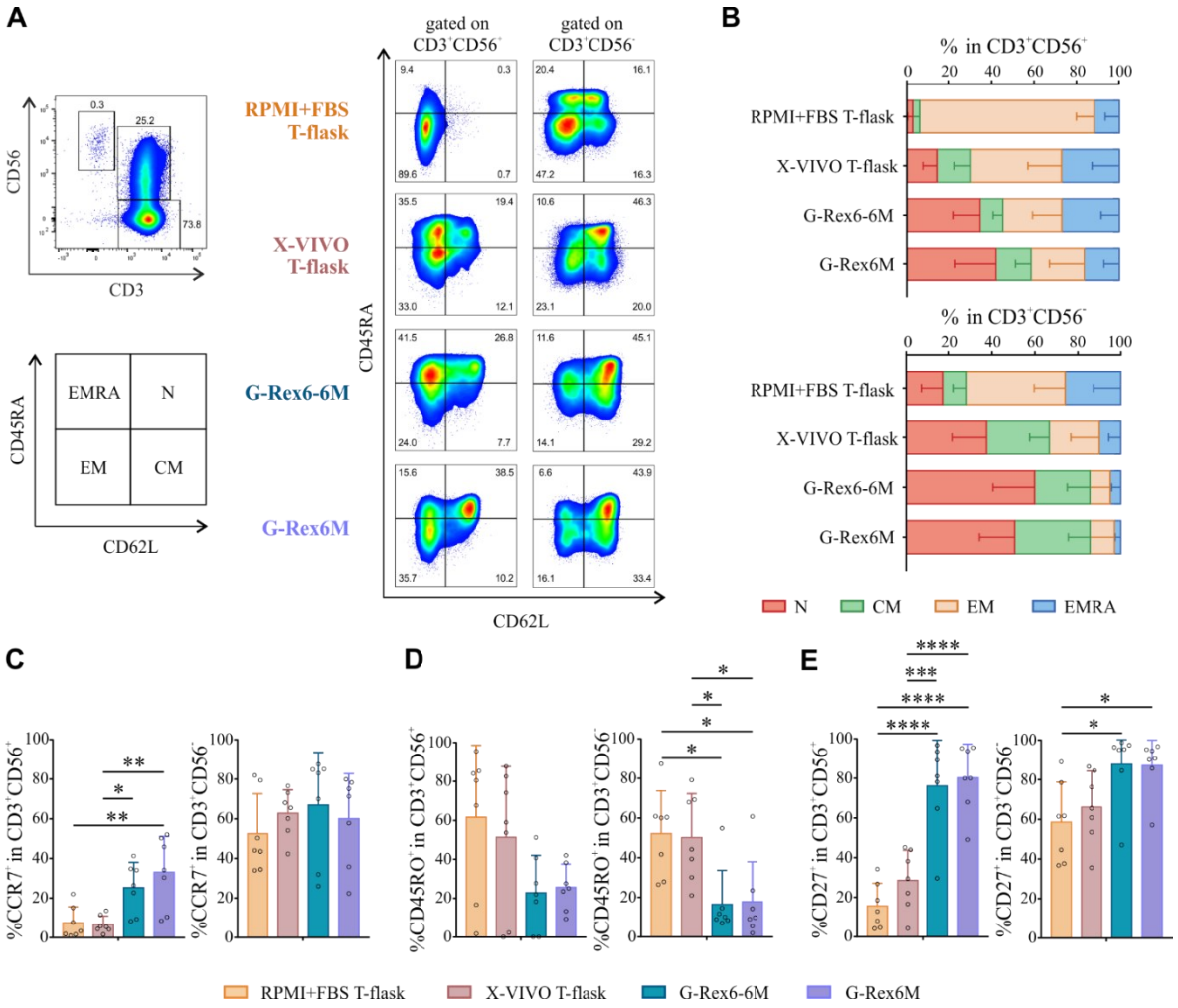

Figure 11. Naïve/Memory profile analysis of CIK cell cultures. Cells were stained for CD3, CD56, CD62L and CD45RA to identify naïve (N), central memory (CM), effector memory (EM), and effector memory RA$^+$ (EMRA) within both CD3$^+$CD56$^+$ and CD3$^+$CD56$^-$ cells (n=7). (**A**) One representative dot plot of each culture condition and subpopulation is reported. Data are graphically shown in (**B**). CD3$^+$CD56$^+$ and CD3$^+$CD56$^-$ cells were also evaluated for the expression of (**C**) CCR7, (**D**) CD45RO and (**E**) CD27. Histograms show the mean expression ± SD. Data were analyzed by one-way ANOVA with Bonferroni's correction (****, P<0.0001; ***, P<0.001; **, P<0.01; *, P<0.05).

Next, we assessed the functional lytic activity of CIK cells cultured in G-Rex devices against different tumor cell lines (Fig.12). G-Rex6–6M CIK cells showed cytotoxicity that was overall similar to CIK cells cultured in all other conditions and appeared slightly reduced against only K562 target cells as compared with CIK cells cultured in X-VIVO in T-flasks (12.5:1 ratio: 40.62 ± 17.24% versus 59.27 ± 25.12%, P = 0.042). On the contrary, the killing activity of G-Rex6M CIK cells was decreased compared with X-VIVO T-flask CIK cells against K562 and MDA-MB-468 targets (Fig.12).

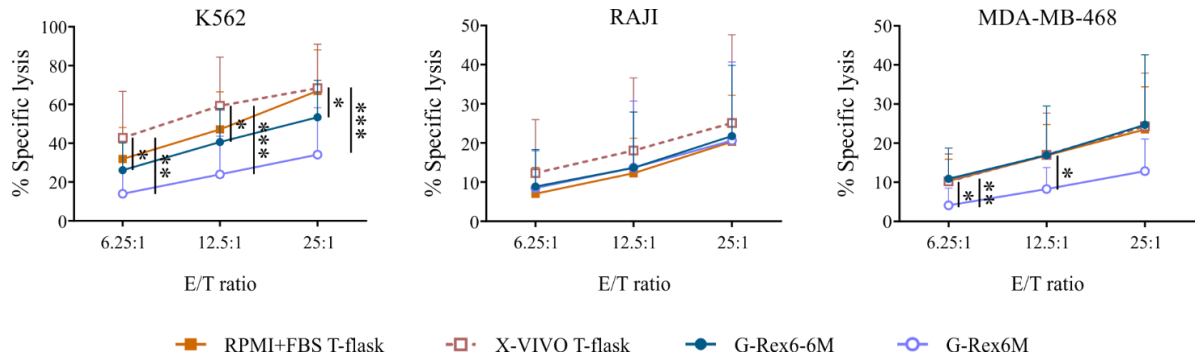

Figure 12. Analysis of CIK cells killing activity against tumor cell lines. CIK cells were challenged against K562, Raji, and MDA-MB-468 tumor cell lines. Lytic activity was measured by calcein-AM release assay between days 14 and 21 of cultures. Results show mean values ± SD of the specific lysis at different E:T ratios of CIK cells cultured in T-flasks (n=8 in RPMI+FBS; n=20 in X-VIVO), G-Rex6-6M (n=17) and G-Rex6M (n=14). Data were analyzed by two-way ANOVA test with Bonferroni's correction (***, P<0.001; **, P<0.01; *, P<0.05).

These and more data have been published in *Cytotherapy*[179].

3.2 Objective II

CIK cells and ADCC in B-cell malignancies

CIK cells can be generated in large scale from high tumor-burden patients using a blinatumomab-based protocol for the elimination of residual tumor cells

After demonstrating the therapeutic potential of healthy donor CIK cells combined with OBI against primary tumor samples, we assessed the therapeutic potentiality in an autologous setting where patients often present strong lymphopenia and a high tumor burden, testing an original protocol of CIK cells expansion that employs Blina. Effector cells were expanded from PBMCs of nine patients affected by different types of B-cell malignancies, both at diagnosis and after relapse (Table 1). Thawed (n=2) or freshly isolated (n=7) PBMCs (Table 2) were plated in serum-free medium in G-Rex devices and stimulated with IFN-γ, IL-2, and either CD3 mAb only (CIK, standard protocol) [3] or the combination of CD3 mAb and Blina (BL-CIK cells, $CD3^+$ Blina protocol). Already after 1 week, BL-CIK cells showed an enhanced expansion compared with CIK cells cultured with the standard protocol, and the difference became even more pronounced on day 14. Indeed, starting from a small number of PBMCs (5×10^6 cells), the cell yield after 2 weeks of culture was $59.3\pm39.7\times10^6$ and $11.2\pm9.8\times10^6$ cells for BL-CIK and standard protocol cultures, respectively (Fig. 13, A), with a mean fold increase of 11.9 vs only 2.5 (Table 1). Interestingly, BL-CIK cultures exhibited also a significantly improved viability (Fig. 13, B).

At day 0, samples from most patients presented an extremely high percentage of $CD19^+$ and $CD20^+$ tumor cells (mean 52.9±28.2% and 45.5±32.1%, respectively; Fig. 13, C and Table 2), which progressively decreased at day 7 in either culture conditions (Fig. 13, D). Noteworthy, a single addition of Blina at the beginning of the culture succeeded to eradicate $CD19^+$ and $CD20^+$ cells on day 14 (Fig. 13, D). On the contrary, the cells expanded in the presence of CD3 mAb only maintained a residual percentage of tumor cells, which accounted for more than 10% of the live final population in two of the patients' samples ((Fig. 13, D and Table 2). Equally important, the addition of Blina allowed a significantly increased expansion of $CD3^+$ cells from 15.2±19.8% to 97.4±2.1%, whereas in the standard protocol the resulting $CD3^+$ component was 85.1±12.0% on day 14 of (Fig. 13, D). Moreover, BL-CIK cells comprised a higher percentage of $CD3^+CD56^+$ cells (Fig. 13, E) and a slightly increased number of naïve cells (Fig. 13, F), as compared to the standard culture.

For the functional characterization, BL-CIK and standard CIK cells were challenged against the $CD20^+$ Raji cell line (Fig. 13, G). Similar to CIK cells obtained with the standard protocol, BL-CIK population not only exhibited comparable basal cytotoxicity but was also efficiently retargeted by the combination with OBI, leading to a significant increase of lysis from 26.2±9.8% to 58.9±12.8% at an E:T ratio of 50:1. Most importantly, such killing improvement was also evident when BL-CIK cells were challenged in an autologous setting. Indeed, BL-CIK combined with OBI very efficiently lysed patient PBMCs that were not susceptible to OBI alone (Fig. 13, H).

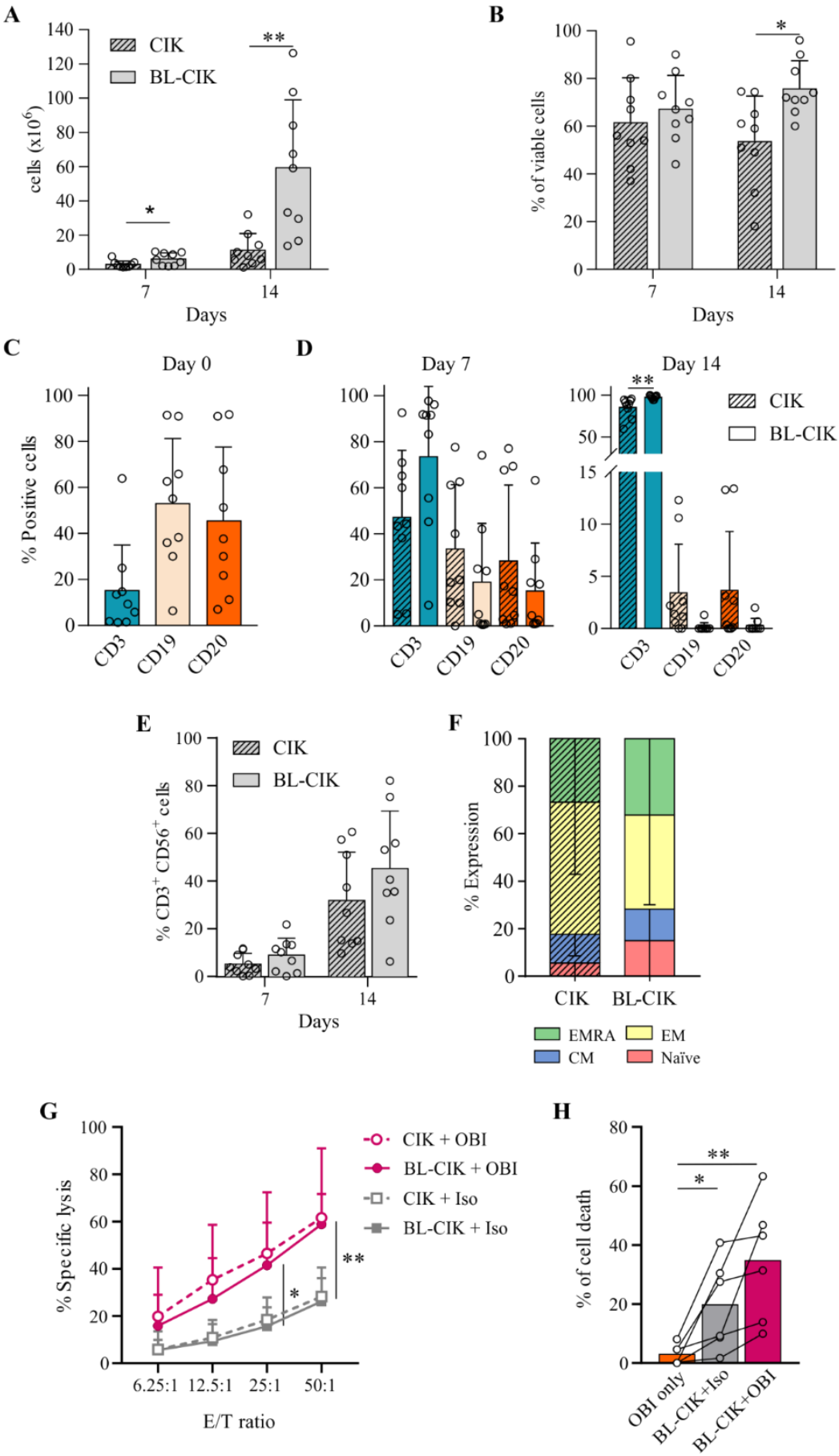
A
cells (x10^6)
CIK
BL-CIK
Days
B
% of viable cells
Days
C
Day 0
% Positive cells
CD3
CD19
CD20
D
Day 7
Day 14
CIK
BL-CIK
E
% CD3+ CD56+ cells
Days
F
% Expression
CIK
BL-CIK
EMRA
EM
CM
Naïve
G
% Specific lysis
CIK + OBI
BL-CIK + OBI
CIK + Iso
BL-CIK + Iso
6.25:1
12.5:1
25:1
50:1
E/T ratio
H
% of cell death
OBI only
BL-CIK+Iso
BL-CIK+OBI

Figure 13. Expansion and characterization of CIK cells from Lymphoma patients. (**A**) CIK cell expansion with the standard protocol (crossed bars, CIK) or with the addition of blina on day 1 (solid bars, BL-CIK). Total cell numbers were evaluated on day 7 and 14 of culture. (**B**) Cell viability was calculated as the percentage of viable cells at the two different time points. (**C**) Percentages of $CD3^+$, $CD19^+$ and $CD20^+$ cells were assessed at day 0, and (**D**) 7 and 14 days later (n=9). Data were analyzed by multiple t-test (*P<0.05, **P<0.01). (**E**) Percentages of $CD3^+CD56^+$ CIK cells within the bulk cultures expanded with the standard protocol (crossed bars, CIK) or with the addition of Blina (solid bars, BL-CIK) (n=9). (**F**) Comparison of the naïive/memory phenotype at day 14 of culture. Cells were stained with CD62L and CD45RA to identify the naive, CM, EM, and EMRA subsets within the $CD3^+CD56^+$ population (n=6). (**G**) CIK and BL-CIK cells were challenged against Raji tumor cell line in combination with Obinutuzumab or isotype antibody. Results show mean values ± SD of specific lysis at different E:T ratios. Lytic activity was measured by calcein-AM release assay on day 14 of culture (n=6). (**H**) Percentage of cell death induced on patient PBMCs after 4-h incubation with Obinutuzumab only, or autologous BL-CIK cells in combination with isotype antibody (BL-CIK+Iso) or Obinutuzumab (BL-CIK+OBI) at an E: T 25:1 (n=6).

The combined therapy with CIK cells and OBI restrains the growth of an aggressive patient-derived lymphoma xenograft

The therapeutic efficacy of CIK+OBI combination therapy was evaluated *in vivo* in a mouse model of $CD20^+$ PDX established from the PBMCs of a patient affected by mantle cell lymphoma in an advanced leukemic phase (MCL3-PDX). The phenotypic similarity with the original tumor was confirmed by the analysis of CD20 expression by both IHC on FFPE tissue and flow cytometry on the dissociated tumor (Fig. 14, A-B). Seven days after the s.c. injection of tumor cells, mice were divided into four experimental groups (untreated, CIK+Iso, OBI only, CIK+OBI) and treated accordingly the scheduled therapy (Fig. 14, D) with CIK cells from a healthy donor that exerted a strong *in vitro* cytotoxicity against PDX-derived tumor cells (Fig. 14, C). Mice receiving the CIK+OBI combination therapy showed a remarkable delay in tumor growth and a significantly reduced tumor size when compared to mice treated with OBI alone (Fig. 14, F). Conversely, the CIK+Iso treatment produced only marginal effects, thus indicating that the synergy between the CD20-specific antibody and CIK cells is required to enhance the antitumor effect (Fig. 14, F). Indeed, only the CIK+OBI combined therapy significantly prolonged the survival of treated mice, while all other treatments were ineffective (Fig. 14, G).

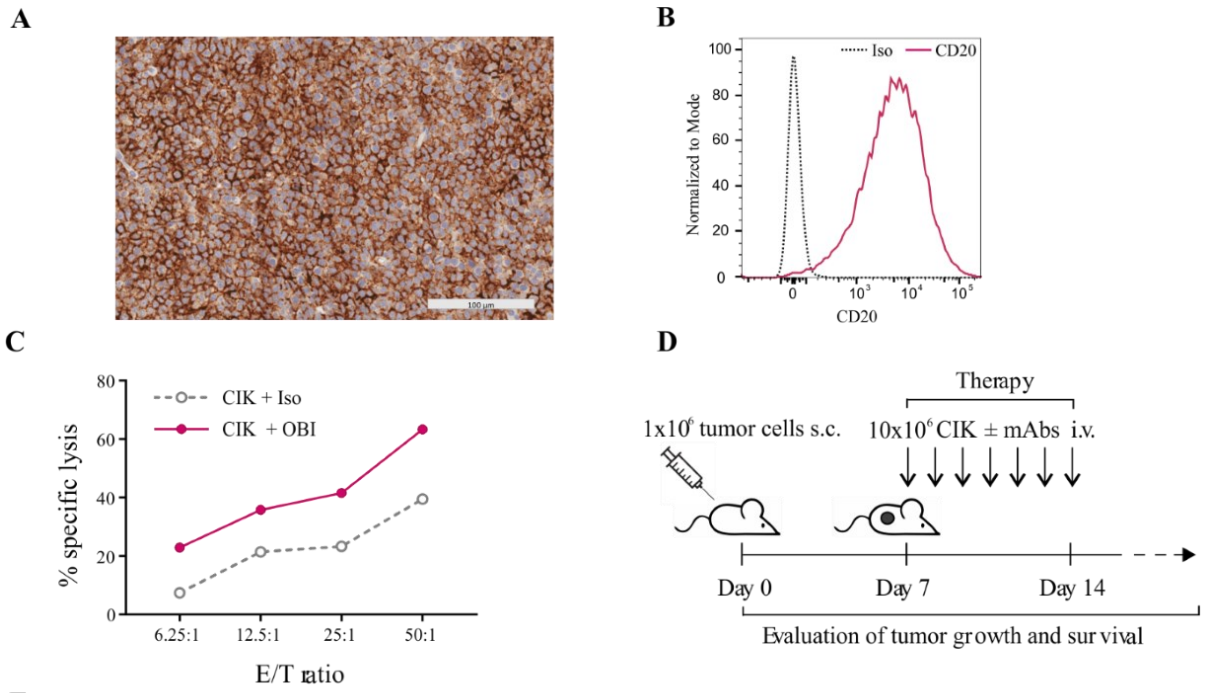
A
B
Iso
CD20
Normalized to Mode
CD20
C
CIK + Iso
CIK + OBI
% specific lysis
E/T ratio
6.25:1
12.5:1
25:1
50:1
D
Therapy
1x10^6 tumor cells s.c.
10x10^6 CIK ± mAbs i.v.
Day 0
Day 7
Day 14
Evaluation of tumor growth and survival

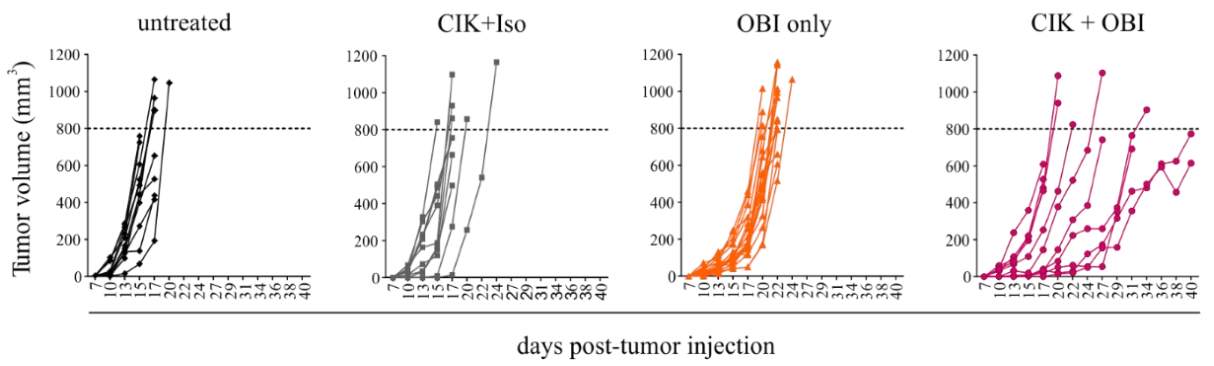
E
untreated
CIK+Iso
OBI only
CIK + OBI
Tumor volume (mm3)
days post-tumor injection

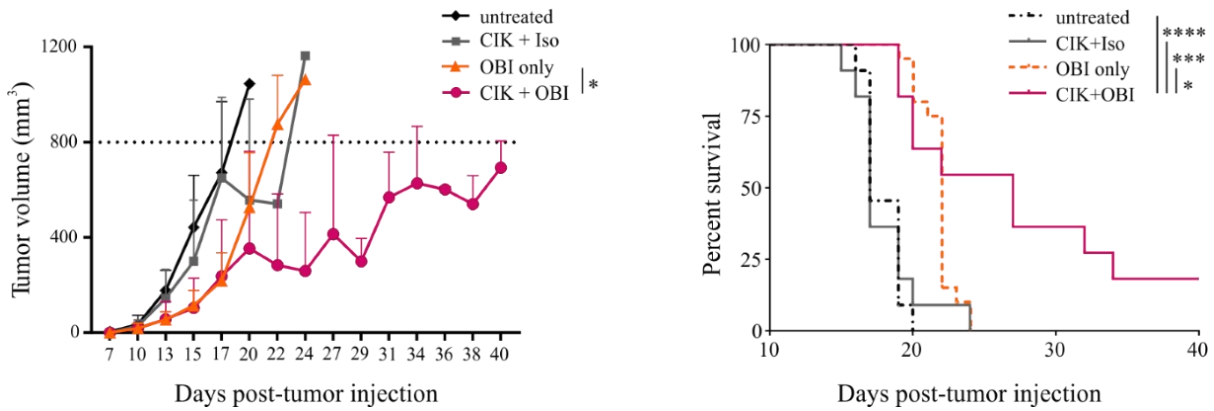
F
untreated
CIK + Iso
OBI only
CIK + OBI
*
Tumor volume (mm3)
Days post-tumor injection
G
untreated
CIK+Iso
OBI only
CIK+OBI
****
***
*
Percent survival
Days post-tumor injection

Figure 14. *In vivo* immunotherapy with CIK cells combined with OBI against an aggressive patient-derived lymphoma xenograft. (**A**) Representative image of anti-CD20 IHC staining *(brown)* of an established Mantle Cell Lymphoma (MCL1)-PDX. (**B**) Flow cytometry analysis of CD20 expression on tumor cells from a digested MCL1-PDX. (**C**) *In vitro* lytic activity of CIK cells used for *in vivo* therapy against target cells from a digested MCL1-PDX measured by a 4-h calcein-AM release assay. (**D**) Schematic representation of the *in vivo* therapeutic schedule. Seven days after subcutaneous (s.c.) injection of $1x10^6$ MCL1-PDX tumor cells, mice were either left untreated (n=11) or injected daily intravenous (i.v.) for 7 days with OBI only (n=12), or $1x10^7$ CIK cells in combination with an irrelevant antibody (CIK+Iso, n=11) or Obinutuzumab (CIK+OBI, n=11). (**E**) Tumor growth was monitored by caliper measurement at different time points and reported individually for each experimental group. (**F**) Time course of tumor growth presented as mean ± SD for each experimental group. Data were analyzed by Multiple t-test ($P<0.05$ =*). (**G**) Kaplan-Meyer survival curves of PDX-bearing mice. Statistical analysis was performed using the Log-rank (Mantel-Cox) test. (* $P<0.05$, *** $P<0.001$).

The co-administration of CIK cells with OBI results in a highly significant infiltration of adoptively transferred cells in the tumor mass, compared to the combinatory approach with a mAb control

Tissue sections from treated mice were stained with CD3/CD56/CD20/DAPI and analyzed by fmIHC (Fig. 15, A). Samples showed an enhanced immune infiltration when CIK cells were administered in combination with OBI, as compared with mice treated with CIK+Iso. In particular, mice receiving CIK+OBI showed a significantly higher density of both $CD3^+$ cells (31.91±48.87 cell counts/mm^2 in CIK+Iso vs 503±943.7 cell counts/mm^2 in CIK+OBI (Fig. 15, B); and $CD3^+CD56^+$ CIK cells (0.13±0.6 cell counts/mm^2 in CIK +Iso vs 28.51±52.85 cell counts/mm^2 in CIK+OBI (Fig. 15, B) within the tumor mass.

All these and more data have been very recently published in the *Journal for Immunotherapy of Cancer*[180].

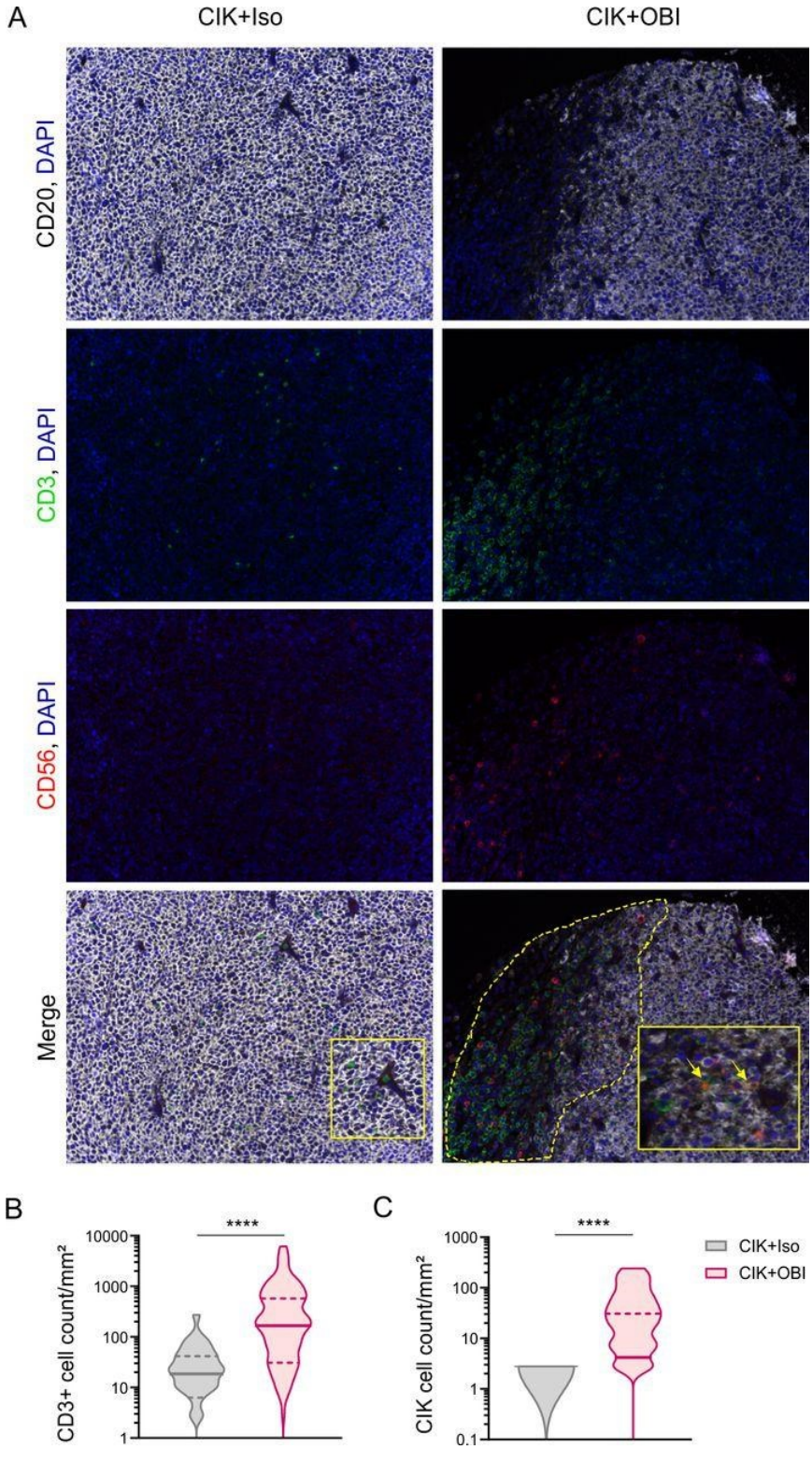

Figure 15. Quantification of tumor-infiltrating CD3$^+$ precursor and CIK cells by fmIHC. (**A**) Representative figure (x20) of FFPE tumor samples collected at the sacrifice of mice, stained with CD3 (green), CD56 (red), CD20 (white), and nuclei (blue), and analyzed by fmIHC. The yellow arrows indicate CD3+CD56+ cells. (**B**) Quantification (cell count/mm2) of tumor-infiltrating immune cells is presented as median and quartiles of CD3+ and (**C**) CD3+CD56+ subsets detected in an average of 80 different snaps

collected from each experimental group (****p<0.0001). CIK, cytokine-induced killer; FFPE, formalin-fixed and paraffin-embedded; fmIHC, fluorescent multiplex immunohistochemistry; OBI, obinutuzumab.

3.3 Objective III

Combinatory therapy with CIK cells and the mAb TRS or the bsscFv Her2xCD3 in a BiTE-like format for Her2/neu$^+$ breast cancer

The bsscFv Her2xCD3 binds selectively on CD3$^+$ effector and Her-2- expressing target cell lines

To address the combinatorial therapeutic strategy for Her-2/neu$^+$ breast cancer, we explored the feasibility of the synergistic effect between CIK cell cytotoxicity and the clinical-grade mAb TRS or scalar doses of the bsscFv Her2xCD3. The bsscFv Her2xCD3 in a BiTE-like format was a gift from Matthias Peipp[150]. The molecule is a result of the fusion between the CD3-directed scFv-fragment that is C-terminally linked to the Her-2-specific scFv; its design in a BiTE-like format can trigger the full activation of T cells aside from other co-stimuli[143,150].

Firstly, we selected five different human cell lines – HCC1419, T-47D, HCC1569, SK-BR-3, MCF-7 – known in the literature to express the surface antigen Her-2, whereas the triple-negative breast cancer (TNBC) MDA-MB-468 cell line was chosen as the negative control. Dot plot and histogram from flow cytometry analysis shown in figure 16, confirmed that all the tested tumor cell lines highly expressed Her-2 antigen (83±100%).

We next evaluated the binding property of the bsscFv Her2xCD3 on both CIK cells and Her-2$^+$ cell lines. CIK cells harvested on day 14 for the following functional assays were previously screened for the expression of CD3, CD56, NKG2D, and CD16a antigens by flow cytometry. After 1 hour of co-incubation, the Cy5.5 fluorophore-conjugated Her2xCD3 bound to CIK cells in a dose-dependent manner (0.02±1 µg/mL) (Fig. 16, b) and to cancer cell lines even at very low dose-range (0.1 µg/mL) (Fig. 16, c).

Then, we demonstrated the simultaneous bispecific binding of Her2xCD3 on both effector CIK and tumor cells. CIK and HCC1419 or SKBR3 tumor cells respectively labelled with CellTrace CFSE and CellTrace Violet, were co-cultured with different doses of Her2xCD3 (0.1-5 µg/mL) for 30 minutes. We observed that, at the highest tested dose, the bsscFv Her2xCD3 engaged 16±18,3% of the double positive CellTrace Violet$^+$ and CellTrace CFSE $^+$ cell population, compared to the 4,66±8,76% double positive population gated at the lowest dose (Fig. 16, d).

a.

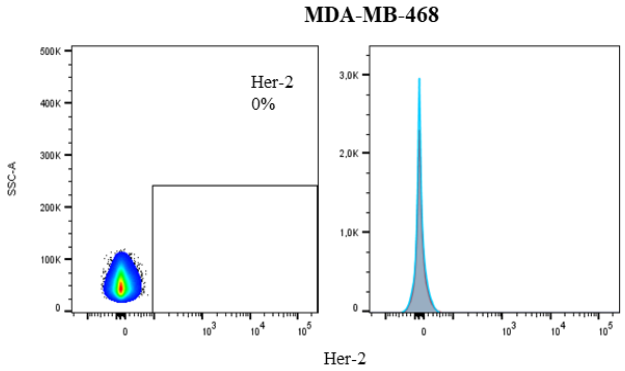
MDA-MB-468
Her-2
0%
SSC-A
Her-2

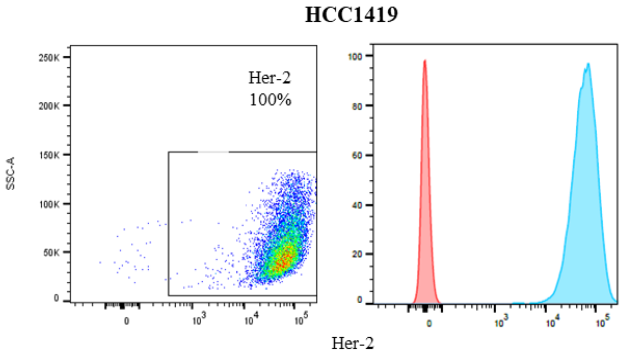
HCC1419
Her-2
100%
SSC-A
Her-2

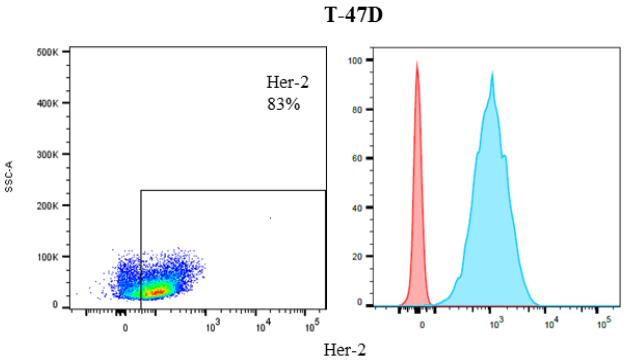
T-47D
Her-2
83%
SSC-A
Her-2

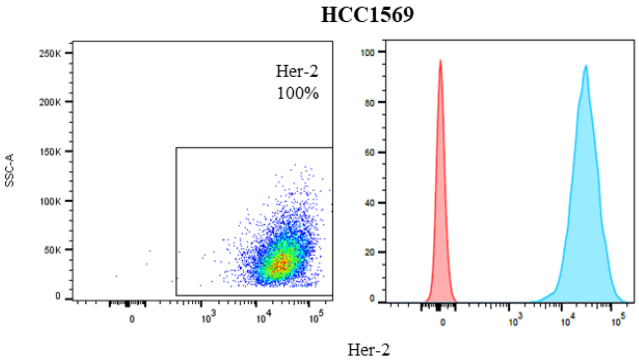
HCC1569
Her-2
100%
SSC-A
Her-2

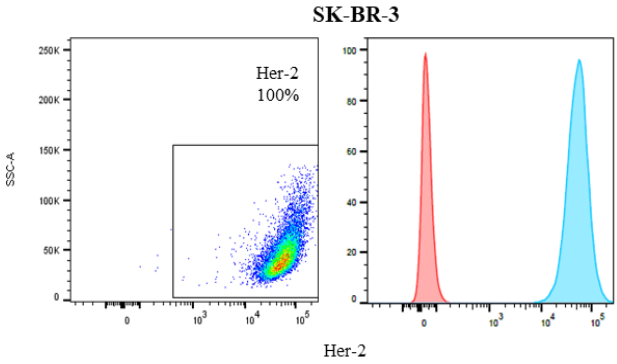
SK-BR-3
Her-2
100%
SSC-A
Her-2

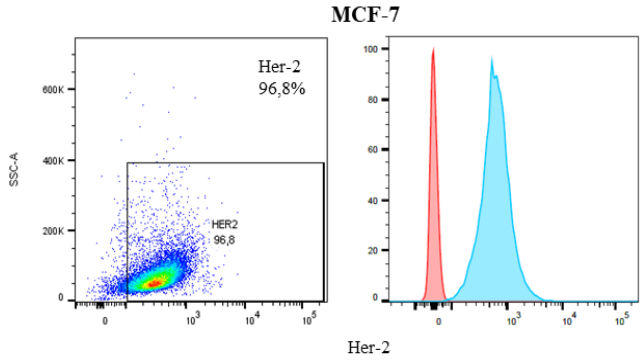
MCF-7
Her-2
96,8%
HER2
96,8
SSC-A
Her-2

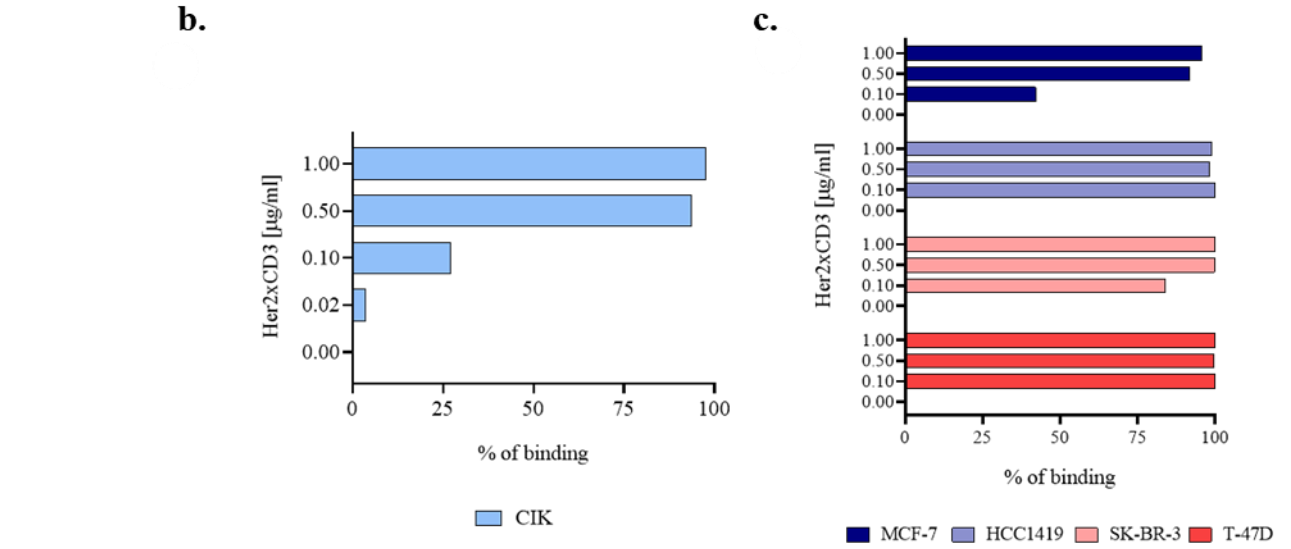
b.
Her2xCD3 [µg/ml]
1.00
0.50
0.10
0.02
0.00
0
25
50
75
100
% of binding
CIK
c.
Her2xCD3 [µg/ml]
1.00
0.50
0.10
0.00
% of binding
MCF-7
HCC1419
SK-BR-3
T-47D

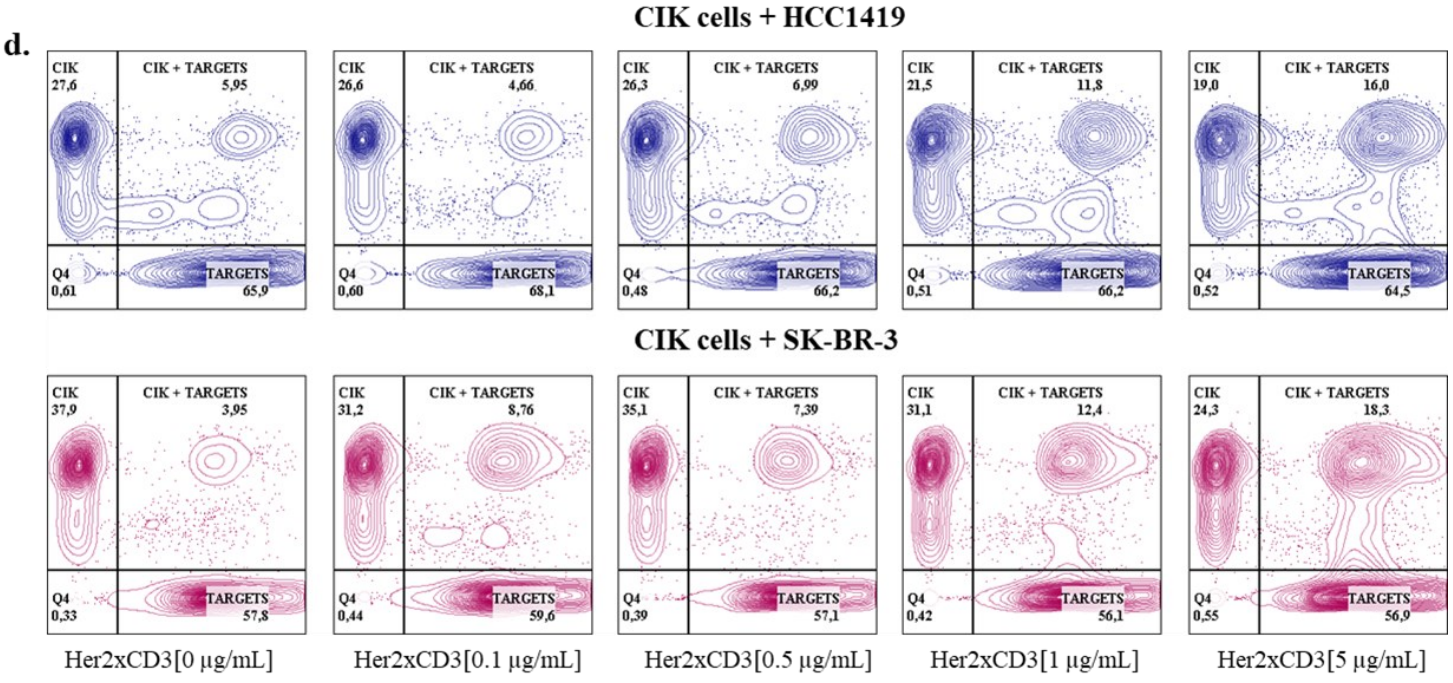
d.
CIK cells + HCC1419
CIK
CIK + TARGETS
TARGETS
Q4
27,6
5,95
0,61
65,9
26,6
4,66
0,60
68,1
26,3
6,99
0,48
66,2
21,5
11,8
0,51
66,2
19,0
16,0
0,52
64,5
CIK cells + SK-BR-3
37,9
3,95
0,33
57,8
31,2
8,76
0,44
59,6
35,1
7,39
0,39
57,1
31,1
12,4
0,42
56,1
24,3
18,3
0,55
56,9
Her2xCD3[0 µg/mL]
Her2xCD3[0.1 µg/mL]
Her2xCD3[0.5 µg/mL]
Her2xCD3[1 µg/mL]
Her2xCD3[5 µg/mL]

Figure 16. Her-2 antigen expression on breast cancer cell lines and evaluation of bsscFv Her2xCD3 binding property (a-d). a) Extracellular expression of Her-2 antigen on human breast cancer cell lines. The expression of Her-2 was assessed by flow cytometry; MDA-MB-468 Her-2$^-$ cell line was used as a negative control. Dot plot and histogram of Her-2 expression are shown for each tested cell line. **b-c) The bsscFv Her2xCD3 selectively binds on CD3$^+$ effector CIK cells and Her-2$^+$ tumor cell lines.** CIK and target cells were incubated independently for 30 minutes with different doses of Cy5.5-fluorophore-conjugated Her2xCD3, and data were analyzed by flow cytometry (n=3). **d) The bsscFv Her2xCD3 simultaneously engages both CD3$^+$ and Her-2$^+$ cells.** Labeled CIK cells and SK-BR-3 or HCC1419 cancer cells were co-cultured with increasing doses of Her2xCD3 for 30 minutes on ice. The co-binding between CIK and target cells mediated by Her2xCD3 was quantified by gating the double-positive CellTrace CFSE-CellTrace Violet cell population by flow cytometry.

The mAb TRS and the bsscFv Her2xCD3 successfully enhanced CIK cell-killing activity against several Her-2-expressing breast cancer cell lines *in vitro.*

We investigated whether the combination of CIK cells with TRS and the bsscFv Her2xCD3 (Her2xCD3-CIK cells) enhanced their basal anti-tumor activity against Her-2$^+$ cancer cell lines in a 4-hour Calcein-AM-release assay. The combination of CIK cells with Her2xCD3 achieved a significant improvement of the antigen-specific CIK cells cytotoxicity against all tested Her-2-expressing cancer cell lines already at low E/T ratios (6.25:1±12.5:1 for HCC1569, MCF-7, SK-BR-3, and T-47D) compared to the basal lytic activity of both CIK cells (CIK only) and to the bsAb isotype control (CIK+Iso) (Fig. 17). Notably, both the HCC1419 and HCC1569 TRS-resistant tumor cell lines[181,182] showed to be sensitive to Her2xCD3-CIK cell lytic effect (Fig. 17, Upper line). We observed that the combination of CIK cells plus TRS was less efficient in terms of tumor cell killing in a 4-hour assay, compared to the lytic effect of CIK cells with the bsscFv Her2xCD3. However, the combination of CIK cells with TRS was significant against the SK-BR-3 target cell line (Fig. 17, 50:1 E/T), compared to the basal killing of CIK cells, whereas the 40% of specific lysis of the HCC1569 cell line was achieved when TRS was combined with the CIK cells (Fig. 17, Upper line, 50:1 E/T), by asserting the advantage of the combinatory therapy. The Her-2-negative breast cancer cell line MDA-MB-468 was used as a negative control.

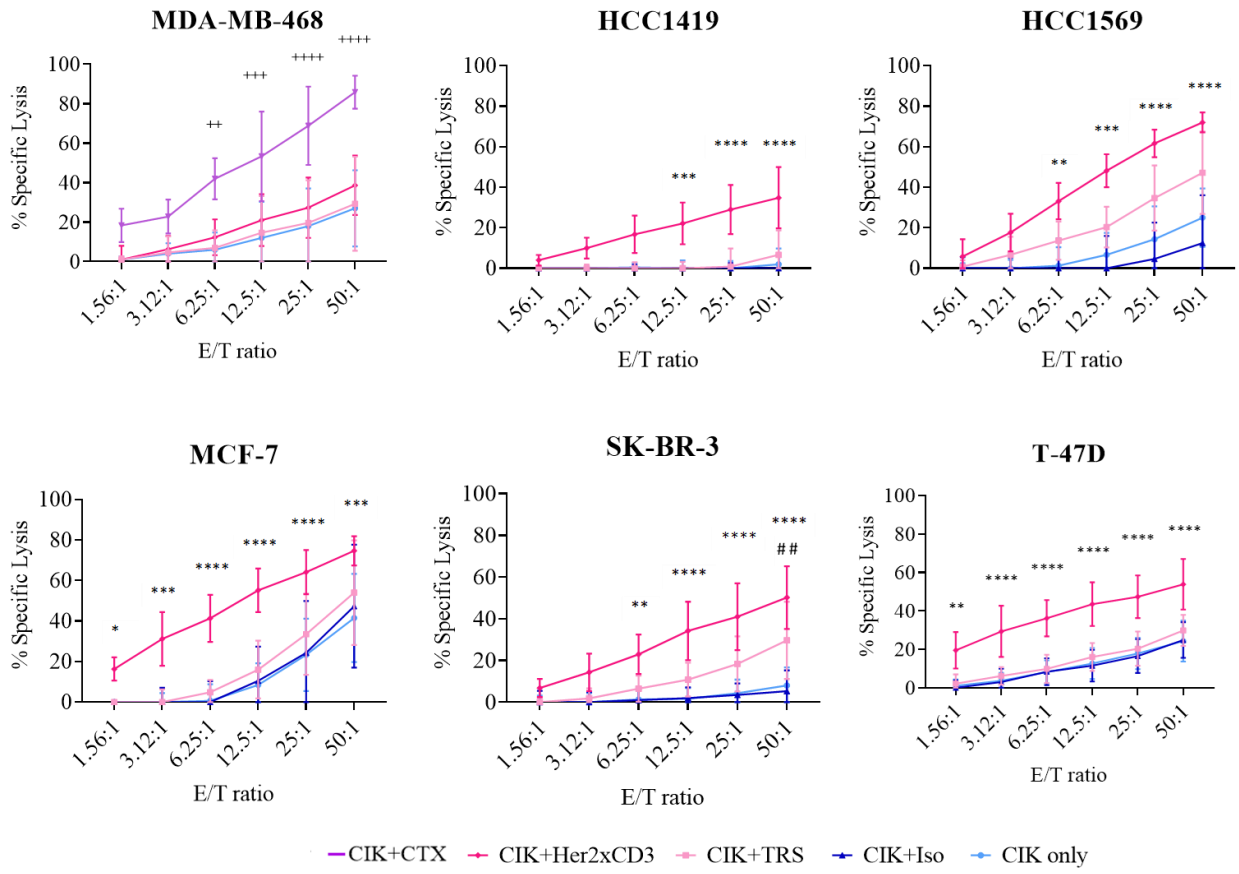

Figure 17. Evaluation of CIK cells killing activity with a 4-hour calcein-AM-release assay. CIK cells were challenged against Her-2-expressing breast cancer cell lines, whereas the Her-2$^-$ - MDA-MB-468 tumor cell line was tested as a negative control. Lytic activity was assessed by calcein-AM release assay on day 14 of CIK cell culture period (n=6). Results show mean values ± SD of the specific lysis at different E:T ratios. Statistical analysis was performed by 2-way ANOVA test with Bonferroni's correction. (Comparison between CIK+Her2xCD3 and CIK cells only: ****, $P \leq 0.0001$;***, $P \leq 0.001$; **, $P \leq 0.01$; *, $P \leq 0.05$; comparison between CIK+TRS and CIK cells only: ##, $P \leq 0.01$; for MDA-MB-468 only, comparison between CIK+CTX and CIK only: ++, $P = 0.0036$, +++, $P= 0.006$, ++++, $P<0.0001$.)

As in literature it has been reported that bsAbs engaging T cells through CD3 show better-measured long-term cytotoxicity outcomes[183], we complemented the 4-hour calcein-AM-release assay results about the CIK cell killing activity with an impedance analysis of adherent target cells in real-time, by monitoring cellular events on the extended time course. The Real-Time Cell Analysis (RTCA) allows for determining whether a smaller number of effector cells is enough to completely lyse adherent tumor cells, or conversely if tumor cells can proliferate because of incomplete lysis due to an inefficient anti-tumoral activity of effector cells. We observed that CIK cells combined with Her2xCD3 showed a rapidly remarkable killing activity against the MCF-7 cell line at 10:1 ratio after

a 2-hour co-culture (Fig. 18, a-b), reaching the maximum of their lytic effect after 10-hour co-culture up to 40-hour from onset (Fig. 18, a-b). Nevertheless, the RTCA sensibility was evident when we challenged a really small number of CIK cells against MCF-7 tumor cells, highlighting the efficacy of this combinatory approach even at an extremely low E:T ratio (1:1, 0.5:1 ratio) as shown in the plots c and d in figure 18. Indeed, 10 hours later, the percentage of Her2xCD3-CIK cells mediated lysis accounted 20±40% at both 1:1 and 0.5:1 ratios, greatly increasing up to 80±90% after 20 hours total of co-culture (Fig. 18, c-d).

Even though clinical-grade bispecific antibodies offer more advantages in terms of cytotoxic effect compared to mAbs, some issues such as the high production cost and the risk of CRS persist[145]. In this regard, we aimed to assess the anti-tumor effect of CIK cells combined with Her2xCD3 reducing the functional concentration of Her2xCD3. The synergistic efficacy of Her2xCD3-CIK cells against different Her-2^{+} tumor cell lines (10:1 ratio) was confirmed also a very low dose of Her2xCD3 (concentration $\log 10^{-3} \pm 10^{0}$), notwithstanding the killing activity of CIK cells was directly correlated with the dose of the bsscFv Her2xCD3 (Fig. 19).

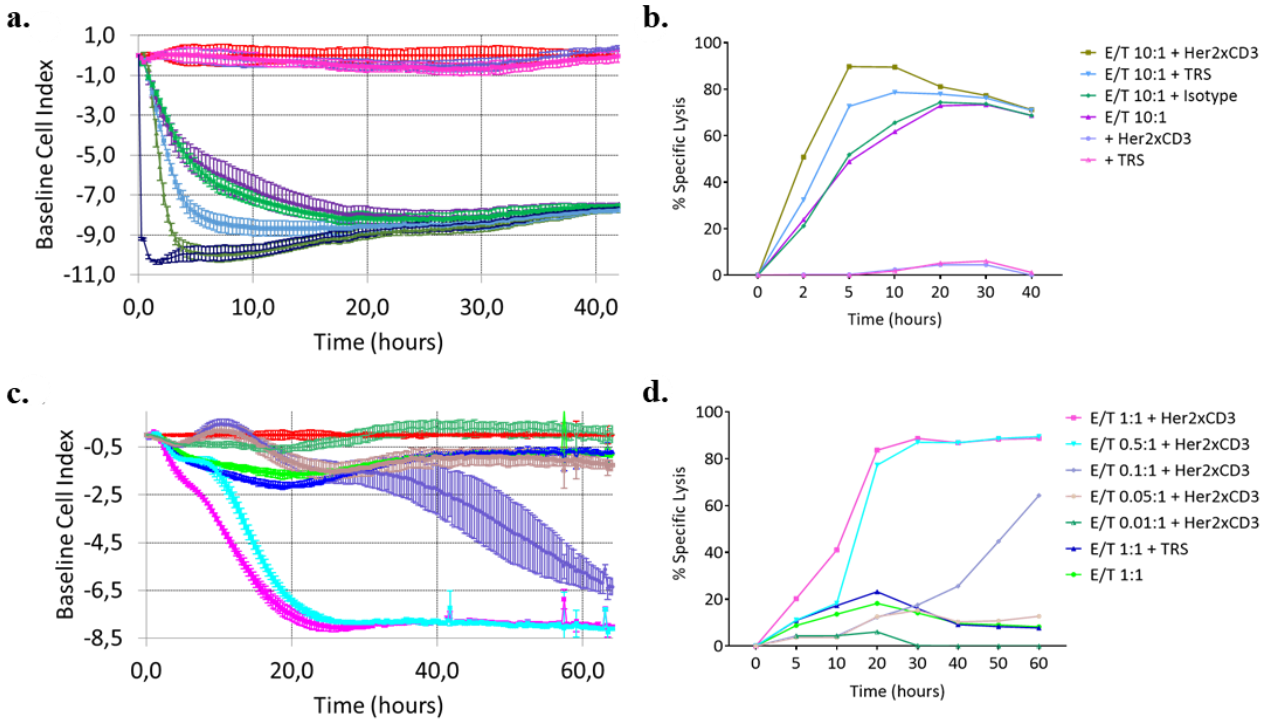

Figure 18. Assessment of CIK cells cytotoxicity with a long-term Real-Time Cell Analysis (RTCA) assay. MCF-7 target cells were cultured for approximately 20 hours on an E-plate before the addition of CIK cells and tested antibodies. The adherent cells impedance indicated as baseline cell index, was determined every 20 minutes over the experimental course and normalized to 1 at the time point 0, following the addition of both CIK cells and antibodies. The purple (Figure a-b) and green light lines (Figure c-d) represent the MCF-7 cells lysis induced by CIK cells alone without the addition of any antibody, whereas the violet light and the pink lines (Figure a-b) represent the tumor cells lysis induced by the presence of the antibodies alone. The red line in plots a-c represents the basal adhesion of MCF-7 cell lines, whereas the blu line in the plot a represents the maximum lysis induced by TritonX. The graph shows the average of triplicates with the SD. Figure b and figure d represent the conversion of the baseline Cell Index in the percentage of specific lysis.

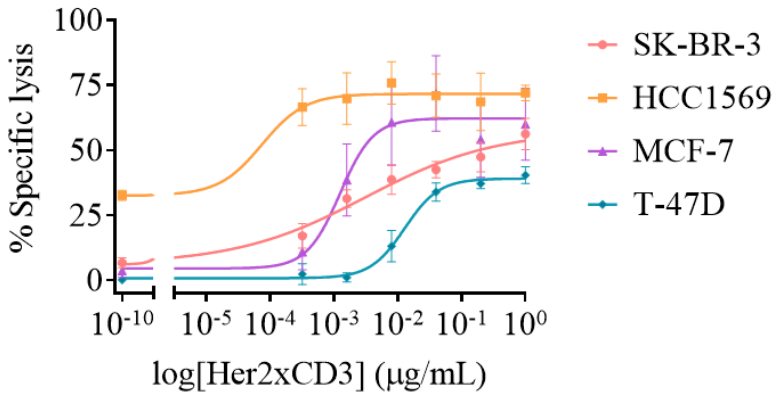

Figure 19. The synergistic effect of the combination between Her2xCD3 and CIK cells was confirmed even at low dose-concentration of Her2xCD3. The percentage of specific lysis was measured by a Calcein-AM release assay; CIK cells and SK-BR-3, HCC1519, MCF-7, T-47D target cells,10:1 ratio, were co-cultured with scalar doses (1, 0.2, 0.04, 0.008 µg/mL) of Her2xCD3 for 4 hours.

CIK cells combined with the bsscFv Her2xCD3 retain a safe cytokine profile

Then we evaluated the inflammatory profile of CIK cells, alone or with the tested antibodies, in response to the MCF-7 target cell line. We also addressed the question of whether the presence of the bsscFv Her2xCD3 or TRS could negatively impact CIK cell safety in terms of cytokine release; mainly because the CRS often occurs after the infusion of several antibody-based therapies[184]. Upon 20-hour co-culture with Her2xCD3-CIK cells and MCF-7 cancer cells (10:1 ratio), we quantified by flow-cytometry the concentrations of the following secreted cytokines: GM-CSF, IFN-α, IFN-γ, IL-2, IL-4, IL-5, IL-6, IL-9, IL-10, IL-12, IL-17A and TNF-α in the cell culture supernatant. We detected an increase in the concentration (pg/mL), of IFN-, GM-CSF, TNF- α pro-inflammatory cytokines,

which was strictly correlated with the bsscFv Her2xCD3 dosage (Fig. 20, 1st-4th line). Furthermore, the concentration of released IL-2 was constant among the tested conditions and we did not detect the production of IL-12 and IL-17a pro-inflammatory cytokines, much less of IL-4, IL-9, and IL-10 anti-inflammatory cytokines. Importantly, CIK cells seemed to retain a safe cytokine profile despite the sudden rise in T cell activation mediated by both Her2xCD3 and TRS as demonstrated by the increase in tumor cells lysis in (Fig. 18, A-D), compared to the action of both the engineered antibodies on their own. In this regard, we observed that the pleiotropic cytokines IL-6 and IL-5 mainly associated with the CRS[184,185] were secreted at very low concentrations (pg/mL) after co-culture of Her2xCD3-CIK cells with target cells (Fig. 20, 2nd-3rd line).

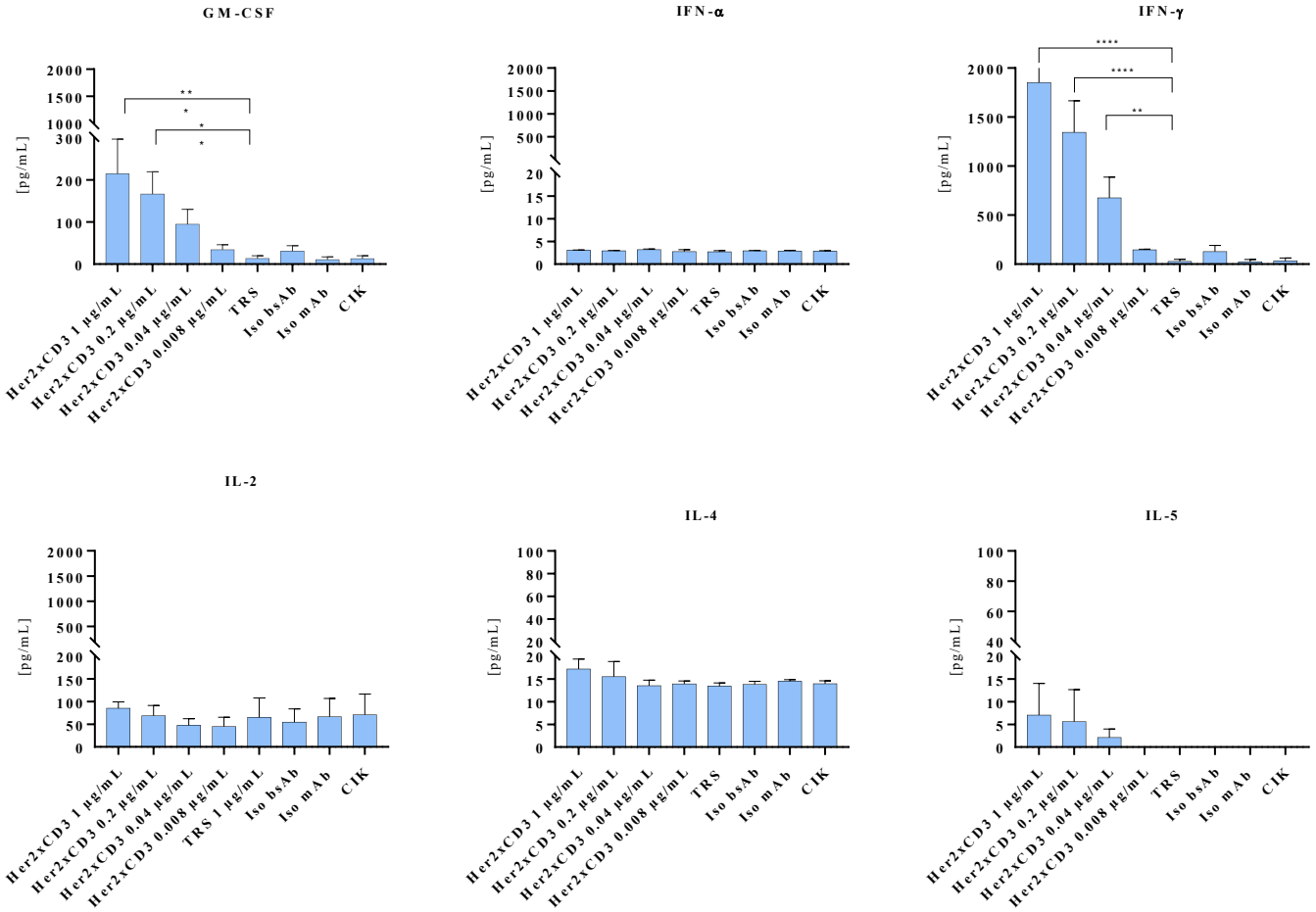

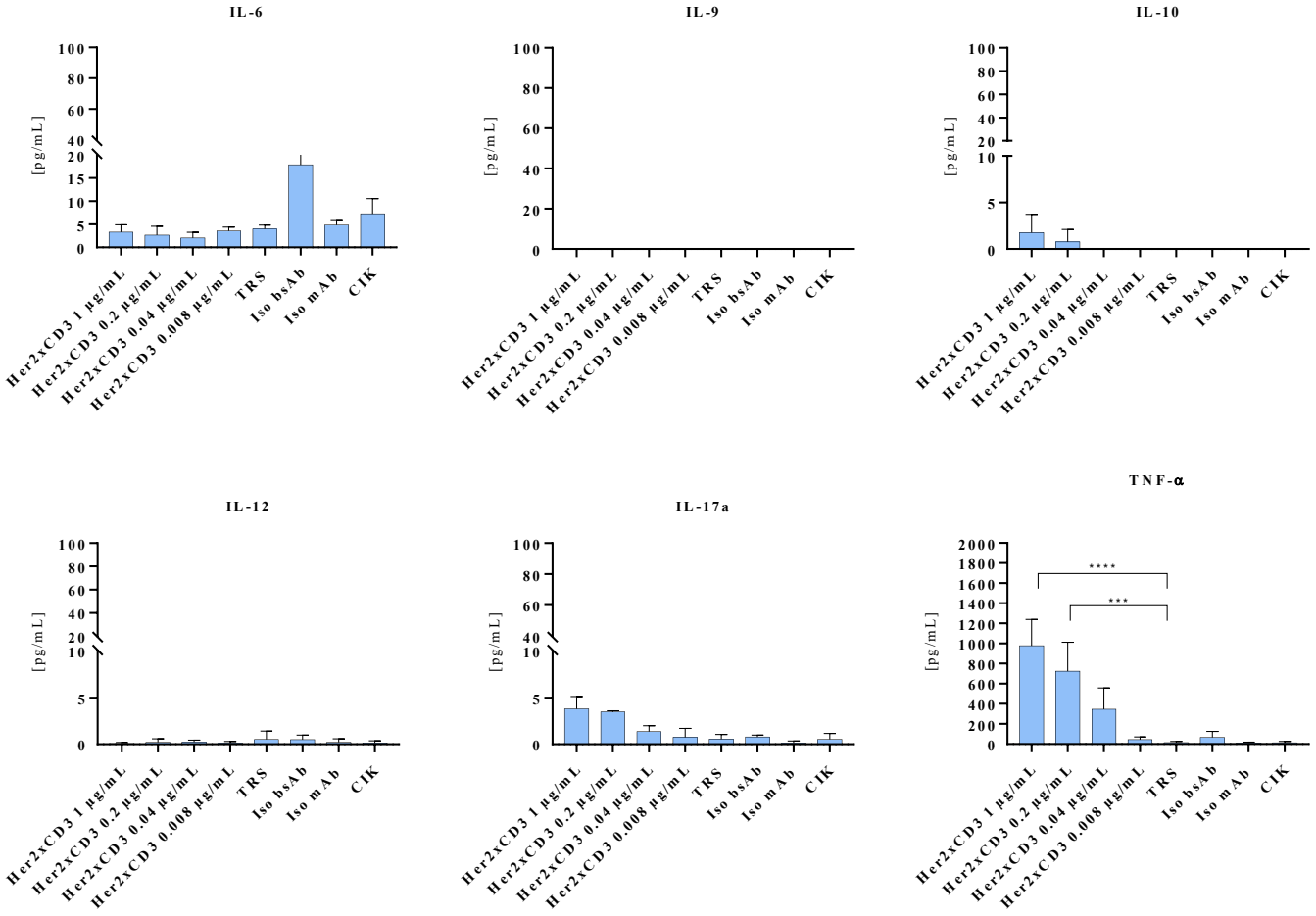

Figure 20. The combination of CIK cells with the bsscFv Her2xCD3 does not impact negatively the safety of CIK cells. Secreted GM-CSF, IFN-α, IFN-γ, IL-2, IL-4, IL-5, IL-6, IL-9, IL-10, IL-12p70, IL-17A, and TNF-α were quantified in the 20-hour co-culture supernatant between CIK and MCF-7 cells (10:1 ratio) with MACSPlex Cytokine 12 Kit, human (Miltenyi Biotec, Germany) according to the manual instructions. Statistical analysis was carried out by comparing all the tested concentrations of Her2xCD3 with the TRS (Mean±SD n=3; ****, $P \leq 0.0001$;***, $P \leq 0.001$; **, $P \leq 0.01$).

In vivo biodistribution of Her2xCD3 and MCF-7/Luc xenograft breast cancer mouse model

To assess successively the *in vivo* efficacy of the proposal combinate therapy Her2xCD3-CIK cells, we evaluated firstly the *in vivo* biodistribution of the bsscFv Her2xCD3 in a NOD/SCID common γ chain knockout (NSG) mouse model. Cy5.5 fluorophore-conjugated Her2xCD3 injected intraperitoneally in MCF-7 xenograft mice reached efficiently the tumor site, picking the maximum concentration ($8x10^5$ph/sec) after 8 hours post-injection (Fig 21).

Next, we establish a metastatic MCF-7/Luc-bearing mouse model to refine the scheduled therapy.

These data have been shown in a poster format at *ESMO*, *ITOC, and NIBIT* congress, which took place respectively in Berlin, Munich, and Padua in 2022.

3.4 Objective IV

The tumor microenvironment of a breast-cancer mouse model

To further gain insight into the trafficking and the infiltration of transferred cells *in vivo* in the BC mouse models developed in our laboratory, we established a collaboration with the laboratory of Doctor Emmanuel Donnadieu at the Cochin Institute in Paris since they recently developed an *ex vivo* slice assay[175,186] which perfectly mimics an adoptive cell transfer experiment. In the slice assay, fluorescently labelled T effector cells are placed *ex vivo* in a fresh agarose-embedded thick-tissue slice and imaged in real-time with a high-resolution spinning disk confocal microscope equipped with a temperature-controlled chamber and a perfusion system [175,186]. Overall, this technique results be easily customizable for the study of both transferred and resident cells, in real-time or *in situ*, and in fresh or fixed tissue slices (Fig. 6). The research team with whom I have worked focuses on the cooperation between the innate and adaptive immune system during the regression of a transplanted polyoma middle T antigen (Tp-PyMT) mammary tumor model, after treatment with the 5,6-dimethylxanthenone-4-acetic acid (DMXAA), a stimulator of interferon genes (STING) agonist[187,188]. As the cellular balance occurring between macrophages, monocytes, and $CD8^+$ T cells seems to play a pivotal role during the tumor regression phase, they are currently exploring the spatial interactions taking place in the tumor niche looking for insights into whether this favourable cellular crosstalk can be retained [189]. As well, their purpose is to investigate the three-dimensional structure of the TME, renowned for negatively influencing breast cancer progression and clinical outcomes[190,191]. To learn more about imaging techniques and practice for optimal microscopy utilization, I was trained on their ongoing projects looking for suitable immune markers to stain and identify cell populations in tumor samples. Such cellular interactions were imaged *in situ* by the tumor slice imaging technique[192] combined with high-resolution spinning disk laser confocal microscopy (SDCLM), and the tumor structure, mainly in terms of the stiffness of extracellular matrix (ECM) collagen, was investigated by the Second Harmonic Generation (SHG) microscopy.

Study of *in situ* spatial cellular interactions by using tumor slice imaging

Agarose-embedded slices from PLP-fixed Tp-PyMT-tumor samples were obtained with a vibratome and a thickness of 350 μm was set to preserve entirely the three-dimensional structure of the tissue. Tumor slices were stained with different combinations of fluorophore-conjugated antibodies looking for the potential cellular interactions occurring between T cells and macrophages/monocytes, and their spatial distribution within stroma and tumor islets. For each staining panel, the marker combination was evaluated for at least four antigens. The tumor slice in figure 22 was stained for

CD8, CD4, F480, and EpCam, representing the spatial localization of F480-polarized macrophages, $CD8^+$, and $CD4^+$ T cells in EpCam-expressing tumors. Tumor slices in figure 22 were stained for CD8, CD103, F480, and EpCam (Fig. 23, a), and for CD8, Fibronectin, F480, and EpCam (Fig. 23, b) showing, respectively, the spatial distribution of $F480^+$ macrophages, $CD103^+$ DCs, and $CD8^+$ T cells in $EpCam^+$ tumor (Fig. 23, a), and the spatial distribution of $F480^+$ macrophages and $CD8^+$ T cells within the fibronectin-labelled stroma and $EpCam^+$ tumor islets (Fig. 23, b). Furthermore, to check the expression of the immune-checkpoint PD-1 on both $F480^+$ macrophages and $CD8^+$ T cells in a border section of a Tp-PyMT tumor, tumor slices were stained for CD8, F480, gp38, and PD-1 (Fig. 24, a). Whereas the spatial distribution of $CD11b^+$ macrophages, $CCR2^+$ monocytes, and $CD8^+$ T cells within $EpCam^+$ tumor islets was evaluated by staining tumor samples for CD8, CD11b, CCR2, and EpCam (Fig. 24, b). Imaging of such thick-tumor slices was carried out in the IMAG'IC facility at the Cochin Institute by using an inverted spinning disk confocal laser microscope, thoroughly described in the Material and method session. Samples were imaged at 20x or 60x magnification and acquired along the z-axis, to collect entirely the three-dimensional structure of the tick tissue. Z-stacked images were then analyzed in a two-dimensional visualization, by compressing the z information into a single plane with the maximum intensity Z projection performed with ImageJ software. Indeed, spinning disk confocal laser microscopy (SDCLM) lets the optical sectioning of 3D samples in 2D slices, ensuring high-resolution and high-efficiency imaging, as emphasized by the high-quality image acquired at 60x magnification in figure 23, b. Overall, among the several reasons better argued in the discussion, SDCLM presents many advantages over both conventional widefield optical microscopy and confocal laser scanning microscopy (CLSM), not only concerning real-time live imaging.

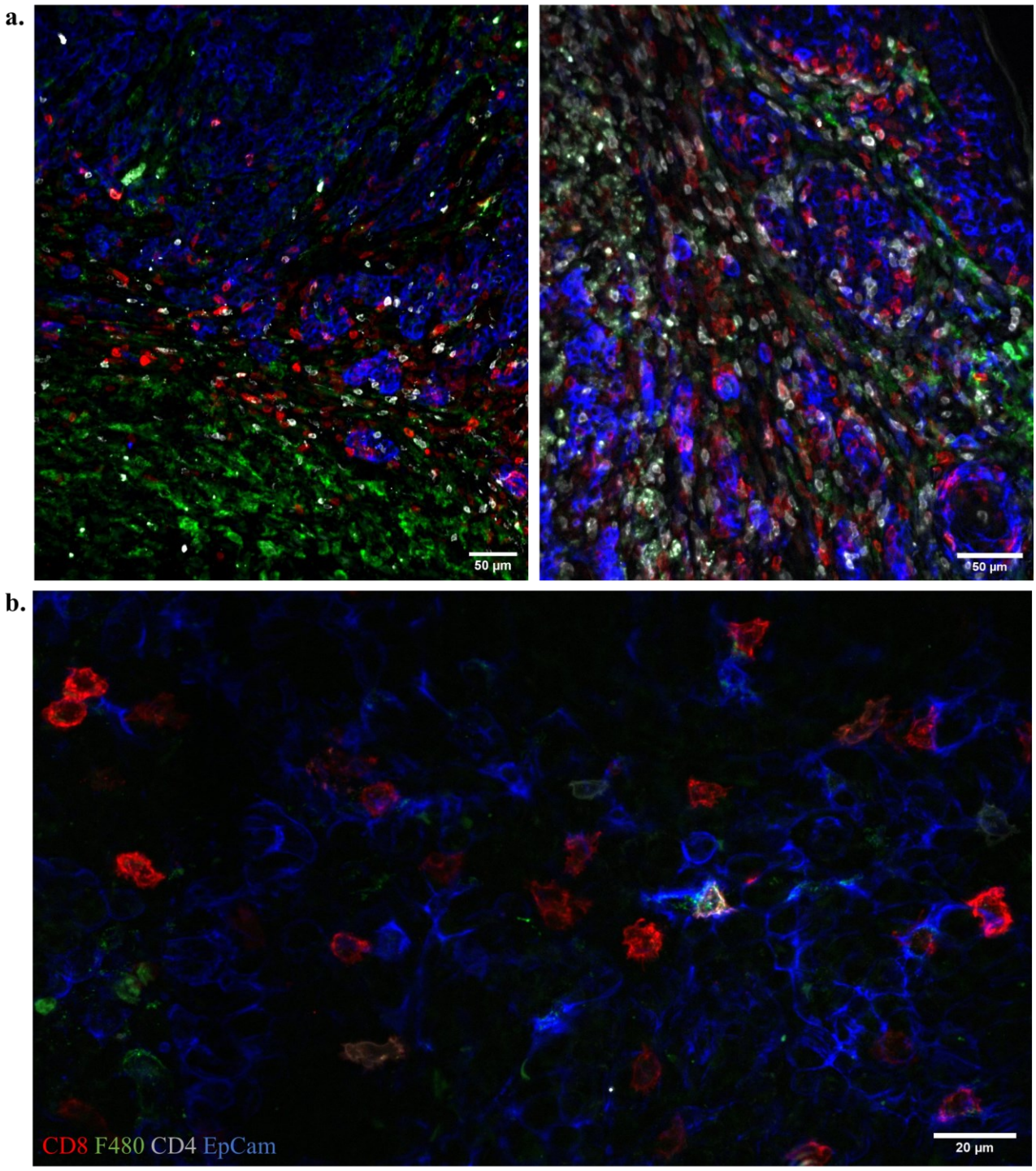

Figure 22. Spatial distribution of F480-expressing macrophages, CD8$^+$ and CD4$^+$ T cells in EpCam$^+$ tumor slices of a Tp-PyMT mouse model. Representative snaps of fixed Tp-PyMT tumor samples stained for CD8 (red), CD4 (white), F480 (green), EpCam (blue). Samples were imaged with IXplore spin microscope, a) 20x magnification, b) 60x magnification. Scale bar, 200 µm. Maximum intensity Z projection visualization.

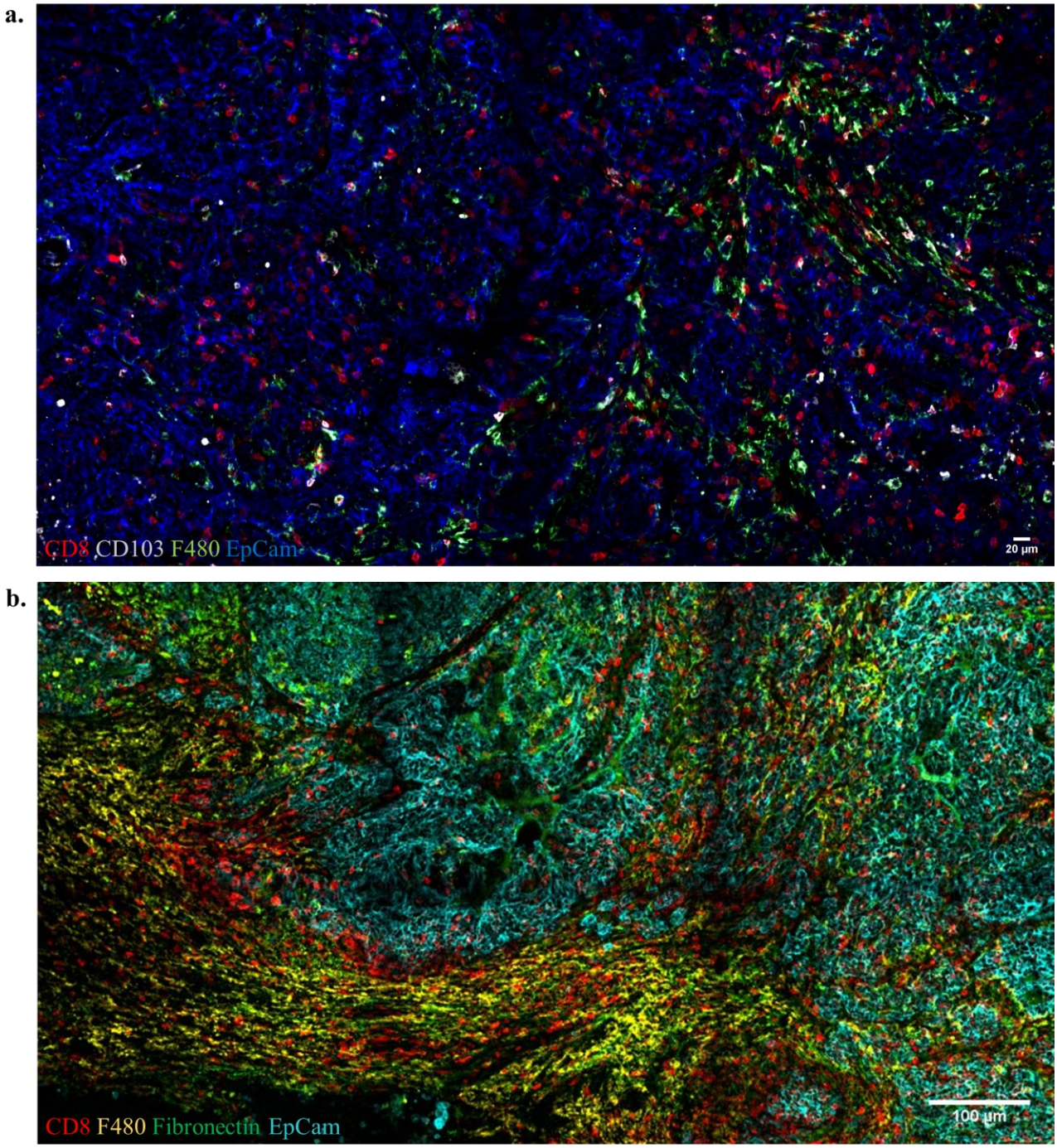

Figure 23. a) Spatial distribution of F480-expressing macrophages, CD103$^+$ DCs, and CD8$^+$ T cells in EpCam$^+$ tumor of a Tp-PyMT mouse model. Representative snaps of fixed Tp-PyMT tumor samples stained for CD8 (red), CD103 (white), F480 (green), EpCam (blue). Samples were imaged with IXplore spin microscope, 20x magnification, Scale bar, 20 µm. **b) Spatial distribution of F480-expressing macrophages and CD8$^+$ T cells within stroma and tumor islets of a Tp-PyMT mouse model.** Representative snaps of fixed Tp-PyMT tumor samples stained for CD8 (red), Fibronectin (green), F480 (yellow), EpCam (cyan). Samples were imaged with IXplore spin microscope, 20x magnification, Scale bar, 100 µm. Maximum intensity Z projection visualization.

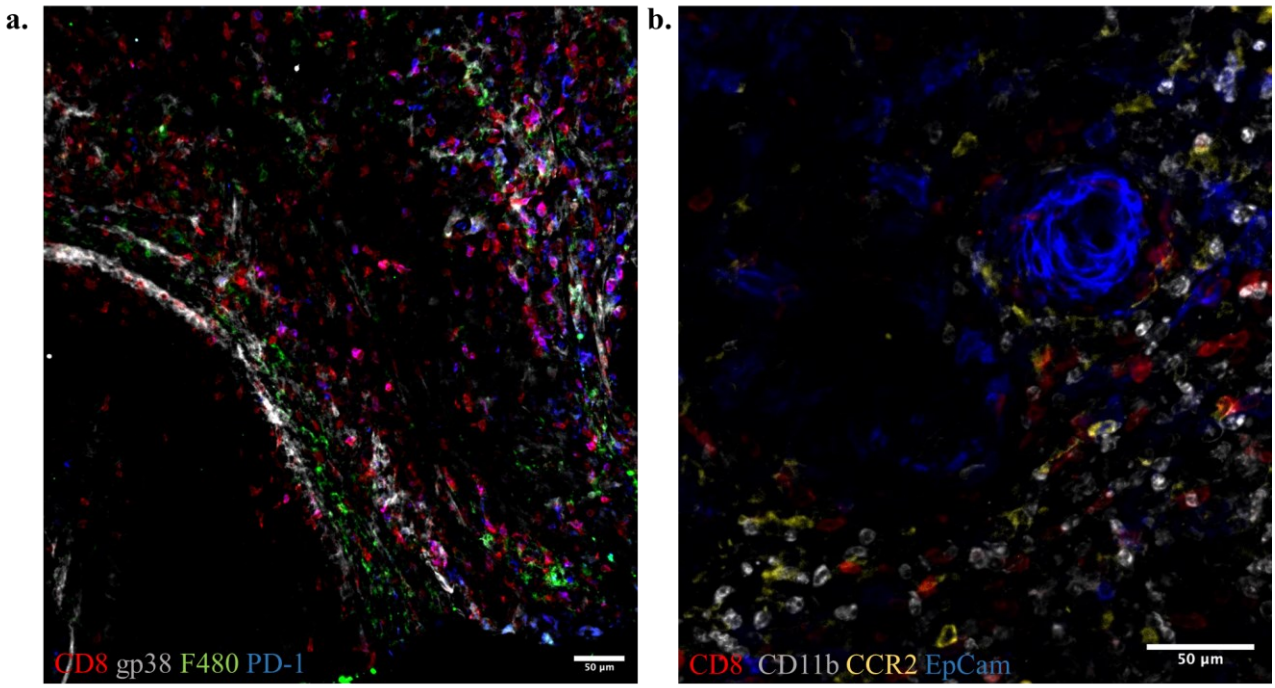

Figure 24. a) PD-1 expression in F480-expressing macrophages and CD8$^+$ T cells in a border section of a Tp-PyMT mouse model. Representative snaps of fixed Tp-PyMT tumor samples stained for CD8 (red), F480 (green), gp38 (white), PD-1 (blue). Samples were imaged with IXplore spin microscope, 20x magnification, Scale bar, 50 µm. **b) Spatial distribution of CD11b$^+$ macrophages, CCR2$^+$ monocytes, and CD8$^+$ T cells within EpCam$^+$ tumor islets of a Tp-PyMT mouse model.** Representative snaps of fixed Tp-PyMT tumor samples stained for CD8 (red), CD11b (white), CCR2 (yellow), EpCam (cyan). Samples were imaged with IXplore spin microscope, 20x magnification, Scale bar, 50 µm. Maximum intensity Z projection visualization.

Characterization of stiffness of extracellular matrix (ECM) collagen by Second Harmonic Generation (SHG) microscopy

Considering the pivotal role played by the tumor ECM in breast tumors and the association between higher deposition of collagen and worse prognosis[172,173,193], we took advantage of the second harmonic generation (SHG) microscopy to investigate the ECM collagen stiffness and density in 4T1-breast cancer mouse model. Fibrillar collagen can produce an intrinsic optical signal literally called a second-harmonic generation. This nonlinear optical process occurs when two photons scatter off a noncentrosymmetric material - such as a collagen fibre- producing a single photon with exactly twice the energy of the initial photons[177] (Fig.8). For each mouse, 15 µm-tick FFPE tissue slides representative of three different tumor sections were analyzed to reconstruct tissue heterogeneity (Fig. 25). Samples were imaged with a 2-photon Leica SP8 DIVE FLIM microscope with a 25x immersion objective. Figure 25 shows four representative snaps of the collagen fibre organization in the tumor mass of a 4T1breast cancer mouse model. ECM presents an arranged and densely collagen matrix in which such fibres have a more and less aligned orientation, depending on the tumor section (Fig. 25). Collagen fibres producing significant detectable SHG signals have been identified as pathways promoting tumor cell locomotion[171]. This biased movement along collagen fibres positively correlates with increased metastatic behaviour. Thus, the extent of metastasis and the collagen structure were evaluated in the lungs of 4T1- breast cancer mice (Fig.26). 15 µm-tick FFPE lung slides were imaged with a 2-photon Leica SP8 DIVE FLIM microscope with a 25x immersion objective. SHG on the injured lungs of 4T1-bearing mice reveals dense and packed collagen fibre indicating pulmonary fibrosis (Fig. 26, a - yellow dashed line on the left), well differentiable from structural collagen maintaining the lung epithelium architecture (Fig. 26, b - yellow line on the right). Furthermore, the advanced stage and the disease aggressiveness were sustained by the tumor mass fully enriched in collagen shown at the bottom panel of figure 25 representing a large metastasis (Fig. 26, b). Therefore, SHG microscopy may provide relevant information concerning the tumor three-dimensional structure, serving as a tool for a more complete understanding of BC progression.

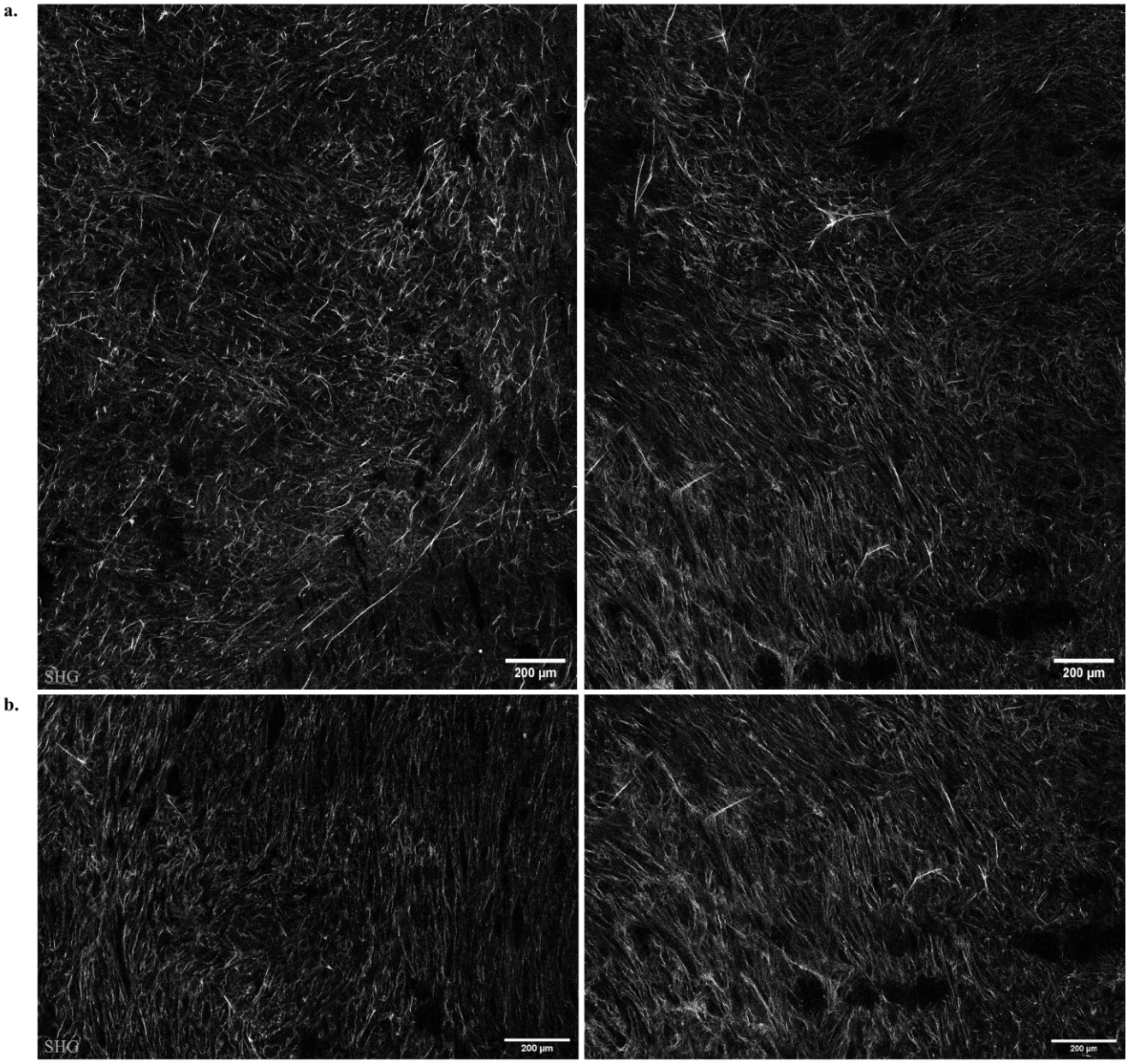

Figure 25. Orientation and linearization of collagen fibers in the tumor bulk of a 4T1 breast-cancer mouse model by second-harmonic generation (SHG). a,b) Representative images of thick and densely packed collagen fibers in 4T1-breast cancer. SHG (white). Samples were imaged with 2-photon Leica SP8 DIVE FLIM microscope, 25x magnification. Scale bar 200 µm.

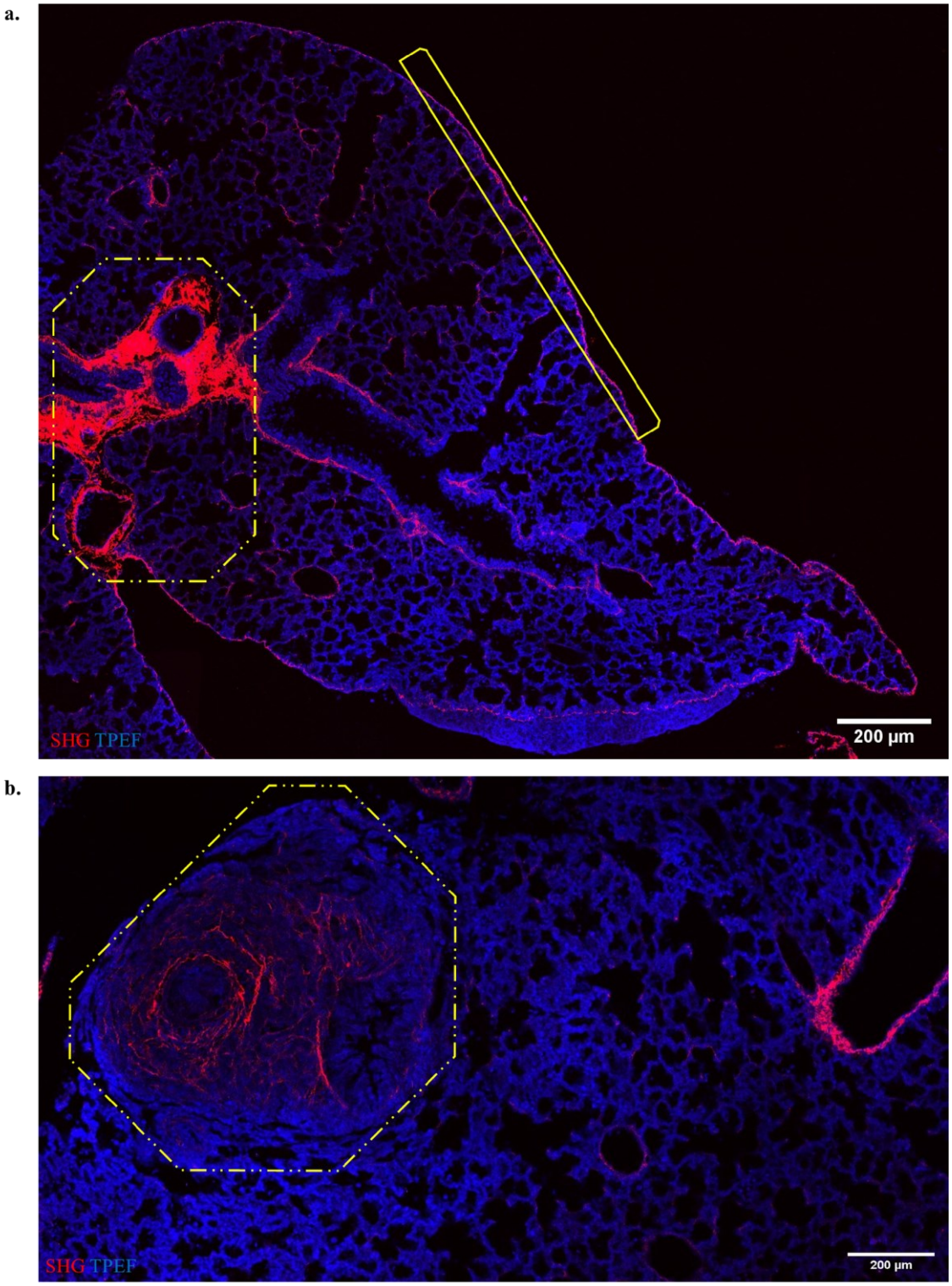

Figure 26. Second-harmonic generation (SHG) images of a metastatic lung of a 4T1 breast-cancer mouse model. a) The yellow dashed line on the left represents pulmonary fibrosis as indicated by the huge amount of collagen fibers. The yellow line on the right represents structural collagen maintaining the lung epithelium architecture. **b)** The yellow dashed line represents a tumor mass fully enriched in collagen. Two-photon-excited fluorescence microscopy (TPEF) (blue), and SHG (red). Samples were imaged with 2-photon Leica SP8 DIVE FLIM microscope, 25x magnification. Scale bar 200 µm.

4. Discussion

CIK cells represent an attractive approach for cell-based immunotherapy, as they are easy to obtain *in vitro* and they do not require genetic engineering procedures or additional modifications before infusion into patients[194,195]. However, CD19 CAR-T is currently considered the most advanced T-cell therapy in the clinical setting, demonstrating unprecedented efficacy[46,196,197]. Nonetheless, the patient's eligibility for CAR-T cell therapy is based on numerous exclusion criteria such as previous treatments, comorbidities, conserved renal and hepatic function, absence of central nervous system localization, and as well as adequate absolute lymphocyte count[198]. One particularly important point is that successful CAR-T cell manufacturing requires a considerable number of functional T cells, but prior treatments with lympho-toxic agents – such as chemotherapy drugs - may have a relevant impact on T cell function. Given these several reasons, a remarkable percentage of patients can not be eligible for CAR-T therapy, missing any further treatment perspective[199]. To overcome the first issues related to the huge amount of cells required in the clinical setting to treat cancer patients, we set up a serum-free protocol using the G-Rex® devices to expand CIK cells from peripheral blood by using X-VIVO 10 serum-free medium and clinical-grade cytokines. Such protocol led to CIK cell expansion in large numbers, with a minimal need for technical interventions, thus reducing the time and risks associated with culture manipulation. In line with the discovery that the successful clinical response of ACT products has been correlated with the percentage of naïve cells within the cell product[200,201], we found that CIK cells cultured under G-Rex6-6M protocol showed a more naïve phenotype, compared to CIK cells expanded with the conventional protocol. Indeed, CIK cells generated in conventional tissue culture flasks with FBS present a fully terminally differentiated (TEMRA) phenotype, defined by the expression of the following markers $CD45RA^+$, $CCR7^+$, CD62L low, $CD11a^+$, $CD27^+$, CD28, $MIP1a^+$, $perforin^+$, FAS $ligand^{+52}$. Interestingly, starting from just $2.5x10^6$ cells, almost $5x10^8$ cells are available in two weeks with the G-Rex6-6M protocol, meaning that even a small volume of peripheral blood can provide a sufficient amount of cells to repeatedly treat a 70 kg patient[202]. Moreover, the CIK cell expansion protocol results to be linear scale-up by using more capacious devices, namely G-Rex100M, without altering CIK cell phenotype and functionality. CIK cell expansions with the optimized protocol employing G-Rex devices is easier compared to CAR-T cell expansion, as it does not handle genetic engineering procedures, which are subjected to additional regulatory issues from medicinal agencies. Hence, the G-Rex system represents a valid chance for patients with inadequate absolute lymphocyte count, who are not eligible for CAR-T therapy[198]. Additionally, the production of effector cells for ACT from these patients is challenging because blood samples often contain contaminant tumor cells and very few percentages of $CD3^+$ T cells. To

obtain CIK cells from hematological patients, we optimized the previously described culture protocol by adding the bsAb CD3xCD19 Blina (BL-CIK protocol) to eliminate the malignant $CD19^+$ cells [179]. In the BL-CIK protocol, a single addition of Blina at the beginning of the expansion led to the concomitant expansion of CIK cells and the elimination of the malignant B cell fraction. Indeed, the elimination of residual malignant cells endowed with inhibitory and suppressive effects[203–205]might promote CIK cell expansion and fitness, thus increasing the treatment safety.

The BL-CIK protocol produced fully functional $CD3^+$ and $CD3^+CD56^+$ cellular subsets, with a higher proportion of naïve cells that might positively impact the efficacy of the therapy. Notably, such cells exhibited also an increased expression of CD27, known to be involved in the *in vivo* cell survival after adoptive transfer, and in the generation and long-term maintenance of T cell immune responses [206]. Overall, the Blina-based culture protocol allowed the expansion of functional CIK cells from all the patients, irrespective of the type of the underlying disease, and the generation of clinically relevant numbers of effector cells even starting from small volumes of peripheral blood, with extremely poor $CD3^+$ counts. In the view of a GMP translation, we argue that this protocol significantly reduces the number of culture manipulations and the time required to obtain a cell product free from residual tumor cells and ready to be administered, without the need for any immunomagnetic selection or depletion procedure.

Taking into account the renowned benefits in the production and manufacturing of CIK over CAR-T cells, we propose a novel combinatory therapeutic approach to offer an alternative strategy to treat patients with both solid and haematological malignancies. Indeed, we provided evidence that CIK cell anti-tumor activity can be further fostered both by the engagement of the CD16a receptor by tumor antigen-specific mAbs, leading to enhanced ADCC-mediated cytotoxicity[51,180], and by the combination with a CD3-bsAb. We exploited this therapeutic approach with CIK cells in the context of B-cell haematological cancers focusing on CD20-expressing malignancies, by combining CIK cells with two clinical-grade anti-CD20 mAbs, RTX or OBI. CIK cells showed a strong improvement in the lytic activity that was always more pronounced with OBI, consistently with the higher affinity for CD16a of its glycoengineered Fc domain, compared to RTX [121]. Overall, i*n vitro* results were well supported *in vivo* in an aggressive PDX mouse model derived from a refractory/relapsed patient since the CIK+OBI combination restrained tumor growth and prolonged mice survival. Thus, our data encourage the clinical application of CIK cells combined with mAbs already in clinical use for the treatment of B-cell malignancies. The success achieved concerning the haematological setting led us to further exploit the versatility of the combinatorial therapeutic strategy in solid tumors. Despite the paramount progress obtained from ACT in hematological cancers, several issues still hinder its

success for solid tumors – such as the difficulties in selecting the appropriate target, addressing T cells to the tumor and/or metastases, and reducing the risk of toxicities–. Considering the aggressiveness, younger onset, and poor prognosis, we decided to focus on Her-2/neu^{+} breast cancer addressing the anti-tumor activity of CIK cells with the clinical grade mAb TRS and the bsscFv Her2xCD3 antibody. To date, in addition to other chemotherapeutic agents, the neo-adjuvant therapy with the mAb TRS is the standard treatment available for both early and metastatic Her-2-expressing BC. However, apart from the severe TRS cardiotoxicity[207], clinical data report that the efficacy of TRS fails within one year of treatment initiation since the majority of patients with metastatic BC become resistant, or they still relapse despite TRS-based therapy[140]. In this thesis work, we show that the described TRS resistance in Her-2^{+} breast cancers can be overcome by combing the anti-tumor activity of CIK cells with TRS or with Her2xCD3 antibody. The bsscFv Her2xCD3 antibody in a BiTe-like format was designed from the fusion between the variable domains of two distinct monoclonal antibodies, the anti-CD3 specific single-chain, and the target Her-2 single-chain antibody[150]. As evidenced by flow cytometry, the Her2xCD3 antibody retains the antigen-specificities of the parental antibodies, binding specifically to CD3-expressing T cells and Her-2^{+} target cell lines. In terms of lytic activity *in vitro*, the combination of CIK cells with Her2xCD3 was significantly efficient in the killing of all tested Her-2-expressing cancer cell lines, over the combination of CIK cells with TRS. As a matter of fact, TRS-resistant tumor cell lines HCC1419 and HCC1569[181,182] showed to be sensitive to the Her2xCD3-CIK cell lytic effect. Emerging data show that sera from TRS-refractory patients are enriched with high levels of the inflammatory protein chitinase 3-like 1 (CHI3L1) compared with sera from responders and healthy controls[208,209]. Mechanistically, CHI3L1 impairs the correct polarization of the microtubule-organizing centre (MTOC) along with the lytic granules to the immune synapse, hence preventing the granule polarization downstream of NK cell signalling. Rescigno and colleagues demonstrated, both *in vitro* and *in vivo,* that recombinant CHI3L1 inhibits both ADCC and innate NK cell cytotoxicity, while the CHI3L1 blockade synergizes with ADCC to cure Her-2-xenografts mice[208]. This could explain whether cell lines endogenously expressing high levels of human CHI3L1, such as the mentioned above HCC1569 and HCC1419, are not or are non-completely sensitive to TRS activity[182], contrary to the strong and efficient lytic effect achieved by CIK cells combined with Her2xCD3. However, the lysis of the HCC1569 cell line observed when the activity of TRS was combined with the anti-tumor effect of CIK cells emphasizes the therapeutic advantage of the combinatory approach. The remarkable enhancement of CIK cell cytotoxicity mediated by the bsscFv Her2xCD3 was evident even at an extremely low E/T ratio, already after a 2-hour co-culture with Her-2^{+} target cells.

Importantly, we detected an increased secretion of IFN-γ, GM-CSF, TNF- α pro-inflammatory cytokines that was proportionally higher with the dosage of the Her2xCD3 antibody. Even though it is known that the hypersecretion of these cytokines by effector T cells may lead to clinically significant collateral damage activating bystander cells such as macrophages, neutrophils, or NK cells[184], we demonstrated that the combinatory tool Her2xCD3-CIK cells was efficient even at extremely low doses of Her2xCD3. Moreover, considering that the polyclonal activation of T cells mediated by the CD3-bsscFv may trigger a cytokine storm as an undesirable side effect[184], we did not detect any increase in the concentration of CRS-associated cytokines – such as IL-5 and IL-6 – after the co-culture with Her2xCD3-CIK cells and target cells. Herein, we show that the treatment of Her-2-expressing breast tumors with CIK cells and the bsscFv Her2xCD3 antibody could represent a promising approach to prevent treatment resistance and increase the number of responders. Nonetheless, ongoing *in vivo* experiments on a subcutaneous PDX model of Her-2^+ -primary tumor and an MCF-7- xenograft mouse model, endowed with the capacity to establish lung metastases, will provide a growing body of evidence about the functionality and efficacy of Her2xCD3-CIK cells combinatory therapy against both primary and metastatic Her-2^+ BC. Moreover, even though the safety of both CIK cells and bispecific antibodies is already validated in several clinical trials, the usage of a very low dosage of bsAbs to enhance CIK cell anti-tumor activity could minimize the possibility of side effects. This important issue can be assessed *in vivo* by employing humanized mice with a human immune system that is able to mimic what happens during a CRS.

Emerging data highlight that the composition of the microenvironment of Her-2-expressing tumors plays a crucial role in determining the sensitivity to Her-2-targeted therapies[158,159]. Considering the high complexity and heterogeneity of the TME in solid cancers, it is important to notice that, in preclinical studies *in vivo,* the employment of immunodeficient animal models (e.g., NOD/SCID, RAG2/$\gamma c^{-/-}$ partially or completely lympho-ablated) may overlooking TME impact on immunotherapy outcomes [210]. The development of PDX models, with an intact ECM architecture and stromal component, represents a powerful tool to predict the efficacy of cancer therapeutics [72]. However, these models lack immune cells and are not unsuitable to study the human tumor immune microenvironment. Conversely, the use of immunocompetent mouse models allows the study of the complex multicellular interactions between adoptively transferred cells and the TME niche as a whole, but they are unable to fully recapitulate the human tumor microenvironment. Over the last decades, advances in 3D cultures *in vitro* are providing new models for translating basic knowledge into novel treatments for cancer. Several *in vitro* systems have been developed to

investigate cellular trafficking and infiltration of effector cells in solid tumors, for example, tumor spheroids, organoids, 3D bio-printing, microfluidics, and scaffold-based approaches[211]. Even though such systems mimic the structure of native tissue, they lack other important cellular and soluble factors. In this regard, the *ex vivo* imaging technique on fresh slices from explanted tumor tissue represents a promising tool that preserves the tissue 3D architecture, the pathway activity, and the complexity of the multicellular TME, representing a good compromise between co-culture studies and animal models[186,192]. Indeed, such *ex vivo* imaging technique could mimic in real-time an adoptive cell transfer experiment, allowing the identification of extracellular factors involved in T cell motility or the follow-up of T cell trafficking in fresh tumor slices. In recent years, this technique has been successfully employed for the study in real-time of cellular interplay taking place in the TME or for the investigation of molecular mechanisms - such as - the measurement of Ca^{2+} responses in thymocytes and T cells upon antigen recognition [212]. To gain insight into the trafficking and the infiltration of transferred cells in our experiment, we started a collaboration with the laboratory of Dr. E. Donnadieu at the Cochin Institute since they recently optimized the *ex vivo* slice assay[186,192]. Representative data shown in this thesis work sustain that the technique is easily customizable for the study of the crosstalk and spatial interactions occurring between several immune populations in the TME on fixed tissue slices. Overall, the possibility to combine the tumor slice assay with the high-resolution SDCLM significantly improves the data outcome. Indeed, in conventional widefield optical microscopy, the ability to capture fine detail above the out-of-focus signal becomes increasingly challenging as the sample increases in thickness. Especially, this occurs because the specimen is bathed in the light used to excite fluorophores, thus the fluorescence emitted by the specimen outside the focal plane of the objective interferes with the resolution of in-focus features. Conversely, in CLSM the sample is illuminated by a single point of light from a laser through the use of a pinhole. The laser beam is scanned point by point in a raster pattern and the signal is detected sequentially from each point by a photomultiplier tube (PMTs) until an entire image is created. Even though this technique generates high-quality images, the disadvantage is the very slow speed and the considerable photobleaching and photodamage caused by the poor efficiency of the PTMs used to detect light, whose quantum efficiency (the probability of converting a photon to an electron) is rather low - typically 30-40%[213]. SDCLM overcomes CLSM limitations by exploiting the multiplex principle and it is now considered the gold standard method to image samples with a small to medium thickness. Indeed, in SDCLM the sample is simultaneously illuminated by thousands of light spots since each microlens presents an associated pinhole laterally co-aligned on a second pinhole disk (Fig. 8) allowing the collection of more than three hundred frames per second. Furthermore, the

multiple-time point-by-point illumination with a lower amount of photons/time results in reduced photobleaching and photodamage, making SDCLM more suitable for 3-dimensional imaging of live cells[214,215].

Concerning solid cancer, it is also noteworthy to mention the impact of non-cellular components in determining tumor fate. Relative to the healthy breast, in BC changes in the overall organization of the extracellular-matrix, generate a dense physical barrier and an increased interstitial pressure (Fig.4), resulting in aberrant signalling and directly impacting drug delivery and therapy efficacy[154,160]. The most well-recognized ECM alteration occurring inside the tumor is the increased collagen deposition [161–166]. As collagen is the most regulator of the biophysical and biochemical properties of TME, it impacts cancer cell polarity, migration, and signaling[167–170], and in BC higher deposition of collagen correlates with worse prognosis[172,173,193]. Interestingly, fibrillar collagen can produce an intrinsic optical signal literally called a second-harmonic generation. To further investigate the tumor structure - in terms of the stiffness of ECM collagen - in the *in vivo* BC-mouse models, we took advantage of a label-free SHG microscopy. SHG microscopy is based on the nonlinear optical process occurring when two photons scatter off a noncentrosymmetric material - such as a collagen fibre- and produce a single photon with exactly twice the energy of the initial photons[177]. Such phenomenon arises out of the noncentrosymmetric assembly of these two photons, therefore called "harmonophores", in a permanent dipole moment[176,177]. Representative images here reported about SHG signal in the tumor bulk of a 4T1-bearing-mouse show an arranged and densely collagen matrix in which collagen fibres present a more and less aligned orientation. Otherwise, the SHG signal in the injured lungs of 4T1-bearing mice allows to well visualize and distinguish structural collagen maintaining the lung epithelium architecture from the fibrotic area and the tumor mass fully enriched in collagen. Thus, SHG microscopy can provide information about both the individual collagen fiber orientation and the overall organization of tumor ECM. Therefore, the collagen score measurement and the study of collagen fiber orientation[171] by SHG microscopy could represent a prognostic indicator for cancer progression, having a crucial impact in clinical advances.

In the present study, we introduce CIK cells combined with clinical-grade monoclonal and bispecific antibodies as a potential pharmacological tool for cancer immunotherapy over other cellular therapies for a broad spectrum of cancer types. Herein, we provide preliminary evidence that the Her2xCD3-CIK cell combinatory strategy can be considered a valuable therapeutic solution for Her-2^{+}-breast cancer overcoming treatment resistance, thus increasing the number of responders. We are currently working on two *in vivo* $Her2^{+}$-mouse models to validate the functionality and efficacy of Her2xCD3-

CIK cell therapy against both primary and metastatic Her-2^{+} BC. With the purpose to contribute to the progress of ACT in the context of solid cancers, the future perspectives of this study aim to gain insight into the trafficking and the survival of adoptively transferred CIK cells *in vivo* and to investigate how CIK cell interact with the other immune cell populations present in the TME to decipher potential inhibitor factors that could negatively impact CIK cell-killing activity.

5. Table and abbreviation

5.1 Table

Patient		Day 0						Day 14					
								BL-CIK			CIK		
		State	*WCC ($x10^9$/L)*	*Blood volume (mL)*	*Total number of PBMCs ($x10^6$)*	*Total number of $CD3^+$ cells ($x10^6$)*	*Seeded cells ($x10^6$)*	*Number of cells harvested ($x10^6$)*	*fold increase*	*Hypothetical yield of cells ($x10^6$)[a]*	*Number of cells harvested ($x10^6$)*	*fold increase*	*Hypothetical yield of cells ($x10^6$)[a]*
CLL1	*relapsed*	fresh	49.3	18	91.0	7.2	5	67.4	13.5	1226.7	32	6.4	582.4
CLL2	*relapsed*	fresh	5.2	15	42.0	1.3	5	103.5	20.7	869.4	5.9	1.2	49.6
CLL3	*naïve*	fresh	50.7	15	330.0	2.9	5	84.1	8.4	2775.3	5.5	1.5	478.5
CLL4	*naïve*	fresh	61.2	18	420.0	0.8	5	29.6	14.8	6216.0	7.9	3.7	1541.4
MCL1	*naïve*	thawed	336.3	18	3200.0	5.0	5	59.1	11.8	37824.0	1.1	0.2	704.0
MCL2	*relapsed*	fresh	23.6	15	322.0	2.2	5	13.7	2.7	882.3	3.5	0.7	225.4
SMZL 1	*naïve*	thawed	27.0	18	590.0	0.5	5	126.3	25.3	14903.4	14.2	2.8	1675.6
SMZL 2	*relapsed*	fresh	24.1	18	300.0	3.3	5	33.2	6.6	1992.0	20.6	4.1	1236.0
B-ALL	*relapsed*	fresh	23.0	15	100.0	14.7	5	16.6	3.3	332.0	10.1	2.0	202.0
	mean		66.7	16.7	599.4	4.2		59.3	11.9	7446.8	11.2	2.5	743.9
	SD		102.6	1.6	990.8	4.5		39.7	7.6	12283.8	9.8	2.0	600.9
	median		27.0	18.0	322.0	2.9		59.1	11.8	1992.0	7.9	2.0	582.4

[a] Yield calculated considering the total number of PBMCs obtained from the sample.

Table 1: Yields of CIK cell expansion from PBMCs obtained from B-cell lymphoma patients.

	% $CD3^+$			% $CD19^+$			% $CD20^+$			% $CD3^+CD56^+$		
	Day 0	Day 14		Day 0	Day 14		Day 0	Day 14		Day 0	Day 14	
Patient		BL-CIK	CIK		BL-CIK	CIK		BL-CIK	CIK		BL-CIK	CIK
CLL1	14.7	96.2	93.5	65.8	0.0	1.2	11.2	0.0	0.0	nd	55.9	60.6
CLL2	25.0	99.0	87.9	55.0	0.0	0.0	51.3	0.0	0.0	8.0	82.1	14.9
CLL3	5.8	99.2	88.1	62.6	0.0	10.6	67.7	0.0	13.4	0.4	40.6	15.2
CLL4	1.4	94.4	91.3	36.0	1.3	2.2	21.8	0.7	2.7	nd	23.6	26.7
MCL1	1.5	100	59.7	91.3	0.0	12.3	91.6	0.0	3.1	0	35.1	9.7
MCL2	9.3	94.2	71.3	30.0	0.0	1.4	30.0	0.0	0.1	0.4	75.3	51.0
SMZL 1	1.8	97.6	84.1	90.9	0.0	2.6	90.9	2.0	13.3	0	6.3	13.9
SMZL 2	13.5	98.3	95.6	38.3	0.0	0.6	37.6	0.0	0.4	nd	53.1	57.4
B-ALL	63.8	97.3	94.4	6.4	0.0	0.0	7.0	0.0	0.0	5.7	35.6	37.4

mean	15.2	97.4	85.1	52.9	0.1	3.4	45.5	0.3	3.7	2.4	45.3	31.9
SD	19.8	2.1	12.0	28.2	0.4	4.7	32.1	0.7	5.6	3.5	24.1	20.3
median	9.3	97.6	88.1	55.0	0.0	1.4	37.6	0.0	0.4	1.4	40.6	26.7

Table 2: Phenotype of CIK cell culture.

5.2 Abbreviation

ACT	Adoptive Cell Therapy
ADCs	Antibody Drug Conjugates
ADCC	Antibody-Dependent Cellular Cytotoxicity
α-GalCer	α-galactosylceramide
APCs	Antigen Presenting Cells
B-ALL	B-cell Acute Lymphoblastic Leukemia
BC	Breast Cancer
BiTe	Bispecific T cell engager
Blina	Blinatumumab
bsAb/ bsAbs	bispecific Antibody/ bispecific Antibodies
bsscFv	bispecific single-chain Fragment variable
CAFs	Cancer Associated Fibroblasts
calcein-AM	calcein-AcetoxyMethyl
CAR	Chimeric Antigen Receptor
CD	Cluster of Differentiation
CHI3L	Chitinase-3-like protein 1
CIK	Cytokine-Induced Killer
CLL	Chronic Lymphocytic Leukemia
CM	Central Memory
CLSM	Confocal Laser Scanner Microscopy
CTL	Cytotoxic T Lymphocyte
CTX	Cetuximab

DCs	Dendritic Cell
DMXAA	5,6-dimethylxanthenone-4-acetic acid
ECM	ExtraCellular Matrix
EGFR	Epidermal Growth Factor Receptor
EM	Effector Memory
EMA	European Medicines Agency
EMRA	Effector Memory RA^+
ER	Estrogen Receptor
E:T ratio	Effector to Target ratio
FAK	Focal Adhesion Kinase
FBS	Fetal Bovine Serum
Fc	Antibody Fragment Crystallizable Region
FDA	Food and Drug Administration
FFPE	Formalin-Fixed Paraffin Embedded
fmIHC	fluorescent multiplex Immuno Histochemistry
GMP	Good Manufacturing Practices
G-Rex	Gas-permeable Rapid expansion
GvHD	Graft versus Host Disease
HER	Human Epidermal growth factor Receptor
HIER	Heat Induced Epitope Retrival
HLA	Human Leukocyte Antigen
HRP	HorseRadish Peroxidase
IFN-γ	Interferon-γ
Ig	Immunoglobulin
IgG	Immunoglobulin G
IHC	immunohistochemistry
IL-2	Interleukin-2
IL-6	Interleukin-6
IL-12	Interleukin-12

IL-15	Interleukin-15
Iso	Isotype control antibody
i.t.	intratumor
i.v.	intravenous
LAK	Lymphokine-Activated Killer
LFA	Lymphocyte Function-associated Antigen
LFA-1	Lymphocyte Function-associated Antigen-1
LFA-3	Lymphocyte Function-associated Antigen-3
LIF	Leukemia Inhibitory Factor
mAb/mAbs	monoclonal Antibody/ monoclonal Antibodies
MAPK	Mitogen-Activated Protein Kinase
MCL	Mantle Cell Lymphoma
MFI	Mean Fluorescent Intensity
MHC	Major Histocompatibility Complex
N	Naïve
neu	neuregulin
NF-κB	Nuclear Factor kappa-light-chain-enhancer of activated B cells
NHL	Non-Hodgkin Lymphoma
NK	Natural Killer
NKG2D	Natural-Killer group 2 member D
NK-T	Natural Killer T
NSG	NOD/SCID common γ chain knockout
OBI	Obinutuzumab
OS	Overall Survival
OVs	Oncolytic Viruses
PBMCs	Peripheral Blood Mononuclear Cells
PDX	Patient-Derived Xenograft
PI3K	PhosphatidylInositol 3-Kinase
PLP	periodate-lysine-paraformaldehyde
PMTs	Photomultiplier Tubes

PR	Progesteron Receptor
rhIFNγ	recombinant human Interferon-γ
rh IL-2	recombinant human Interleukin-2
RPMI	Roswell Park Memorial Institute
RTCA	Real-Time Cell Analysis
RTX	Rituximab
s.c.	subcutaneous
scFv	single chain Fragment variable
SD	standard Deviation
SDCLM	Spinning Disk Confocal Laser Microscopy
SHG	Second Harmonic Generation
STING	STimulator of INterferon genes
TACSs	Tumor Associated Collagen Signatures
TCR	T-cell Receptor
TILs	Tumor Infiltrating Lymphocytes
Tp-PyMT	Transplanted polyoma middle T antigen
TME	Tumor Microenvironment
TNBC	Triple Negative Breast Cancer
TNF-α	Tumor Necrosis Factor-α
TPEF	two-photon excitation microscopy
T_{reg}	regulatory T
WHO	World Health Organisation

6. Bibliography

1. Ferlay, J. *et al.* Cancer statistics for the year 2020: An overview. *Int. J. Cancer* **149**, 778–789 (2021).
2. Sung, H. *et al.* Global Cancer Statistics 2020: GLOBOCAN Estimates of Incidence and Mortality Worldwide for 36 Cancers in 185 Countries. *CA. Cancer J. Clin.* **71**, 209–249 (2021).
3. Rosenberg, S. A. & Restifo, N. P. Adoptive cell transfer as personalized immunotherapy for human cancer. *Science (80-.).* **348**, 62–68 (2015).
4. Galluzzi, L. *et al.* Classification of current anticancer immunotherapies. *Oncotarget* **5**, 12472–12508 (2014).
5. Cable, J. *et al.* Frontiers in cancer immunotherapy-a symposium report. *Ann. N. Y. Acad. Sci.* **1489**, 30–47 (2021).
6. Bonini, C. & Mondino, A. Adoptive T-cell therapy for cancer : The era of engineered T cells Adoptive T-cell therapy : A historical. *Eur. J. Immunol.* **45**, 2457–2469 (2015).
7. Rosenberg, S. A. *et al.* Use of Tumor-Infiltrating Lymphocytes and Interleukin-2 in the Immunotherapy of Patients with Metastatic Melanoma. *N. Engl. J. Med.* **319**, 1676–1680 (1988).
8. Grimm, E. A., Mazumder, A., Zhang, H. Z. & Rosenberg, S. A. Lymphokine-activated killer cell phenomenon. Lysis of natural killer-resistant fresh solid tumor cells by interleukin 2-activated autologous human peripheral blood lymphocytes. *J. Exp. Med.* **155**, 1823–1841 (1982).
9. Lim, O., Jung, M. Y., Hwang, Y. K. & Shin, E.-C. Present and Future of Allogeneic Natural Killer Cell Therapy. *Front. Immunol.* **6**, 1–8 (2015).
10. Lafont, V. *et al.* Plasticity of γδ T cells: impact on the anti-tumor response. *Front. Immunol.* **5**, 1–13 (2014).
11. Terabe, M. & Berzofsky, J. A. The Role of NKT Cells in Tumor Immunity. *Adv. Cancer Res.* **101**, 277–348 (2008).
12. Cappuzzello, E., Sommaggio, R., Zanovello, P. & Rosato, A. Cytokines for the induction of antitumor effectors : The paradigm of Cytokine-Induced Killer (CIK) cells. *Cytokine Growth Factor Rev.* 1–7 (2017) doi:10.1016/j.cytogfr.2017.06.003.
13. Shafer, P., Kelly, L. M. & Hoyos, V. Cancer Therapy With TCR-Engineered T Cells: Current Strategies, Challenges, and Prospects. *Front. Immunol.* **13**, 835762 (2022).
14. June, C. H., Riddell, S. R. & Schumacher, T. N. Adoptive cellular therapy : A race to the finish line. *Sci. Transl. Med.* **7**, 1–9 (2015).

15. Miller, J. S. *et al.* Low dose subcutaneous interleukin-2 after autologous transplantation generates sustained in vivo natural killer cell activity. *Biol. Blood Marrow Transplant.* **3**, 34–44 (1997).

16. Burns, L. J. *et al.* IL-2-based immunotherapy after autologous transplantation for lymphoma and breast cancer induces immune activation and cytokine release: a phase I/II trial. *Bone Marrow Transplant.* **32**, 177–186 (2003).

17. Dalle, J.-H. *et al.* Characterization of Cord Blood Natural Killer Cells: Implications for Transplantation and Neonatal Infections. *Pediatr. Res.* **57**, 649–655 (2005).

18. Luevano, M. *et al.* The unique profile of cord blood natural killer cells balances incomplete maturation and effective killing function upon activation. *Hum. Immunol.* **73**, 248–257 (2012).

19. Tanaka, H. *et al.* Analysis of natural killer (NK) cell activity and adhesion molecules on NK cells from umbilical cord blood. *Eur. J. Haematol.* **71**, 29–38 (2003).

20. Suck, G. *et al.* NK-92: an 'off-the-shelf therapeutic' for adoptive natural killer cell-based cancer immunotherapy. *Cancer Immunol. Immunother.* **65**, 485–492 (2016).

21. Knorr, D. A. *et al.* Clinical-Scale Derivation of Natural Killer Cells From Human Pluripotent Stem Cells for Cancer Therapy. *Stem Cells Transl. Med.* **2**, 274–283 (2013).

22. Woll, P. S. *et al.* Human embryonic stem cells differentiate into a homogeneous population of natural killer cells with potent in vivo antitumor activity. *Blood* **113**, 6094–6101 (2009).

23. Hermanson, D. L. *et al.* Induced Pluripotent Stem Cell-Derived Natural Killer Cells for Treatment of Ovarian Cancer. *Stem Cells* **34**, 93–101 (2016).

24. Yang, Y. *et al.* Phase I Study of Random Healthy Donor–Derived Allogeneic Natural Killer Cell Therapy in Patients with Malignant Lymphoma or Advanced Solid Tumors. *Cancer Immunol. Res.* **4**, 215–224 (2016).

25. Iliopoulou, E. G. *et al.* A phase I trial of adoptive transfer of allogeneic natural killer cells in patients with advanced non-small cell lung cancer. *Cancer Immunol. Immunother.* **59**, 1781–1789 (2010).

26. Geller, M. A. *et al.* A phase II study of allogeneic natural killer cell therapy to treat patients with recurrent ovarian and breast cancer. *Cytotherapy* **13**, 98–107 (2011).

27. Wu, Y.-L. *et al.* γδ T cells and their potential for immunotherapy. *Int. J. Biol. Sci.* **10**, 119–135 (2014).

28. Yazdanifar, M., Barbarito, G., Bertaina, A. & Airoldi, I. γδ T cells: the ideal tool for cancer immunotherapy. *Cells* **9**, 1305 (2020).

29. Kunzmann, V. *et al.* Tumor-promoting Versus Tumor-antagonizing Roles of γδ T Cells in Cancer Immunotherapy. *J. Immunother.* **35**, 205–213 (2012).

30. Wilhelm, M. *et al.* γδ T cells for immune therapy of patients with lymphoid malignancies. *Blood* **102**, 200–206 (2003).

31. Zhao, Y., Niu, C. & Cui, J. Gamma-delta (γδ) T cells: friend or foe in cancer development? *J. Transl. Med.* **16**, 3 (2018).

32. Silva-Santos, B., Serre, K. & Norell, H. γδ T cells in cancer. *Nat. Rev. Immunol.* **15**, 683–691 (2015).

33. Hill, T. M., Bezbradica, J. S., Van Kaer, L. & Joyce, S. CD1d-Restricted Natural Killer T Cells. in *eLS* 1–27 (John Wiley & Sons, Ltd, 2016). doi:10.1002/9780470015902.a0020180.pub2.

34. Nair, S. & Dhodapkar, M. V. Natural Killer T Cells in Cancer Immunotherapy. *Front. Immunol.* **8**, (2017).

35. Morgan, R. A. *et al.* Cancer Regression and Neurological Toxicity Following Anti-MAGE-A3 TCR Gene Therapy. *J. Immunother.* **36**, 133–151 (2013).

36. Norberg, S. M. *et al.* Regression of Epithelial Cancers Following T Cell Receptor Gene Therapy Targeting Human Papillomavirus-16 E7. *Blood* **132**, 492–492 (2018).

37. Norberg, S. *et al.* Safety and clinical activity of gene-engineered T-cell therapy targeting HPV-16 E7 for epithelial cancers. *J. Clin. Oncol.* **38**, 101–101 (2020).

38. Chandran, S. *et al.* Abstract CN01-03: T cell receptor gene therapy for a public neoantigen derived from mutated PIK3CA, a dominant driver oncogene in breast and endometrial cancers. in *Other Topics* CN01-03-CN01-03 (American Association for Cancer Research, 2019). doi:10.1158/1535-7163.TARG-19-CN01-03.

39. Larson, R. C. & Maus, M. V. Recent advances and discoveries in the mechanisms and functions of CAR T cells. *Nat. Rev. Cancer* **21**, 145–161 (2021).

40. Sadelain, M., Brentjens, R. & Rivière, I. The Basic Principles of Chimeric Antigen Receptor Design. *Cancer Discov.* **3**, 388–398 (2013).

41. Johnson, P. C. & Abramson, J. S. Patient selection for chimeric antigen receptor (CAR) T-cell therapy for aggressive B-cell non-Hodgkin lymphomas. *Leuk. Lymphoma* **61**, 2561–2567 (2020).

42. Gust, J., Taraseviciute, A. & Turtle, C. J. Neurotoxicity Associated with CD19-Targeted CAR-T Cell Therapies. *CNS Drugs* **32**, 1091–1101 (2018).

43. Hay, K. A. *et al.* Kinetics and biomarkers of severe cytokine release syndrome after CD19 chimeric antigen receptor–modified T-cell therapy. *Blood* **130**, 2295–2306 (2017).

44. Bear, A. S., Fraietta, J. A., Narayan, V. K., O'Hara, M. & Haas, N. B. Adoptive Cellular Therapy for Solid Tumors. *Am. Soc. Clin. Oncol. Educ. B.* 57–65 (2021) doi:10.1200/EDBK_321115.

45. Rodriguez-Garcia, A., Palazon, A., Noguera-Ortega, E., Powell, D. J. & Guedan, S.

CAR-T Cells Hit the Tumor Microenvironment: Strategies to Overcome Tumor Escape. *Front. Immunol.* **11**, 1–17 (2020).

46. Maude, S. L., Teachey, D. T., Porter, D. L. & Grupp, S. A. CD19-targeted chimeric antigen receptor T-cell therapy for acute lymphoblastic leukemia. *Blood* **125**, 4017–23 (2015).

47. Maude, S. L. *et al.* Tisagenlecleucel in Children and Young Adults with B-Cell Lymphoblastic Leukemia. *N. Engl. J. Med.* **378**, 439–448 (2018).

48. Schmidt-Wolf, I. G., Negrin, R. S., Kiem, H. P., Blume, K. G. & Weissman, I. L. Use of a SCID mouse/human lymphoma model to evaluate cytokine-induced killer cells with potent antitumor cell activity. *J. Exp. Med.* **174**, 139–149 (1991).

49. Lu, P. H. & Negrin, R. S. A novel population of expanded human CD3+CD56+ cells derived from T cells with potent in vivo antitumor activity in mice with severe combined immunodeficiency. *J. Immunol.* **153**, 1687–96 (1994).

50. Schmidt-Wolf, G. D., Negrin, R. S. & Schmidt-Wolf, I. G. H. Activated T cells and cytokine-induced CD3+ CD56+ killer cells. *Ann. Hematol.* **74**, 51–56 (1997).

51. Cappuzzello, E., Tosi, A., Zanovello, P., Sommaggio, R. & Rosato, A. Retargeting cytokine-induced killer cell activity by CD16 engagement with clinical-grade antibodies. *Oncoimmunology* **5**, 1–10 (2016).

52. Franceschetti, M. *et al.* Cytokine-induced killer cells are terminally differentiated activated CD8 cytotoxic T-EMRA lymphocytes. *Exp. Hematol.* **37**, 616-628.e2 (2009).

53. Introna, M. *et al.* Rapid and massive expansion of cord blood-derived cytokine-induced killer cells: An innovative proposal for the treatment of leukemia relapse after cord blood transplantation. *Bone Marrow Transplant.* **38**, 621–627 (2006).

54. Hayes, M. P., Wang, J. & Norcross, M. A. Regulation of interleukin-12 expression in human monocytes: selective priming by interferon-gamma of lipopolysaccharide-inducible p35 and p40 genes. *Blood* **86**, 646–650 (1995).

55. Lopez, R. D., Waller, E. K., Lu, P. & Negrin, R. S. CD58 / LFA-3 and IL-12 provided by activated monocytes are critical in the in vitro expansion of CD56 + T cells. *Cancer Immunol. Immunother.* **49**, 629–640 (2001).

56. Van Wauwe, J., De Mey, J. & Goossens, J. OKT3 : a monoclonal anti-human T lymphocyte antibody with potent mitogenic properties. *J. Immunol.* **124**, 2708–2713 (1980).

57. Van Wauwe, J. P., Goossens, J. G. & Beverley, P. C. L. Human T lymphocyte activation by monoclonal antibodies ; OKT3 , but not UCHT1 , triggers mitogenesis via an interleukin 2-dependent mechanism. *J. Immunol.* **133**, 129–132 (1984).

58. Sangiolo, D. *et al.* Alloreactivity and anti-tumor activity segregate within two distinct subsets of cytokine-induced killer (CIK) cells: implications for their infusion across

major HLA barriers. *Int. Immunol.* **20**, 841–848 (2008).

59. Bremm, M. *et al.* Improving Clinical Manufacturing of IL-15 Activated Cytokine-Induced Killer (CIK) Cells. *Front. Immunol.* **10**, (2019).

60. Märten, A. *et al.* Interactions between dendritic cells and cytokine-induced killer cells lead to an activation of both populations. *J. Immunother.* **24**, 502–10 (2001).

61. Wang, X. *et al.* Cytokine-induced killer cell/dendritic cell–cytokine-induced killer cell immunotherapy for the postoperative treatment of gastric cancer. *Medicine (Baltimore).* **97**, e12230 (2018).

62. Schmidt-Wolf, I. G. H., Negrin, R. S., Kiem, H. P., Blume, K. G. & Weissman, I. L. Use of a SCID mouse/human lymphoma model to evaluate cytokine-induced killer cells with potent antitumor cell activity. *J. Exp. Med.* **174**, 139–149 (1991).

63. Zoll, B. *et al.* Generation of cytokine-induced killer cells using exogenous interleukin-2, -7 or -12. *Cancer Immunol. Immunother.* **47**, 221–226 (1998).

64. Lin, G. *et al.* Interleukin-6 inhibits regulatory T cells and improves the proliferation and cytotoxic activity of cytokine-induced killer cells. *J. Immunother.* **35**, 337–43 (2012).

65. Pievani, A. *et al.* Dual-functional capability of CD3+CD56+CIK cells, a T-cell subset that acquires NK function and retains TCR-mediated specific cytotoxicity. *Blood* **118**, 3301–3310 (2011).

66. Verneris, M. R., Baker, J., Edinger, M. & Negrin, R. S. Studies of ex vivo activated and expanded CD8+ NK-T cells in humans and mice. *J. Clin. Immunol.* **22**, 131–136 (2002).

67. Schmidt-Wolf, I. G. *et al.* Phenotypic characterization and identification of effector cells involved in tumor cell recognition of cytokine-induced killer cells. *Exp. Hematol.* **21**, 1673–1679 (1993).

68. May, C., Sapra, P. & Gerber, H. P. Advances in bispecific biotherapeutics for the treatment of cancer. *Biochem. Pharmacol.* **84**, 1105–1112 (2012).

69. Kellner, C., Derer, S., Valerius, T. & Peipp, M. Boosting ADCC and CDC activity by Fc engineering and evaluation of antibody effector functions. *Methods* **65**, 105–113 (2014).

70. Karami, M. A., Cao, T. M., Baker, J., Verneris, M. R. & Negrin, R. S. Silencing human NKG2D, DAP10 and DAP12 reduces cytotoxicity of in vivo activated CD8+ T and NK cells. *Biol. Blood Marrow Transplant.* **11**, 41 (2005).

71. Verneris, M. R., Karami, M., Baker, J., Jayaswal, A. & Negrin, R. S. Role of NKG2D signaling in the cytotoxicity of activated and expanded CD8+ T cells. *Blood* **103**, 3065–3073 (2004).

72. Sommaggio, R. *et al.* Adoptive cell therapy of triple negative breast cancer with redirected cytokine-induced killer cells. *Oncoimmunology* **9**, 1777046 (2020).

73. Nishimura, R. *et al.* In vivo trafficking and survival of cytokine-induced killer cells resulting in minimal GVHD with retention of antitumor activity. *Blood* **112**, 2563–2574 (2008).

74. Verneris, M. R. *et al.* Engineering hematopoietic grafts: purified allogeneic hematopoietic stem cells plus expanded CD8+ NK-T cells in the treatment of lymphoma. *Biol. Blood Marrow Transplant.* **7**, 532–42 (2001).

75. Schwartz, R. N., Stover, L. & Dutcher, J. P. Managing toxicities of high-dose interleukin-2. *Oncology (Williston Park).* **16**, 11–20 (2002).

76. Yang, Y. G., Dey, B. R., Sergio, J. J., Pearson, D. a & Sykes, M. Donor-derived interferon gamma is required for inhibition of acute graft-versus-host disease by interleukin 12. *J. Clin. Invest.* **102**, 2126–2135 (1998).

77. Baker, J., Verneris, M. R., Ito, M., Shizuru, J. A. & Negrin, R. S. Expansion of cytolytic CD8+ natural killer T cells with limited capacity for graft-versus-host disease induction due to interferon γ production. *Blood* **97**, 2923–2931 (2001).

78. Kong, D.-S. *et al.* Phase III randomized trial of autologous cytokine-induced killer cell immunotherapy for newly diagnosed glioblastoma in korea. *Oncotarget* **8**, 7003–7013 (2017).

79. Lu, X. chun *et al.* Clinical Study of Autologous Cytokine-Induced Killer Cells for the Treatment of Elderly Patients with Diffuse Large B-Cell Lymphoma. *Cell Biochem. Biophys.* **62**, 257–265 (2012).

80. Leemhuis, T., Wells, S., Scheffold, C., Edinger, M. & Negrin, R. S. A phase I trial of autologous cytokine-induced killer cells for the treatment of relapsed Hodgkin disease and non-Hodgkin lymphoma. *Biol. Blood Marrow Transplant.* **11**, 181–187 (2005).

81. Chan, J. K. *et al.* Enhanced killing of primary ovarian cancer by retargeting autologous cytokine-induced killer cells with bispecific antibodies: a preclinical study. *Clin. Cancer Res.* **12**, 1859–67 (2006).

82. Olioso, P. *et al.* Immunotherapy with cytokine induced killer cells in solid and hematopoietic tumours: a pilot clinical trial. *Hematol. Oncol.* **27**, 130–9 (2009).

83. Introna, M. *et al.* Repeated infusions of donor-derived cytokine-induced killer cells in patients relapsing after allogeneic stem cell transplantation: a phase I study. *Haematologica* **92**, 952–9 (2007).

84. Laport, G. G. *et al.* Adoptive Immunotherapy with Cytokine-Induced Killer Cells for Patients with Relapsed Hematologic Malignancies after Allogeneic Hematopoietic Cell Transplantation. *Biol. Blood Marrow Transplant.* **17**, 1679–1687 (2011).

85. Linn, Y. C. *et al.* The anti-tumour activity of allogeneic cytokine-induced killer cells in patients who relapse after allogeneic transplant for haematological malignancies. *Bone Marrow Transplant.* **47**, 957–966 (2012).

86. Wang, S. *et al.* Human leukocyte antigen-haploidentical donor-derived

cytokine-induced killer cells are safe and prolong the survival of patients with advanced non-small cell lung cancer. *Oncol. Lett.* **8**, 2727–2733 (2014).

87. Du, Y. *et al.* Hydrogel-based co-delivery of CIK cells and oncolytic adenovirus armed with IL12 and IL15 for cancer immunotherapy. *Biomed. Pharmacother.* **151**, 113110 (2022).

88. Cao, J., Kong, F.-H., Liu, X. & Wang, X.-B. Immunotherapy with dendritic cells and cytokine-induced killer cells for hepatocellular carcinoma: A meta-analysis. *World J. Gastroenterol.* **25**, 3649–3663 (2019).

89. Zhao, P. *et al.* Dendritic cell immunotherapy combined with cytokine-induced killer cells promotes skewing toward Th2 cytokine profile in patients with metastatic non-small cell lung cancer. *Int. Immunopharmacol.* **25**, 450–6 (2015).

90. Capellero, S. *et al.* Preclinical immunotherapy with Cytokine-Induced Killer lymphocytes against epithelial ovarian cancer. *Sci. Rep.* **10**, 1–11 (2020).

91. Li, Y. *et al.* A Combination of Cytokine-Induced Killer Cells With PD-1 Blockade and ALK Inhibitor Showed Substantial Intrinsic Variability Across Non-Small Cell Lung Cancer Cell Lines. *Front. Oncol.* **12**, (2022).

92. Leuci, V. *et al.* CSPG4-specific CAR.CIK lymphocytes as a novel therapy for the treatment of multiple soft-tissue sarcoma histotypes. *Clin. Cancer Res.* **26**, 6321–6334 (2020).

93. Franceschetti, M. *et al.* Cytokine-induced killer cells are terminallydifferentiated activated CD8 cytotoxic T-EMRA lymphocytes. *Exp. Hematol.* **37**, 616–628 (2009).

94. Godfrey, D. I., MacDonald, H. R., Kronenberg, M., Smyth, M. J. & Van Kaer, L. NKT cells: What's in a name? *Nat. Rev. Immunol.* **4**, 231–237 (2004).

95. Baker, J., Verneris, M. R., Ito, M., Shizuru, J. a. & Negrin, R. S. Expansion of cytolytic CD8+ natural killer T cells with limited capacity for graft-versus-host disease induction due to interferon ?? production. *Blood* **97**, 2923–2931 (2001).

96. Godfrey, D. I. & Rossjohn, J. New ways to turn on NKT cells. *J. Exp. Med.* **208**, 1121–5 (2011).

97. Okada, H., Nagamura-Inoue, T., Mori, Y. & Takahashi, T. A. Expansion of Vα24+Vβ11+ NKT cells from cord blood mononuclear cells using IL-15, IL-7 and Flt3-L depends on monocytes. *Eur. J. Immunol.* **36**, 236–244 (2006).

98. Kawano, T. *et al.* CD1d-Restricted and TCR-Mediated Activation of V α 14 NKT Cells by Glycosylceramides. *Science (80-.).* **278**, 1626–1629 (1997).

99. Sun, Z. *et al.* Immune modulation and safety profile of adoptive immunotherapy using expanded autologous activated lymphocytes against advanced cancer. *Clin. Immunol.* **138**, 23–32 (2011).

100. Rosenberg, S. A. *et al.* Durable complete responses in heavily pretreated patients with metastatic melanoma using T-cell transfer immunotherapy. *Clin. Cancer Res.* **17**,

4550–4557 (2011).

101. Meng, Y. *et al.* Cell-based immunotherapy with cytokine-induced killer (CIK) cells: From preparation and testing to clinical application. *Hum. Vaccines Immunother.* **13**, 1379–1387 (2017).

102. Meng, Y. *et al.* Rapid expansion in the WAVE bioreactor of clinical scale cells for tumor immunotherapy. *Hum. Vaccines Immunother.* **14**, 2516–2526 (2018).

103. Palmerini, P. *et al.* A serum-free protocol for the ex vivo expansion of Cytokine-Induced Killer cells using gas-permeable static culture flasks. *Cytotherapy* (2020) doi:10.1016/j.jcyt.2020.05.003.

104. Vera, J. F. *et al.* Accelerated Production of Antigen-specific T Cells for Preclinical and Clinical Applications Using Gas-permeable Rapid Expansion Cultureware (G-Rex). *J. Immunother.* **33**, 305–315 (2010).

105. Jin, J. *et al.* Simplified method of the growth of human tumor infiltrating lymphocytes in gas-permeable flasks to numbers needed for patient treatment. *J. Immunother.* **35**, 283–292 (2012).

106. Forget, M. A. *et al.* The beneficial effects of a gas-permeable flask for expansion of Tumor-Infiltrating lymphocytes as reflected in their mitochondrial function and respiration capacity. *Oncoimmunology* **5**, (2016).

107. Chakraborty, R. *et al.* Robust and cost effective expansion of human regulatory T cells highly functional in a xenograft model of graft-versus-host disease. *Haematologica* **98**, 533–537 (2013).

108. Lapteva, N. *et al.* Large-scale ex vivo expansion and characterization of natural killer cells for clinical applications. *Cytotherapy* **14**, 1131–1143 (2012).

109. Lapteva, N. & Vera, J. F. Optimization manufacture of virus- and tumor-specific T cells. *Stem Cells Int.* **2011**, 434392 (2011).

110. Arber, D. A. *et al.* The 2016 revision to the World Health Organization classification of myeloid neoplasms and acute leukemia. *Blood* **127**, 2391–2405 (2016).

111. Maloney, D. G. *et al.* IDEC-C2B8: Results of a Phase I Multiple-Dose Trial In Patients With Relapsed Non-Hodgkin's Lymphoma. *J. Clin. Oncol.* (1997) doi:10.1200/JCO.1997.15.10.3266.

112. McLaughlin, P. *et al.* Rituximab chimeric anti-CD20 monoclonal antibody therapy for relapsed indolent lymphoma: half of patients respond to a four-dose treatment program. *J. Clin. Oncol.* **16**, 2825–2833 (1998).

113. Ghielmini, M. *et al.* ESMO Guidelines consensus conference on malignant lymphoma 2011 part 1: diffuse large B-cell lymphoma (DLBCL), follicular lymphoma (FL) and chronic lymphocytic leukemia (CLL). *Ann. Oncol.* **24**, 561–576 (2013).

114. Brugières, L. & Brice, P. Lymphoma in Adolescents and Young Adults. in 101–114 (2016). doi:10.1159/000447080.

115. Sanjay, V. Non-Hodgkin Lymphoma (NHL). (2021).

116. Chao, M. Treatment challenges in the management of relapsed or refractory non-Hodgkin lymphoma - novel and emerging therapies. *Cancer Manag. Res.* 251–269 (2013) doi:10.2147/CMAR.S34273.

117. Leandro, M. J. B-cell subpopulations in humans and their differential susceptibility to depletion with anti-CD20 monoclonal antibodies. *Arthritis Res. Ther.* **15**, S3 (2013).

118. Casan, J. M. L., Wong, J., Northcott, M. J. & Opat, S. Anti-CD20 monoclonal antibodies: reviewing a revolution. *Hum. Vaccines Immunother.* **14**, 2820–2841 (2018).

119. Pievani, A. *et al.* Enhanced killing of human B-cell lymphoma targets by combined use of cytokine-induced killer cell (CIK) cultures and anti-CD20 antibodies. *Blood* (2011) doi:10.1182/blood-2010-06-290858.

120. Bologna, L. *et al.* Mechanism of Action of Type II, Glycoengineered, Anti-CD20 Monoclonal Antibody GA101 in B-Chronic Lymphocytic Leukemia Whole Blood Assays in Comparison with Rituximab and Alemtuzumab. *J. Immunol.* **186**, 3762–3769 (2011).

121. Mössner, E. *et al.* Increasing the efficacy of CD20 antibody therapy through the engineering of a new type II anti-CD20 antibody with enhanced direct and immune effector cell–mediated B-cell cytotoxicity. *Blood* **115**, 4393–4402 (2010).

122. Goede, V. *et al.* Obinutuzumab plus Chlorambucil in Patients with CLL and Coexisting Conditions. *N. Engl. J. Med.* **370**, 1101–1110 (2014).

123. Sehn, L. H. *et al.* Randomized Phase II Trial Comparing Obinutuzumab (GA101) With Rituximab in Patients With Relapsed CD20 + Indolent B-Cell Non-Hodgkin Lymphoma: Final Analysis of the GAUSS Study. *J. Clin. Oncol.* **33**, 3467–3474 (2015).

124. Sehn, L. H. *et al.* Obinutuzumab plus bendamustine versus bendamustine monotherapy in patients with rituximab-refractory indolent non-Hodgkin lymphoma (GADOLIN): a randomised, controlled, open-label, multicentre, phase 3 trial. *Lancet Oncol.* **17**, 1081–1093 (2016).

125. Marcus, R. *et al.* Obinutuzumab for the First-Line Treatment of Follicular Lymphoma. *N. Engl. J. Med.* **377**, 1331–1344 (2017).

126. Salles, G. *et al.* Phase 1 study results of the type II glycoengineered humanized anti-CD20 monoclonal antibody obinutuzumab (GA101) in B-cell lymphoma patients. *Blood* **119**, 5126–5132 (2012).

127. Sehn, L. H. *et al.* A phase 1 study of obinutuzumab induction followed by 2 years of maintenance in patients with relapsed CD20-positive B-cell malignancies. *Blood* **119**, 5118–5125 (2012).

128. Cartron, G. *et al.* Therapeutic activity of humanized anti-CD20 monoclonal antibody

and polymorphism in IgG Fc receptor FcγRIIIa gene. *Blood* **99**, 754–758 (2002).

129. Radford, J. *et al.* Obinutuzumab (GA101) plus CHOP or FC in relapsed/refractory follicular lymphoma: results of the GAUDI study (BO21000). *Blood* **122**, 1137–1143 (2013).

130. Dyer, M. J. *et al.* Obinutuzumab (GA101) in Combination with CHOP (Cyclophosphamide, Doxorubicin, Vincristine and Prednisone) or Bendamustine for the First-Line Treatment of Follicular Non-Hodgkin Lymphoma: Final Results from the Maintenance Phase of the Phase Ib GAUDI Study. *Blood* **124**, 1743–1743 (2014).

131. Azamjah, N., Soltan-Zadeh, Y. & Zayeri, F. Global Trend of Breast Cancer Mortality Rate: A 25-Year Study. *Asian Pacific J. Cancer Prev.* **20**, 2015–2020 (2019).

132. Prat, A. *et al.* Clinical implications of the intrinsic molecular subtypes of breast cancer. *The Breast* **24**, S26–S35 (2015).

133. Tzahar, E. *et al.* A hierarchical network of interreceptor interactions determines signal transduction by Neu differentiation factor/neuregulin and epidermal growth factor. *Mol. Cell. Biol.* **16**, 5276–87 (1996).

134. Karunagaran, D. *et al.* ErbB-2 is a common auxiliary subunit of NDF and EGF receptors: implications for breast cancer. *EMBO J.* **15**, 254–64 (1996).

135. Ross, J. S. *et al.* The HER-2/ neu Gene and Protein in Breast Cancer 2003: Biomarker and Target of Therapy. *Oncologist* **8**, 307–325 (2003).

136. Stern, D. F., Heffernan, P. A. & Weinberg, R. A. p185, a product of the neu proto-oncogene, is a receptorlike protein associated with tyrosine kinase activity. *Mol. Cell. Biol.* **6**, 1729–1740 (1986).

137. Hayes, D. F. & Thor, A. D. c-erbB-2 in breast cancer: development of a clinically useful marker. *Semin. Oncol.* **29**, 231–45 (2002).

138. Masood, S. & Bui, M. M. Prognostic and predictive value of HER2/neu oncogene in breast cancer. *Microsc. Res. Tech.* **59**, 102–8 (2002).

139. García-Aranda, M. & Redondo, M. Immunotherapy: A Challenge of Breast Cancer Treatment. *Cancers (Basel).* **11**, 1822 (2019).

140. Luque-Cabal, M., García-Teijido, P., Fernández-Pérez, Y., Sánchez-Lorenzo, L. & Palacio-Vázquez, I. Mechanisms behind the Resistance to Trastuzumab in HER2-Amplified Breast Cancer and Strategies to Overcome It. *Clin. Med. Insights Oncol.* **10s1**, CMO.S34537 (2016).

141. Corti, C., Giugliano, F., Nicolò, E., Ascione, L. & Curigliano, G. Antibody–Drug Conjugates for the Treatment of Breast Cancer. *Cancers (Basel).* **13**, 2898 (2021).

142. Figueroa-Magalhães, M. C., Jelovac, D., Connolly, R. M. & Wolff, A. C. Treatment of HER2-positive breast cancer. *The Breast* **23**, 128–136 (2014).

143. Baeuerle, P. A., Kufer, P. & Bargou, R. BiTE: Teaching antibodies to engage T-cells

for cancer therapy. *Curr. Opin. Mol. Ther.* **11**, 22–30 (2009).

144. Einsele, H. *et al.* The BiTE (bispecific T-cell engager) platform: Development and future potential of a targeted immuno-oncology therapy across tumor types. *Cancer* **126**, 3192–3201 (2020).

145. Ma, J. *et al.* Bispecific Antibodies: From Research to Clinical Application. *Front. Immunol.* **12**, 626616 (2021).

146. Peipp, M., Dechant, M. & Valerius, T. Effector mechanisms of therapeutic antibodies against ErbB receptors. *Curr. Opin. Immunol.* **20**, 436–443 (2008).

147. Peipp, M. & Valerius, T. Bispecific antibodies targeting cancer cells. *Biochem. Soc. Trans.* **30**, 507–511 (2002).

148. Booy, E. P. *et al.* Monoclonal and bispecific antibodies as novel therapeutics. *Arch. Immunol. Ther. Exp. (Warsz).* **54**, 85–101 (2006).

149. Topp, M. S. *et al.* Targeted Therapy With the T-Cell–Engaging Antibody Blinatumomab of Chemotherapy-Refractory Minimal Residual Disease in B-Lineage Acute Lymphoblastic Leukemia Patients Results in High Response Rate and Prolonged Leukemia-Free Survival. *J. Clin. Oncol.* **29**, 2493–2498 (2011).

150. Oberg, H.-H. *et al.* Novel bispecific antibodies increase γδ T-cell cytotoxicity against pancreatic cancer cells. *Cancer Res.* **74**, 1349–60 (2014).

151. Christiansen, J. & Rajasekaran, A. K. Biological impediments to monoclonal antibody-based cancer immunotherapy. *Mol. Cancer Ther.* **3**, 1493–1501 (2004).

152. Capone, P. M., Papsidero, L. D. & Chu, T. M. Relationship between antigen density and immunotherapeutic response elicited by monoclonal antibodies against solid tumors. *J. Natl. Cancer Inst.* **72**, 673–7 (1984).

153. Frantz, C., Stewart, K. M. & Weaver, V. M. The extracellular matrix at a glance. *J. Cell Sci.* **123**, 4195–4200 (2010).

154. Lu, P., Weaver, V. M. & Werb, Z. The extracellular matrix: A dynamic niche in cancer progression. *J. Cell Biol.* **196**, 395–406 (2012).

155. Lund, A. W. *et al.* Lymphatic vessels regulate immune microenvironments in human and murine melanoma. *J. Clin. Invest.* **126**, 3389–3402 (2016).

156. Podgrabinska, S. *et al.* Inflamed lymphatic endothelium suppresses dendritic cell maturation and function via Mac-1/ICAM-1-dependent mechanism. *J. Immunol.* **183**, 1767–79 (2009).

157. Lakins, M. A., Ghorani, E., Munir, H., Martins, C. P. & Shields, J. D. Cancer-associated fibroblasts induce antigen-specific deletion of CD8 + T Cells to protect tumour cells. *Nat. Commun.* **9**, 948 (2018).

158. Salemme, V., Centonze, G., Cavallo, F., Defilippi, P. & Conti, L. The Crosstalk Between Tumor Cells and the Immune Microenvironment in Breast Cancer:

Implications for Immunotherapy. *Front. Oncol.* **11**, (2021).

159. Arnould, L. *et al.* Trastuzumab-based treatment of HER2-positive breast cancer: an antibody-dependent cellular cytotoxicity mechanism? *Br. J. Cancer* **94**, 259–267 (2006).

160. Correia, A. L. & Bissell, M. J. The tumor microenvironment is a dominant force in multidrug resistance. *Drug Resist. Updat.* **15**, 39–49 (2012).

161. Zhu, G.-G. *et al.* Immunohistochemical study of type I collagen and type I pN-collagen in benign and malignant ovarian neoplasms. *Cancer* **75**, 1010–1017 (1995).

162. Gould, V. E., Koukoulis, G. K. & Virtanen, I. Extracellular matrix proteins and their receptors in the normal, hyperplastic and neoplastic breast. *Cell Differ. Dev.* **32**, 409–416 (1990).

163. Hasebe, T., Tsuda, H., Tsubono, Y., Imoto, S. & Mukai, K. Fibrotic focus in invasive ductal carcinoma of the breast: a histopathological prognostic parameter for tumor recurrence and tumor death within three years after the initial operation. *Jpn. J. Cancer Res.* **88**, 590–9 (1997).

164. Colpaert, C. G. *et al.* The presence of a fibrotic focus in invasive breast carcinoma correlates with the expression of carbonic anhydrase IX and is a marker of hypoxia and poor prognosis. *Breast Cancer Res. Treat.* **81**, 137–47 (2003).

165. Boyd, N. F. *et al.* Heritability of Mammographic Density, a Risk Factor for Breast Cancer. *N. Engl. J. Med.* **347**, 886–894 (2002).

166. Huijbers, I. J. *et al.* A Role for Fibrillar Collagen Deposition and the Collagen Internalization Receptor Endo180 in Glioma Invasion. *PLoS One* **5**, e9808 (2010).

167. Levental, K. R. *et al.* Matrix Crosslinking Forces Tumor Progression by Enhancing Integrin Signaling. *Cell* **139**, 891–906 (2009).

168. Fraley, S. I. *et al.* A distinctive role for focal adhesion proteins in three-dimensional cell motility. *Nat. Cell Biol.* **12**, 598–604 (2010).

169. Paszek, M. J. *et al.* Tensional homeostasis and the malignant phenotype. *Cancer Cell* **8**, 241–254 (2005).

170. van Kempen, L. C. L. T., Ruiter, D. J., van Muijen, G. N. P. & Coussens, L. M. The tumor microenvironment: a critical determinant of neoplastic evolution. *Eur. J. Cell Biol.* **82**, 539–548 (2003).

171. de Andrade Natal, R., Adur, J., Cesar, C. L. & Vassallo, J. Tumor extracellular matrix: lessons from the second-harmonic generation microscopy. *Surg. Exp. Pathol.* **4**, 7 (2021).

172. Provenzano, P. P. *et al.* Collagen reorganization at the tumor-stromal interface facilitates local invasion. *BMC Med.* **4**, 38 (2006).

173. Riching, K. M. *et al.* 3D Collagen Alignment Limits Protrusions to Enhance Breast

Cancer Cell Persistence. *Biophys. J.* **107**, 2546–2558 (2014).

174. Pieri, L., Sassoli, C., Romagnoli, P. & Domenici, L. Use of periodate-lysine-paraformaldehyde for the fixation of multiple antigens in human skin biopsies. *Eur. J. Histochem.* **46**, 365–75 (2010).

175. Peranzoni, E. *et al.* Ex Vivo Imaging of Resident CD8 T Lymphocytes in Human Lung Tumor Slices Using Confocal Microscopy. *J. Vis. Exp.* (2017) doi:10.3791/55709.

176. Campagnola, P. J. *et al.* Three-Dimensional High-Resolution Second-Harmonic Generation Imaging of Endogenous Structural Proteins in Biological Tissues. *Biophys. J.* **82**, 493–508 (2002).

177. Desa, D. E. *et al.* Second-Harmonic Generation Imaging Reveals Changes in Breast Tumor Collagen Induced by Neoadjuvant Chemotherapy. *Cancers (Basel).* **14**, (2022).

178. Guilbert, T. *et al.* A robust collagen scoring method for human liver fibrosis by second harmonic microscopy. *Opt. Express* **18**, 25794–807 (2010).

179. Palmerini, P. *et al.* A serum-free protocol for the ex vivo expansion of Cytokine-Induced Killer cells using gas-permeable static culture flasks. *Cytotherapy* **22**, 511–518 (2020).

180. Dalla Pietà, A. *et al.* Innovative therapeutic strategy for B-cell malignancies that combines obinutuzumab and cytokine-induced killer cells. *J. Immunother. cancer* **9**, (2021).

181. Bartel, C. A. & Jackson, M. W. HER2-positive breast cancer cells expressing elevated FAM83A are sensitive to FAM83A loss. *PLoS One* **12**, e0176778 (2017).

182. Jernström, S. *et al.* Drug-screening and genomic analyses of HER2-positive breast cancer cell lines reveal predictors for treatment response. *Breast Cancer Targets Ther.* **Volume 9**, 185–198 (2017).

183. Brischwein, K. *et al.* MT110: a novel bispecific single-chain antibody construct with high efficacy in eradicating established tumors. *Mol. Immunol.* **43**, 1129–43 (2006).

184. Cosenza, M., Sacchi, S. & Pozzi, S. Cytokine Release Syndrome Associated with T-Cell-Based Therapies for Hematological Malignancies: Pathophysiology, Clinical Presentation, and Treatment. *Int. J. Mol. Sci.* **22**, 7652 (2021).

185. Hay, K. A. *et al.* Kinetics and biomarkers of severe cytokine release syndrome after CD19 chimeric antigen receptor-modified T-cell therapy. *Blood* **130**, 2295–2306 (2017).

186. Bougherara, H. *et al.* Real-Time Imaging of Resident T Cells in Human Lung and Ovarian Carcinomas Reveals How Different Tumor Microenvironments Control T Lymphocyte Migration. *Front. Immunol.* **6**, (2015).

187. Guerin, M. V. *et al.* TGFβ blocks IFNα/β release and tumor rejection in spontaneous

mammary tumors. *Nat. Commun.* **10**, 4131 (2019).

188. Weiss, J. M. *et al.* The STING agonist DMXAA triggers a cooperation between T lymphocytes and myeloid cells that leads to tumor regression. *Oncoimmunology* **6**, (2017).

189. Vermare, A., Guérin, M. V, Peranzoni, E. & Bercovici, N. Dynamic CD8+ T Cell Cooperation with Macrophages and Monocytes for Successful Cancer Immunotherapy. *Cancers (Basel).* **14**, (2022).

190. Seewaldt, V. ECM stiffness paves the way for tumor cells. *Nat. Med.* **20**, 332–333 (2014).

191. Nicolas-Boluda, A. *et al.* Tumor stiffening reversion through collagen crosslinking inhibition improves T cell migration and anti-PD-1 treatment. *Elife* **10**, (2021).

192. Peranzoni, E. *et al.* Ex Vivo Imaging of Resident CD8 T Lymphocytes in Human Lung Tumor Slices Using Confocal Microscopy. *J. Vis. Exp.* (2017) doi:10.3791/55709.

193. Kauppila, S., Stenbäck, F., Risteli, J., Jukkola, A. & Risteli, L. Aberrant type I and type III collagen gene expression in human breast cancerin vivo. *J. Pathol.* **186**, 262–268 (1998).

194. Schmeel, L. C., Schmeel, F. C., Coch, C. & Schmidt-Wolf, I. G. H. Cytokine-induced killer (CIK) cells in cancer immunotherapy: report of the international registry on CIK cells (IRCC). *J. Cancer Res. Clin. Oncol.* **141**, 839–849 (2015).

195. Giraudo, L. *et al.* Cytokine-induced killer cells as immunotherapy for solid tumors : current evidences and perspectives. *Immunotherapy* (2015).

196. Grupp, S. A. *et al.* Chimeric antigen receptor-modified T cells for acute lymphoid leukemia. *N. Engl. J. Med.* **368**, 1509–1518 (2013).

197. Neelapu, S. S. *et al.* Axicabtagene Ciloleucel CAR T-Cell Therapy in Refractory Large B-Cell Lymphoma. *N. Engl. J. Med.* **377**, 2531–2544 (2017).

198. Cai, Q., Zhang, M. & Li, Z. Potential strategies against resistance to CAR T-cell therapy in haematological malignancies. *Ther. Adv. Med. Oncol.* **12**, 175883592096296 (2020).

199. Smith, S. D. *et al.* Eligibility for CAR T-cell therapy: An analysis of selection criteria and survival outcomes in chemorefractory DLBCL. *Am. J. Hematol.* **94**, (2019).

200. Das, R. K., Vernau, L., Grupp, S. A. & Barrett, D. M. Naïve T-cell Deficits at Diagnosis and after Chemotherapy Impair Cell Therapy Potential in Pediatric Cancers. *Cancer Discov.* **9**, 492–499 (2019).

201. Klebanoff, C. A., Gattinoni, L. & Restifo, N. P. Sorting through subsets: which T-cell populations mediate highly effective adoptive immunotherapy? *J. Immunother.* **35**, 651–60 (2012).

202. Introna, M. *et al.* Phase II Study of Sequential Infusion of Donor Lymphocyte Infusion and Cytokine-Induced Killer Cells for Patients Relapsed after Allogeneic Hematopoietic Stem Cell Transplantation. *Biol. Blood Marrow Transplant.* **23**, 2070–2078 (2017).

203. Sarvaria, A., Madrigal, J. A. & Saudemont, A. B cell regulation in cancer and anti-tumor immunity. *Cell. Mol. Immunol.* **14**, 662–674 (2017).

204. Zhang, Y., Gallastegui, N. & Rosenblatt, J. D. Regulatory B cells in anti-tumor immunity. *Int. Immunol.* **27**, 521–530 (2015).

205. Horikawa, M., Minard-Colin, V., Matsushita, T. & Tedder, T. F. Regulatory B cell production of IL-10 inhibits lymphoma depletion during CD20 immunotherapy in mice. *J. Clin. Invest.* **121**, 4268–4280 (2011).

206. Mahnke, Y. D., Brodie, T. M., Sallusto, F., Roederer, M. & Lugli, E. The who's who of T-cell differentiation: human memory T-cell subsets. *Eur. J. Immunol.* **43**, 2797–809 (2013).

207. Sendur, M. A. N., Aksoy, S. & Altundag, K. Cardiotoxicity of novel HER2-targeted therapies. *Curr. Med. Res. Opin.* **29**, 1015–1024 (2013).

208. Darwich, A. *et al.* Paralysis of the cytotoxic granule machinery is a new cancer immune evasion mechanism mediated by chitinase 3-like-1. *J. Immunother. cancer* **9**, (2021).

209. Ansari, K. I., Bhan, A., Liu, X., Chen, M. Y. & Jandial, R. Astrocytic IGFBP2 and CHI3L1 in cerebrospinal fluid drive cortical metastasis of HER2+breast cancer. *Clin. Exp. Metastasis* **37**, 401–412 (2020).

210. Zitvogel, L., Pitt, J. M., Daillère, R., Smyth, M. J. & Kroemer, G. Mouse models in oncoimmunology. *Nat. Rev. Cancer* **16**, 759–773 (2016).

211. Di Modugno, F. *et al.* 3D models in the new era of immune oncology: focus on T cells, CAF and ECM. *J. Exp. Clin. Cancer Res.* **38**, 117 (2019).

212. Bhakta, N. R., Oh, D. Y. & Lewis, R. S. Calcium oscillations regulate thymocyte motility during positive selection in the three-dimensional thymic environment. *Nat. Immunol.* **6**, 143–151 (2005).

213. Elliott, A. D. Confocal Microscopy: Principles and Modern Practices. *Curr. Protoc. Cytom.* **92**, e68 (2020).

214. Faklaris, O. *et al.* Quality assessment in light microscopy for routine use through simple tools and robust metrics. *J. Cell Biol.* **221**, (2022).

215. Oreopoulos, J., Berman, R. & Browne, M. Spinning-disk confocal microscopy: present technology and future trends. *Methods Cell Biol.* **123**, 153–75 (2014).